



**Investigating Time and Spectral Dependence in
Neutron Radiation Environments for
Semiconductor Damage Studies**

DISSERTATION

Matthew R. Halstead, Civilian, USA

AFIT-ENP-DS-14-S-04

**DEPARTMENT OF THE AIR FORCE
AIR UNIVERSITY**

AIR FORCE INSTITUTE OF TECHNOLOGY

Wright-Patterson Air Force Base, Ohio

DISTRIBUTION STATEMENT A

Approved for public release; distribution unlimited

The views expressed in this document are those of the author and do not reflect the official policy or position of the United States Air Force, the United States Department of Defense or the United States Government. This material is declared a work of the U.S. Government and is not subject to copyright protection in the United States.

AFIT-ENP-DS-14-S-04

INVESTIGATING TIME AND SPECTRAL DEPENDENCE IN NEUTRON
RADIATION ENVIRONMENTS FOR SEMICONDUCTOR DAMAGE STUDIES

DISSERTATION

Presented to the Faculty
Graduate School of Engineering and Management
Air Force Institute of Technology
Air University
Air Education and Training Command
in Partial Fulfillment of the Requirements for the
Degree of Doctor of Philosophy

Matthew R. Halstead, BS, MS
Civilian, USA

September 2014

DISTRIBUTION STATEMENT A

Approved for public release; distribution unlimited

INVESTIGATING TIME AND SPECTRAL DEPENDENCE IN NEUTRON
RADIATION ENVIRONMENTS FOR SEMICONDUCTOR DAMAGE STUDIES

Matthew R. Halstead, BS, MS
Civilian, USA

Approved:

//signed//

17 July 2014

Dr. James C. Petrosky
Dissertation Advisor
Chair

Date

//signed//

July 17, 2014

Dr. Edward White
Committee Member
Member

Date

//signed//

July 17, 2014

Dr. Paul E. Sokol
Committee Member
Member

Date

Accepted:

//signed//

July 17, 2014

Adedeji B. Badiru, Ph.D.
Dean, Graduate School of Engineering
and Management

Date

Abstract

As legacy neutron irradiation facilities are shut down due to security and financial constrictions, a growing need arises for alternatives that can provide the same or similar radiation environments using methods and/or fuels that do not pose the same risks. For this reason, facilities that provide much lower neutron fluxes and different spectral shapes are being leveraged over longer irradiation intervals to meet this need. However, the question arises as to whether the use of these types of facilities provide a valid comparison to the legacy systems' results.

To this end, a model using a system of coupled, non-linear ordinary differential equations has been developed to track defect species in silicon for short pulse neutron irradiations. This model has been used to predict current gain degradation in silicon BJTs for various neutron fluences. These predictions have been compared against experimental data collected at two neutron irradiation facilities with different time and spectral profiles. The damage constant during irradiation has been determined, and it is different for both facilities. However, the time profile is found to have no effect in the region tested in this work. Now that this analysis has been done, these types of facilities can be used for radiation vulnerability analysis studies for use in short pulse neutron damage studies.

To my wife

Acknowledgements

So many people and organizations were essential to this research's successful completion. First, this research was financially supported by the NSWC (Crane) through the DoD's SMART scholarship. Without their support, none of this would have been possible. Also, Steve Clark of NSWC (Crane) has been my biggest supporter from the very beginning, providing encouragement and doing all he could to help me through the hardest of times.

It was my privilege to work with scientists and researchers at the Center for the Exploration of Energy and Matter at Indiana University in Bloomington, IN. In particular, my thanks goes to Tom Rinckel, Sangjin Lee, and Andy Edwards.

Next, I want to acknowledge and thank my research committee for bringing all their expertise to bear upon my research topic. Dr. White brought fresh insight from a mathematics perspective. Dr. Sokol's experience as an experimentalist and a solid state physicist meant he always knew the right question to ask, even when I knew I did not have the answer.

It is difficult to express the deep thanks I wish to express to my research advisor, Dr. Petrosky. From the first day I walked through his door and told him I'd be attending AFIT, he took it upon himself to act as mentor, teacher, dad, mom, Drill Sergeant, and life coach. Without a doubt, I have learned more from our discussions over the last 5 years than I ever thought possible. I hope I can one day attain the level of deep understanding of physics and life that Dr. Petrosky so obviously has and so generously shares.

Matthew R. Halstead

Table of Contents

	Page
Abstract	iv
Acknowledgements	vi
List of Figures	ix
List of Tables	xviii
List of Abbreviations	xx
I. Introduction	1
1.1 Overview	1
Legacy Test Systems	2
Neutron Source Alternatives	3
1.2 Testing Si Bipolar Transistors	6
1.3 Motivation	7
1.4 Problem statement	10
References	11
II. Theory	13
2.1 Basic Semiconductor Physics	13
Material Classification	13
Doping of Semiconductor Material	15
Semiconductor Junctions	16
Semiconductor Device Types & Applications	17
2.2 Semiconductor Defects in Silicon	22
Defect Clusters	25
Short Term Annealing	26
2.3 Radiation Environments and Hardness Testing	29
Description of hardness testing	30
Radiation Testing Facilities	31
Spectral Collapsing	36
References	38
III. First-Principles Modeling of BJT Performance	43
3.1 Historical Modeling Efforts	43
3.2 Model Development Progression	46
Step One – General Defect Mode	47
Step Two – Model Including Multiple Defect Species	48
Step Three – Incorporation of Precursors	50

	Page
Step Four – Incorporating Concentrations, C_{def}	52
Step Five – Development of Reaction Rate Parameters	57
Step Six – Gain, β , Calculation	59
Step Seven – Adding Additional Species	65
Step Eight – Temporal Profile Capability	71
3.3 Initial Model Results	72
References	78
 IV. Experimental Verification	81
4.1 IU NREF Experiments	82
Facility Description	82
NREF Experiment 1: Exploration Experiments	85
NREF Experiment 2: Expanded Dataset	98
4.2 OSURR Experimental Series	116
Facility Description	118
OSURR Test Equipment	120
OSURR Test Procedure	122
Neutron Dosimetry	123
BJT Gain Degradation Experiment	127
References	136
 V. Comparison of Model to Experiment	139
5.1 Sensitivity Analysis	139
5.2 Parameter Search	142
5.3 Model/Data Comparison	146
References	152
 VI. Summary, Conclusions, and Way Forward	153
6.1 Summary of Research	153
6.2 Conclusions	159
6.3 Ideas for Future Research	160

List of Figures

Figure	Page
1. The normalized neutron spectrum of three different types of neutron generators shows that each provides a different spectral shape and may be relevant for different applications [11].	5
2. A schematic of the energy bands for a conductor (left) with a partially filled conduction band (top) and with overlapping valence and conduction bands (bottom), a semiconductor (middle), and an insulator (right). (Figure derived from [3].)	14
3. Measured ionization energies for select acceptors and donors in Si (in eV). Below the Fermi level, impurities are acceptors (unless otherwise noted); above the Fermi level, impurities are donors. (Figure derived from [3].)	16
4. A schematic view of an idealized n^+pn bipolar junction transistor. The silicon dioxide is used to passivate the surface boundary. (Figure derived from [3].)	18
5. The Fermi level, E_f , is continuous across the entire bandgap schematic of an idealized n^+pn BJT in thermal and electronic equilibrium.	19
6. The BJT bandgap shifts as bias is applied. In this case, positive voltage is applied at the emitter, and negative voltage is applied to the collector while the base is kept at ground.	20
7. Idealized schematic of electron and hole currents in an n^+pn BJT.	21
8. Schematic of the creation of a Frenkel pair (in this case using low-energy neutron bombardment of the crystal lattice). [10]	23
9. Recreation of a typical history track of a 50 keV recoil atom in silicon produced using a Monte Carlo simulation. [24]	26

Figure	Page
10. Schematic representation of defect and subcascade formation as a function of PKA energy. The y-axis of the plot is logarithmic and representative of the number of interactions [27].	27
11. A schematic of the IUCF cyclotron is a proton accelerator that can provide 20 ns pulses of 200 MeV protons at about 2×10^{10} rad(Si)/s [41].	31
12. Reactor Core at the OSURR shows multiple irradiation facilities (CIF, AIF, PIF) as well as beam ports for external set-up and irradiation.	33
13. Neutron differential flux spectrum at the OSURR 7 inch tube at full power where the 1-MeV equivalent (Si) flux at this power level is 1.92×10^{11} n/cm ² /s and the hardness is 0.13.	34
14. A schematic of the IU NREF beamline at the LENS.	35
15. Using a single defect species results in the growth of the defect population that approaches an asymptote with a time constant characteristic of the relaxation of defect species during irradiation.	48
16. For this arbitrary selection of parameters, the vacancy population rises quickly, but reaches a secular equilibrium at a lower level than the di-vacancies during irradiation.	50
17. The displacement damage kerma for a silicon semiconductor as tabulated in the ASTM Standard E722 [19].	56
18. The dopant concentrations (B^+ and P^-) in the base-emitter region of a 2n2222A silicon BJT were determined from spreading resistance measurements and SIMS data [13].	60
19. Diffusivity (left) and mobility (right) as a function of impurity concentration in the semiconductor bulk is flat till 10^{15} cm ⁻³ ; it can be affected by radiation induced defects adding to the impurity concentration.	62

Figure	Page
20. The neutron flux for the hypothetical situation in Figure 21 corresponds to a 1-MeV equivalent (Si) flux of 5×10^{10} n/cm ² /s using the ASTM standard method of calculation.	63
21. The first simulation using the model with six defect species and a time-averaged 1-MeV equivalent neutron flux of 5×10^{10} n/cm ⁻² /s and an initial impurity concentration of 5×10^{15} at/cm ³	64
22. Results of the calculation of gain change as a function of fluence for the hypothetical situation uncover an issue with the model as it shows that the change in gain would begin to recover during irradiation, which is not observed in literature.	65
23. The calculation of residuals between vacancies “created” and vacancies “accounted for” is below the tolerance set for noise in the calculation, meaning that the value is effectively zero at all x-axis values.	69
24. The test of computational time versus irradiation and annealing time showed a nearly linear relationship from 0 s to 1200 s.	74
25. The plot of species concentrations after simulating a 10 s irradiation period followed by a 10 s annealing period displays a noticeable vacancy defect concentration increase and subsequent annealing during each pulse cycle.	75
26. The change in gain as a function of fluence during irradiation calculated using the model developed in this research. It simulates a 10 s irradiation period and displays a generally linear response with a sawtooth-like pattern corresponding to irradiation and annealing during a pulse cycle.	76
27. (Top) The simulated change in gain during annealing. (Bottom) The simulated annealing factor after irradiation. Annealing in the model occurs quite quickly and approaches the final value within less than 1 s.	77

Figure	Page
28. The IU LINAC Facility schematic shows the proton source and LINAC at bottom left; the beam is split to targets in lower right and upper middle [6].....	83
29. The IU NREF beam is pulsed, and the duty cycle is typically around 0.8% with the current configuration. Ideally, the beam pulse is a square wave; however, each pulse has a rise and fall transient.....	84
30. Using Monte Carlo particle simulation software and an input deck provided by IU NREF personnel [11], the neutron spectrum was calculated on a <i>per proton</i> basis and at different distances from the beryllium target; this can then be scaled based on the proton source specifications for a particular run.....	85
31. When operating the proton source at a current of 20 mA, the resultant neutron spectrum is scaled to a 1-MeV equivalent (Si) neutron flux of $> 6 \times 10^{10}$ n/cm ² /s.	86
32. A close-up of the DuT fixture (left), switchbox (middle), and SMUs (right). In the text fixture and switchbox, the aluminum box acted as an EMI shield.	86
33. The test set-up inside the TMR included a block of acrylic to position the DuT fixture at the centerline of the beam. The acrylic jack sat atop this block. The aluminum test rig is positioned to the left of the jack and is facility the beryllium target (which is out of sight below and to the left of the set-up).	87
34. A schematic of the shunt and test BJTs. The BJT being analyzed is in Common Ground configuration.....	88
35. BJT gain as a function of time for the MSI test. The intervals of irradiation and intervals of annealing were fit to the Messenger-Spratt equation and a power function, respectively.	90
36. Gain as a function of time for continuous irradiations of (a) 20 min, (b) 30 min, (c) 60 min, and (d) 90 min. Note that in (a) there is a significant annealing time (approximately 60 min), while in the other three cases (b-d) there is only a 5 min annealing measured following irradiation.	91

Figure	Page
37. Examples of the curve fitting for both degradation (top) and annealing (bottom). Note that in the top chart, gain was normalized to the precharacterization gain, while on the bottom it has not been normalized.	93
38. The A and C coefficients are plotted as a function of time. The connecting dotted lines in the figures are just for presentation and analysis.	94
39. Comparison of the annealing of BJT gain for multiple sequential interval (top) and single long interval (bottom) tests. The y-axis is the change in gain relative to the start of annealing interval.	95
40. (Top) Gain as a function of temperature during a post-irradiation thermal anneal. Gain was measured <i>in-situ</i> while being baked and normalized to the gain at 150°C. (Bottom) Gain as a function of temperature as the devices were allowed to come back to room temperature after the thermal anneal. Gain in both plots has been normalized to the maximum value (at 150°C).	96
41. A comparison of gain degradation as a function of fluence for multiple systems. "Legacy data" includes data from SPR-III, WSMR FBR, ACRR, and LANSCE. The dotted line represents the $\Delta(1/\beta)$ using the accepted value of the damage constant, K	97
42. Timeline representing irradiation, waiting, and counting times for neutron activation analysis.	102
43. Beta organic scintillation counter at IU (left arrow) for measurement of beta decay products from phosphorus daughter; S pellet was placed in an aluminum holding fixture (right arrow) 14 cm from the detector.	104
44. Schematic showing variables involved in calculating solid angle for a source of beta particles with radius, s , a distance, d , away from a detector with radius, a . The geometric factor, ξ , is dependent on the solid angle.	106
45. Cross sections for neutron capture by (left) ^{32}S , (middle) ^{54}Fe , and (right) ^{56}Fe . Note that the units of the y-axis are in mb.	108

Figure	Page
46. A comparison of the measured and expected activity at infinite irradiation time for the IU NREF neutron spectrum provides good agreement for the Fe foils for 4.96×10^{10} n/cm ² /s while the S pellet does not agree.	110
47. The $\Delta(1/\beta)$ with fluence for the 4 dosimetric shots with error corresponding to beam current uncertainty in the x-direction and equipment error in the y-direction. The average slope was $3.06 (\pm 0.55) \times 10^{-15}$ cm ² /n.	111
48. The $\Delta(1/\beta)$ with fluence for three of the five variable fluence shots with error corresponding to beam current uncertainty in the x-direction and equipment error in the y-direction. Shots 5 and 8 were removed because the beam current fluctuated during the shot.	112
49. (a) IU NREF beam current as a function of time for the experiment. (b) The proton beam current was not constant throughout the experimental series, and an example of proof of this is that the beam current ratio of 5F, which should be 6.0, is 12% higher.	114
50. Shots 5F (top) and 8F (bottom) of the $\Delta(1/\beta)$ versus fluence. In these two shots, the proton beam current jumped between low and high values during the irradiation. The blue dotted vertical lines correspond to the time/fluence at which the beam current changed during the irradiation.	115
51. The $\Delta(1/\beta)$ versus fluence for the experimental data collected from the second experimental series at IU NREF as compared to data from various single-pulse, short-duration irradiation facilities such as SPR-III and WSMR FBR.	117
52. Simulation of three different irradiation conditions at the IU NREF and OSURR.	118
53. Image looking down in the OSURR reactor pool at the core during operation. This shows the multiple tubes and beam-ports available for use. The 7 inch tube used for irradiations was positioned at the red X. [Photo obtained from OSURR Staff.]	119

Figure	Page
54. Neutron differential flux spectrum at the OSURR 7 inch tube at full power where the 1-MeV equivalent (Si) flux at this power level is 1.92×10^{11} n/cm ² /s and the hardness is 0.13.	120
55. SMU set up next to the OSURR reactor pool.	121
56. The test rig built for the OSURR experiments was simple and made from materials that would minimally activate so that the experiment could be accomplished as many times as possible while requiring the minimum downtime for radioactive decay between shots.	122
57. Cross sections for neutron capture by ⁵⁸ Fe; note that the units of the y-axis are in b this time.	125
58. Comparison of measured dosimetric data (black dots) for packet 1 (left) and packet 2 (right) with curves of saturation activity as a function of 1-MeV equivalent flux with the expected value of 1.92×10^9 n/cm ² /s for 1% power in the 7 inch tube at OSURR shows that the pellet/foil set agrees well with the Monte Carlo simulation results and OSURR reactor estimates, within experimental error.....	126
59. Comparison of measured dosimetric data (black dots) for packet 1 (left) and packet 2 (right) with curves of saturation activity as a function of 1-MeV equivalent flux with the expected value of 4.96×10^{10} n/cm ² /s for 23.4% power in the 7 inch tube at OSURR shows that the pellet/foil set agrees well with the Monte Carlo simulation results and OSURR reactor estimates, within experimental error.....	126
60. Raw data from irradiation of 2 BJTs at the OSURR at 1% power for 20 minutes.	130
61. The $\Delta(1/\beta)$ with fluence for the 20 minute irradiation; gain change has been corrected for gamma dose using the ASTM standard value of gamma displacement damage factor.	131
62. The collector current as a function of collector voltage for the 26% power shot.	132

Figure	Page
63. The Messenger-Spratt response during irradiation by $4.96 \times 10^{10} n/cm^2/s$ 1-MeV equivalent (Si) neutrons.....	133
64. The annealing factor of the BJTs irradiated at the OSURR as a function of time after irradiation is completed.....	134
65. The $\Delta(1/\beta)$ as a function of the point in time where the measurement was taken; note that the x -axis is an arbitrary scale.....	135
66. The devices respond differently for different neutron spectra; however, it is yet to be proven whether the ASTM elevated temperature annealing interval will have a significant enough impact to bring all devices back to the literature value for the damage constant.	136
67. This example of a Latin Square shows the three values – A , B , and C – positioned such that each value is used exactly once in every row and column.....	141
68. The time-averaged differential neutron flux at the IU NREF that was used for sensitivity analysis.	142
69. The vacancy concentration over a $400 \mu s$ interval and for a range of vacancy diffusivity values shows little change across the entire range.	143
70. Regression coefficient, R^2 , as calculated for E_{fp} and D_v for the (top two) first, (middle two) second, and (bottom two) final iterations.	147
71. The regression coefficient from Figure 70 is binned in histogram form for the (top two) first try, (middle two) second try, and (bottom two) final try.....	148
72. Three dimensional histogram of $R^2 > 0.9$ showing where both D_v and E_{fp} meet the R^2 cut.	149
73. The change in gain as a function of time for the model as compared with experiment for IU NREF Shot 1T (beam frequency of 20 Hz, pulse width of $400 \mu s$, and 20 mA beam current). There is a small deficit when compared with the data until about 10 min, at which time it follows very well within experimental error.	150

Figure	Page
74. The annealing factor as a function of time shows good agreement for the comparison of the model against experimental data.	151
75. The $\Delta(1/\beta)$ versus fluence for the experimental data collected from the second experimental series at IU NREF as compared to data from various single-pulse, short-duration irradiation facilities such as SPR-III and WSMR FBR.	155
76. Simulation of three different irradiation conditions at the IU NREF and OSURR.	156
77. When comparing all datasets together, the devices respond differently for different neutron spectra; however, it is yet to be confirmed whether the ASTM elevated temperature annealing interval will have a significant enough impact to bring all devices back to the literature value for the damage constant.	157
78. The differential neutron energy spectrum at IU NREF with an example of the way the spectrum may be broken up into the region that creates Frenkel-pairs (left), the region that creates clusters (right), and the region that has some probability of creating either (middle).	161

List of Tables

Table	Page
1. Modes of BJT operation.	20
2. Select defect species and their electronic parameters. Here e^- denotes the conduction electron and h^+ denotes the hole, V is the vacancy, the subscript I denotes an interstitial atom, and charge states are indicated by superscripts. (Derived from [14])	24
3. Description of nine interactions used for six defect species model.	54
4. Model parameters selected for test run of final model design. The lattice constant a_o for silicon at room temperature is 5.4307×10^{-8} cm.	73
5. BJT operating parameters for two measurement methods.	82
6. Beam parameters on the day of experiment.	88
7. Activation analysis results from sulfur foils.	89
8. Fitting coefficients from gain degradation intervals with extracted damage constant, K	92
9. Fitting coefficients from annealing intervals.	92
10. Iron foil mass measurement.	101
11. Sulfur pellet mass measurement.	101
12. Gamma peak information for the iron foils.	102
13. Calculation of measured 1-MeV Equivalent (Si) neutron flux using iron foils.	103
14. Sulfur pellet background measurement for 5 minute counting intervals; note that Cps = counts per second.	104
15. Calculation of measured 1-MeV Equivalent (Si) neutron flux using sulfur pellets.	107

Table	Page
16. Fitting coefficients from gain degradation intervals with extracted flux, ϕ	113
17. The calculated damage constant and linear regression parameter for neutron irradiation at the IU NREF experimental set 2.	116
18. Mass measurement for the OSU dosimeters.	124
19. Iron foil dosimetry analysis for the OSU dosimeters.	127
20. Sulfur pellet dosimetry analysis for the OSU dosimeters.	128
21. Gold foil dosimetry analysis for the OSU dosimeters.	129
22. Parameters (P), Expectation values ($\langle P \rangle$), and Ranges (R) for 17 parameters varied in sensitivity study. Units of D are cm^2/s , units of E are eV, units of ν are s^{-1} and units of Radius are Å.	140
23. First guess for upper and lower bounds for parameter search using LHS methodology.	144
24. Change to upper and lower bounds for the parameter search after first cut using LHS methodology; colors are only to guide the eye to the parameter bounds that became smaller (red), larger (green), or stayed the same (yellow).	145
25. Change to upper and lower bounds for the parameter search after first cut using LHS methodology; colors are only to guide the eye to the parameter bounds that became smaller (red), larger (green), or stayed the same (yellow).	145

List of Abbreviations

Abbreviation	Page
SPR-III	1
APG	1
WSMR	1
SNM	1
ACRR	1
kerma	2
BJT	2
ASTM	2
ACRR	3
DuT	4
IBL	4
SNL	4
IU	5
CEEM	5
NREF	5
LiN	7
DoD	9
DoE	9
LHC	17
TEM	25
PKA	25
SAA	29

Abbreviation		Page
OSURR	Ohio State Research Reactor	32
NREF	Neutron Radiation Effects Facility	32
SAND-II	Spectrum Analysis by Neutron Detectors	33
TMR	Target-Moderator-Reflector	36
ASTM	American Society for Testing and Materials	36
NIEL	Non-Ionizing Energy Loss	43
ODE	Ordinary Differential Equation	52
SIMS	Secondary Ion Mass Spectroscopy	59
IU	Indiana University	71
NREF	Neutron Radiation Effects Facility	71
OSURR	Ohio State University Research Reactor	81
LINAC	Linear Accelerators	83
LENS	Low-Energy Neutron Source	84
NREF	Neutron Radiation Effects Facility	84
TLD	thermoluminescent dosimeters	98
GPIB	General Purpose Interface Bus	98
CIF	Central Irradiation Facility	119
AIF	Auxiliary Irradiation Facility	119
PIF	Peripheral Irradiation Facility	119
GPIB	General Purpose Interface Bus	121
PCB	printed circuit board	121
LHS	Latin Hypercube Sampling	140
FP	Frenkel Pairs	141

INVESTIGATING TIME AND SPECTRAL DEPENDENCE IN NEUTRON RADIATION ENVIRONMENTS FOR SEMICONDUCTOR DAMAGE STUDIES

I. Introduction

1.1 Overview

In the radiation effects on electronics community, the overarching goal of every theoretical analysis, simulation, and experiment is to understand the response of electronic devices and components when subjected to a type and level of radiation. Neutron radiation sources such as fast burst reactors at the Sandia Pulsed Reactor (SPR-III) [1], the Aberdeen Proving Ground (APG) [2], and White Sands Missile Range (WSMR) [3] have been the gold standard for pulsed neutron radiation damage studies. The harsh, but well-quantified, neutron environments at these facilities were used to gain government and industry approval for components used in various systems, such as missiles and satellites. However, some of these facilities have been shut down due to a growing interest in the security of Special Nuclear Material (SNM).

While this happens, researchers search for alternatives that can provide the same or similar radiation environments using methods and/or fuels that do not pose a safety or security risk. Examples of these alternatives include thermal neutron reactors such as the Annular Core Research Reactor (ACRR), neutron surrogate facilities, and accelerator-based neutron sources. Each of these systems has benefits and disadvantages, but there is one trait that they all share. This trait is a lower time-averaged neutron flux requiring longer irradiation times to reach the total fluence required by scientists making comparisons to legacy data collected from fast burst reactors.

Conventional wisdom has held that a spectrum of neutrons can be collapsed into an equivalent number of mono-energetic neutrons. This is done using the concept of damage Kinetic Energy Released per unit MAss (kerma), or the amount of kinetic energy deposited in matter [4], which can then be used to calculate the expected damage in Si devices for a given fluence. In the past, this has been verified for fluences up to and exceeding 10^{14} n/cm² at facilities such as the SPR-III. However, as these fast burst reactors are decommissioned or no longer widely used, the question arises as to whether the use of alternative facilities with longer irradiation times is a valid comparison to the legacy fast burst systems.

It is the overarching goal of this research to investigate the effect of temporal and spectral variance on Bipolar Junction Transistor (BJT) performance for facilities that require a significant amount of irradiation time to reach desired neutron fluences, both constant and continuously-pulsed sources. In this work, only Si n^+pn -type BJTs are considered, since these devices have a significant data history and are well-understood.

Legacy Test Systems.

While short pulse neutron sources have been used for decades and numerous legacy data sets exist in databases around the world, a growing interest in the control and security of SNM has resulted in shutting down a number of these crucial facilities. The SPR-III was decommissioned in 2007 amid a flurry of last-minute experiments [5, 6]. The U.S. Army's fast burst reactor at APG was long-ago decommissioned due to budget and security concerns. The United States' only remaining fast burst reactor is situated at the WSMR in Arizona. It continues to operate, however it also faces budgetary and security concerns. It is for this reason that the community continues to look for alternatives to facilities fueled by SNM.

The American Society for Testing and Materials (ASTM) provides a standard

method to test BJT response to neutrons [7]. In it, the prescribed requirements include very few hard-and-fast stipulations. However, it suggests that the source provide total fluence of particles in very short bursts, often in $100 \mu\text{s}$ or less. With fast burst reactors, it was an inherent physical safeguard that the reaction finished in this time frame or less, which was one reason why the standard was written this way. However, with alternative methods currently proposed, it can be difficult to reach relevant neutron fluence levels in such a short time interval.

Neutron Source Alternatives.

Alternative neutron sources for radiation testing are many and varied. Fission reactors are sources that are typically driven by traditional nuclear reactors fueled with low- to medium-enrichment uranium or mixed-oxide fuel. Examples of this source include the Annular Core Research Reactor (ACRR) [8] as well as university research reactors. Often, they can be operated in both pulsed or steady-state mode. The pulse is caused by a large reactivity insertion instigated by quickly withdrawing a reactor control rod from the core, typically using pneumatic or hydraulic methods. The excess reactivity causes the reactor to go prompt supercritical for a short time before the control rod falls back into the reactor, stifling the reaction.

The advantage of this alternative is that the fuel, while still nuclear material, is of much lower enrichment than for bare metal reactors such as the SPR-III. Additionally, while the pulse width of the critical transient is short, neutron fluences are very high. Unfortunately, since the coolant and moderator is usually light water, the neutron spectrum is heavily shifted to the thermal region. Because of the shift to the thermal region, facilities such as the ACRR are typically used for components that will be primarily used in terrestrial applications, since most damaging neutron irradiation in the oxygen-rich environment near the earth's surface has been greatly thermalized

and the pulse subsequently stretched out in time before reaching the component in question. However, for space-based systems, this is not the case, as much of the neutron radiation (either cosmic or nuclear weapon induced) remains hard and the radiation pulse short. Also, the gamma flux from fission and fission products in thermal reactor systems is relatively high, which adds additional complexity to the analysis of experimental results.

Charged particle accelerators bombard a Device under Test (DuT) with ions and equate the resultant damage to a fluence of neutrons via a transfer function [9]. An example of this system is the Ion Beam Lab (IBL) at Sandia National Laboratory (SNL). Since the ions are charged, packets of them can be accelerated through an electromagnetic field and directed to a DuT. An advantage to this method is the ability to control, manipulate, and focus the incident particles to the target, which can lead to high fluence and short pulse widths. Also, since the charged particles deposit most of their energy at the end of their track, the device being tested can be probed for sensitivity in different areas. However, a disadvantage is that, because the experimenter is not using neutrons, an approximation must be made for damage equivalence. Additionally, since charged particles deposit almost all of their energy at the end of their track in a Bragg peak, the damage that is caused is highly-localized, which is contrary to the homogeneity of damage caused by neutrons. This may be helpful, if the experimenter wishes to probe a very specific region of a device; however, it does not simulate the damage done by neutrons exactly and must be taken into account.

Compact accelerator-driven neutron sources encompass a wide range of irradiation facilities. *Neutron generators* use very small linear accelerators to fuse deuterium, tritium, or a combination of the two [10]. Each combination provides a different total flux and spectrum of neutron energies. An idealized plot of these spectra are

plotted in Figure 1. Typically, these sources run at very low flux and are used for applications more pertinent to medicine or more delicate experiments. More recently, higher flux neutron generators are being developed [10], but these technologies are still in their infancy and not fully realized.

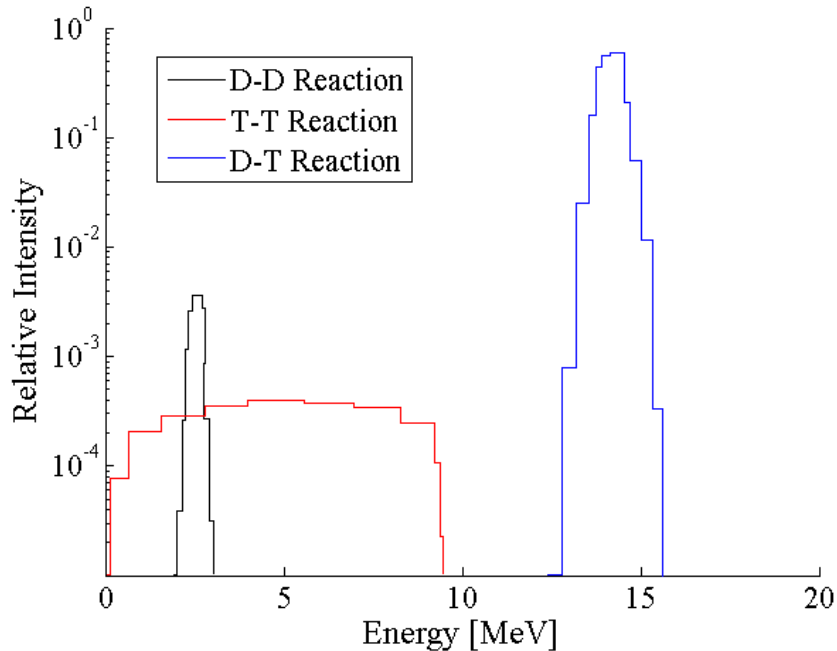


Figure 1. The normalized neutron spectrum of three different types of neutron generators shows that each provides a different spectral shape and may be relevant for different applications [11].

Another example of an accelerator-driven source is the one found at the Indiana University (IU) Center for the Exploration of Energy and Matter (CEEM) Neutron Radiation Effects Facility (NREF). Here, neutrons are created via the inelastic collision of protons in beryllium. The protons are accelerated into a beryllium target using a linear accelerator. The resulting neutrons depend strongly on the incident proton energy and can be very energetic. However, because the amount of energy deposited in the beryllium target is so great, the linear accelerator typically has a short duty time. For example, at the NREF target at CEEM, the standard operating parameters have a pulse width of $400\ \mu\text{s}$ with a repetition rate of 20 Hz. This leads to

a duty cycle of approximately 0.8%, which is driven by the structure of the beryllium target. Advantages to this source include the ability to turn the source on and off quickly, relatively low gamma contamination (about 8-10 neutrons for every gamma), and a hard spectrum. However, a disadvantage is the relatively low time-averaged neutron flux, leading to long times of continuous operation to reach high fluences. If the community is to use this type of neutron production source for displacement damage studies, the effect of producing damage over long periods of pulsed irradiation must be well understood. It is the goal of this research to further this understanding.

1.2 Testing Si Bipolar Transistors

Si BJTs are ubiquitous semiconductor devices used in various applications including power transmission, amplification, and high-frequency oscillation [12]. There exists a significant amount of data collected over many years regarding operation of BJTs in ideal and in operational environments. For this reason, the response of these devices is well-known and highly characterized.

Transistors, specifically the Si 2N2222A n^+pn BJT, are being used instead of a novel type of semiconductor device such as III-V type transistors or carbon nanotube-based devices for a variety of reasons. The primary reason has already been mentioned; that is, the devices are very well-characterized in a large number of environmental conditions. Additionally, because these devices are so copious, it is easy to procure a large lot size for experimental considerations. By using the same lot for all experimental procedures, the variability inherent in lot-to-lot variation can be minimized [13]. While the parts tested in this dissertation research were obtained from a military-standard procured lot, transistor variability is still a consideration to make when developing experimental procedures. An additional reason for using Si is that it is an indirect bandgap semiconductor material, meaning that it does not require Liq-

uid Nitrogen (LiN) cooling or other environmental considerations to minimize system electronic noise. For all of these reasons, Si n^+pn transistors were used in this work. In essence, due to the vast knowledge and maturity of fabrication techniques, these devices allow the researcher to explore variations in effect of different environments.

1.3 Motivation

The sponsor of this research (supporting the author, with gratitude) is the Naval Surface Warfare Center (NSWC), Crane Detachment. One of the key missions of the organization is to analyze the performance of critical electronic systems and components for use in the harsh radiation environment produced by nuclear weapons, and to verify that operational performance measures are met. Due to the complexity of the electronic systems, as well as the variability and complexity of the environments, this inherently requires a substantial test base covering multiple types of radiation over a wide range of time and energy scales.

Sources for testing and analysis are varied, expensive and specialized for the nuclear weapons environment, due to the extreme fluences and short time of interaction. Testing sources can be categorized by producing ionization effects (e.g. photons and electrons) and displacements effects (neutrons and ions). These categorizations are mainly due to the different physical mechanisms of the radiation interactions and the ultimate effect on charge transport in electronics; ionizing effects can be transient, as well as accumulative, and neutron effects are generally permanent. The test environments are simulated based upon the analysis of these effects. To even more fidelity, testing and analysis are further separated by endo- and exo-atmospheric environments. This separation is largely due to the effect of the atmosphere on the energy spectrum of the radiation, especially regarding neutrons. For endo-atmospheric weapons sources, the neutrons are strongly down scattered from the initial fission

spectrum and time-broadened due to elastic collisions in the air at practical distances. Thus, a test environment must account for this variation in damage effects, and it is what makes the testing and validation of DoD systems much more rigorous than those for space operations alone.

Many sources exist for testing and analysis of pulsed ionizing effects, primarily through use of controlled pulsed electron systems (e.g MEDUSA, Utah [14]). For facilities like this, the delivery of high fluxes and short pulses are facilitated by the electron charge, which allows for electronic and magnetic field steering and focusing. NSWC, Crane, is developing an advanced dose rate facility at Indiana University which would provide a local source for conducting ionization irradiation testing and analysis; the Advanced Electron-Photon Facility (ALPHA) at Indiana University [15]. The system offers high fluxes and target irradiation sizes that not only meet the NSWC mission requirements, but also DoD and DoE dose rate survivability requirements with a narrow energy band window to allow for precision in ionization radiation effects analysis. Aside from the operational parameters, the near co-location with NSWC, Crane, will likely increase interoperability and lower overall cost per shot for testing.

Sources for endo-atmospheric testing and analysis of short pulse neutron effects on electronics are primarily accomplished at the Sandia National Laboratory Annual Core Research Reactor (ACRR). This system is suitable for such testing due to its long pulse period, flux, and moderated spectrum. Sandia has many years worth of testing and analysis using this system for pulsed neutron analysis. However, the ACRR is not a panacea, given that the proximity of the devices to the reactor does not allow for neutron only testing, and actions similar to those used in this research must be accomplished to separate ionizing and non-ionizing effects.

Since the closing of the Sandia Pulsed Reactor III [6] in September 2007, the

Department of Defense (DoD) and the Department of Energy (DoE) have put much effort into developing methods for simulating the exo-atmospheric short-pulse neutron environment [16]. Although there have been proposals for development of large, high flux, high energy (up to 14 MeV) neutron sources, much of the effort has gone to developing a physics based experimental approach that allows for the use of modeling to extrapolate to regions of interest with high fidelity and confidence. During that process, NSWC and much of the DoD have defaulted to the use of White Sands Missile Range Fast Burst Reactor (FBR) for much of their experimental validation. Although useful for validation, it has similar concerns for validation and testing due to flux, timing, and size restrictions, as well as the travel and coordination costs; and the future of the facility is the driving concern.

One of NSWCs approaches to meet their exo-atmospheric testing needs has been oriented on development of a neutron source that is relatively local, does not require special handling permits for special nuclear material, and can meet flux and timing requirements for validation of their critical components. The Neutron Radiation Effects Facility (NREF) at Indiana University (described in more detail later in this document) has strong promise for this purpose, and has many positive attributes similar to the ALPHA. The spectrum can be tailored by changing the proton energy to allow for better fidelity of spectral effects; the neutron source is relatively gamma free, which reduces the complexity of experiments; the pulses have a fast rise and fall time allowing for temporal variation in experiments; the system does not require special nuclear materials; and it is located close to NSWC. It suffers, however, from a low duty cycle (0.8%) and low flux, both requiring extensive engineering and design to improve. Furthermore, it is operated in a continuous multiple-pulse mode, possibly presenting variations in physical mechanisms that cannot be related to legacy research due in part to variation in defect formations from high instantaneous fluxes, and

short term annealing effects that may alter the outcome during the off time of the duty cycle. Experiments at this facility have shown that a detailed understanding of neutron damage in Si is not comprehensive and requires additional investigation. It is for this reason that this research is undertaken, so that decisions and efforts to engineer a better source are done with an understanding of the trade-offs and provide the nation with the simulation capabilities required to meet mission requirements.

1.4 Problem statement

The traditional method to predict the response of bipolar junction transistors that have been subjected to displacement damage from neutrons is using the Messenger-Spratt equation [17]. However, this equation is usually applied to short, single-pulse irradiation environments. The first question answered in this dissertation is: does defect annealing during irradiation affect the end result and, if so, can it be corrected?

Additionally, the neutron spectrum is often collapsed down into an equivalent mono-energetic spectrum with a corresponding damage constant. The second question asked in this work is whether the neutron spectrum shape will affect the damage response in Si BJTs.

To address these questions, the work is broken up into three pieces:

1. Develop a model that tracks bulk defect species concentrations so that the current gain in a BJT can be predicted with acceptable accuracy for a variety of input spectra and time profiles.
2. Answer the question of whether a BJT damaged in an accelerator-driven neutron source facility will follow the Messenger-Spratt response.
3. Collect empirical evidence of whether or not the spectral shape affects the response by using different facilities to irradiate the same type of BJT.

References

1. J. Kelly, P. Griffin, and W. Fan, “Benchmarking the Sandia Pulsed Reactor III cavity neutron spectrum for electronic parts calibration and testing,” *IEEE Trans. Nucl. Sci.*, vol. 40, no. 6, pp. 1418–1425, December 1993.
2. M. Oliver, “PIN diode and neutron spectrum measurements at the army pulse radiation facility,” *IEEE Trans. Nucl. Sci.*, vol. 41, no. 6, pp. 2132–2138, December 1994.
3. D. Luera, TF; Welch, “Output characteristics of the white sands missile range fast burst reactor,” *Nuclear Effects Directorate, Army Missile Test and Evaluation, White Sands Missile Range, New Mexico*, 1970.
4. V. Rogers, L. Harris, D. Steinman, and D. Bryan, “Silicon ionization and displacement kerma for neutrons from thermal to 20 MeV,” *IEEE Trans. Nucl. Sci.*, vol. 22, no. 6, pp. 2326–2329, Dec. 1975.
5. A. Gavron, “Design of a subcritical multiplying low-enriched uranium externally driven neutron assembly at the Los Alamos Neutron Science Center,” Los Alamos National Laboratory, Tech. Rep. LA-UR-08-6256, 2008.
6. (2007, September) Sun sets on Sandia Pulsed Reactor. News Release.
7. ASTM Standard E722-09(e1), *Standard Practice for Characterizing Neutron Energy Fluence Spectra in Terms of an Equivalent Monoenergetic Neutron Fluence for Radiation-Hardness Testing of Electronics*, ASTM International, West Conshohocken, PA, 2009.
8. L. Choate and T. Schmidt, “New neutron simulation capabilities provided by the Sandia Pulse Reactor-III (SPR-III) and the upgraded Annular Core Pulse Reactor (ACPR),” *IEEE Trans. Nucl. Sci.*, vol. 25, no. 6, pp. 1625–1628, Dec. 1978.
9. E. Bielejec, G. Vizkelethy, N. Kolb, D. King, and B. Doyle, “Damage equivalence of heavy ions in silicon bipolar junction transistors,” *IEEE Trans. Nucl. Sci.*, vol. 53, no. 6, pp. 3681–3686, 2006.
10. J. Reijonen, “Compact neutron generators for medical, home land security, and planetary exploration,” in *Proceedings of Particle Accelerator Conference*, Knoxville, TN, 2005.
11. J. Fantidis, B. Dimitrios, P. Constantinos, and V. Nick, “Fast and thermal neutron radiographies based on a compact neutron generator,” *J. Theor. Appl. Phys.*, vol. 6, p. 20, 2012.
12. B. Brar, G. Sullivan, and P. Asbeck, “Herb’s bipolar transistors,” *IEEE Trans. Elect. Dev.*, vol. 48, no. 11, pp. 2473–2476, November 2001.

13. R. Berger, J. AzAzarewicz, and H. Eisen, “Hardness assurance guidelines for moderate neutron environment effects in bipolar transistors and integrated circuits,” *IEEE Trans. Nucl. Sci.*, vol. 25, no. 6, pp. 1555–1560, December 1978.
14. V. Harper-Slaboszewicz, E. Hartman, M. Shaneyfelt, J. Schwank, and T. Sheridan, “Dosimetry experiments at the MEDUSA Facility (Little Mountain),” Sandia National Laboratory, Tech. Rep. SAND2010-6771, 2010. [Online]. Available: <http://prod.sandia.gov/techlib/access-control.cgi/2010/106771.pdf>
15. (2014, July) Indiana University ALPHA. Indiana University. [Online]. Available: <http://www.indiana.edu/~estor/>
16. G. Hennigan, R. Hoekstra, J. Castro, D. Fixel, and J. Shadid, “Simulation of neutron radiation damage in silicon semiconductor devices,” Sandia, Tech. Rep. SAND2007-7157, October 2007.
17. G. Messenger and J. Spratt, “The effects of neutron irradiation on silicon and germanium,” in *Proc. IRE*, vol. 46, June 1958, pp. 1038–1044.

II. Theory

In this portion of the document, the underlying theory that will be necessary to understand the overarching goals of the research will be presented. As such, the main focus will be on semiconductor physics, defect formation in semiconductors, and radiation damage mechanisms in silicon devices. In addition, a description of radiation environments and electronics hardness testing will be laid out.

2.1 Basic Semiconductor Physics

Material Classification.

All solid materials can be categorized into three main electrical classes: conductors, insulators, and semiconductors [1]. These materials are classified in this way based on a number of electrical properties, one of which is the conductivity. Conductors have such high conductivity, and inherently low resistivity, that electrons can easily travel through the material, when induced to do so, with little loss of energy [2]. Conversely, insulators have extremely low conductivity and, thus, electrons have difficulty moving throughout the material. In the middle, the conductivity of semiconductors is strongly dependent on available carriers, as presented by doping concentration or applied fields.

Another way to classify crystalline solids is by the band-gap energy between the valence and conduction bands, which is presented in the chart in Figure 2. This gap arises because, as the atoms in the solid form bonds, energy bands form with a forbidden region in between. Electrons can occupy the lower, or valence, band or, if given enough energy, they may be found in the higher, or conduction, band. The band-gap energy, E_g , is the width of the forbidden region between these two bands.

In a conductor, the conduction band may be partially filled or it may overlap

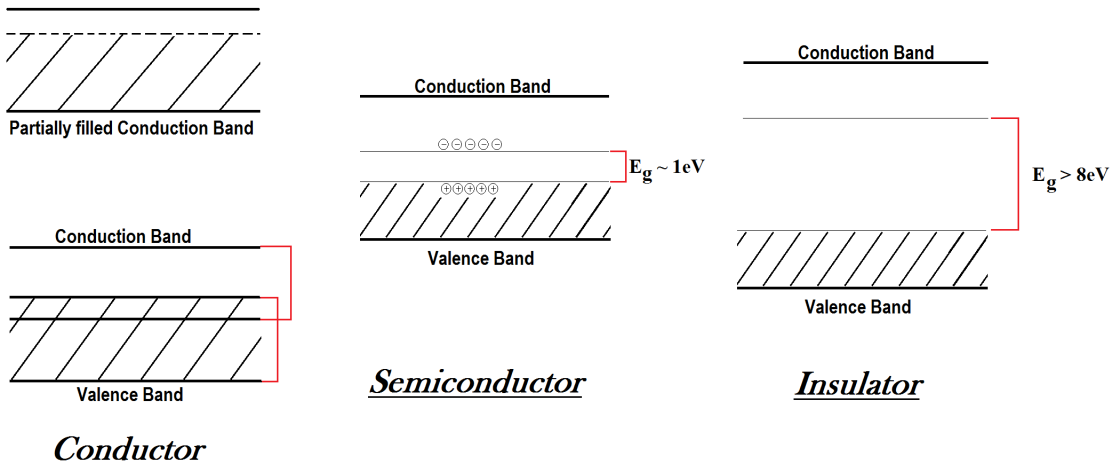


Figure 2. A schematic of the energy bands for a conductor (left) with a partially filled conduction band (top) and with overlapping valence and conduction bands (bottom), a semiconductor (middle), and an insulator (right). (Figure derived from [3].)

with the valence band, and electrons can easily move throughout the solid with little resistance. In an insulator, the band-gap energy is very large, so electrons need significant energy to occupy the conduction band. A semiconductor occupies the “goldilocks” region; the band-gap energy is small enough that some electrons may be excited from the valence band to the conduction band by thermal energy or an applied electric field but not so small that all do.

When an electron is excited into the conduction band, it leaves behind a *hole* in the valence band. Despite physically being *the lack of something*, this hole is treated as a particle and is the opposite of the electron. While the electron (with the symbol e^-) is considered the carrier of negative charge, the hole carries positive charge, and is often delineated by the symbol h^+ . In the calculation of semiconductor properties and performance parameters, electrons and holes are the primary negative and positive *charge carriers*, respectively.

Doping of Semiconductor Material.

In an ideal Si semiconductor, the crystal is a perfect lattice of silicon atoms, each one covalently bonded to 4 others. This is called the *intrinsic* semiconductor state. In this state, the Si carrier concentration is approximately 10^{10} cm^{-3} and is approximately equal in electrons and holes.

The introduction of impurities into the semiconductor changes the carrier transport characteristics. The impurities must lie within the silicon bandgap in order to act as either donors or acceptors. For a donor, the impurity electron energy typically lies close to the conduction band so that, with very little thermal energy, almost 100% of their electrons are excited into the conduction band. This creates a significant increase of negative charge carriers in the conduction band. Similarly, for an acceptor, the impurity usually lies near the valance band and accepts electrons from the valence band with very little thermal energy required, which subsequently adds additional holes to the semiconductor material. Figure 3 displays some of the more common impurities added to silicon semiconductors as well as their position within the bandgap.

When at thermal equilibrium, the concentration of electrons and holes in an *n*-type extrinsic (doped) semiconductor is described by the equation

$$n_i^2 = np = (N_C N_V) e^{-E_g/kT} \quad (1)$$

where n_i is the intrinsic carrier concentration; n and p are the electron and hole concentrations, respectively; N_C and N_V are the effective density of states in the conduction and valence bands, respectively; E_g is the band-gap energy for the semiconductor; k is the Boltzmann constant; and T is the temperature.

When a semiconductor material is doped, its intrinsic qualities, such as carrier mobility and diffusivity, change.

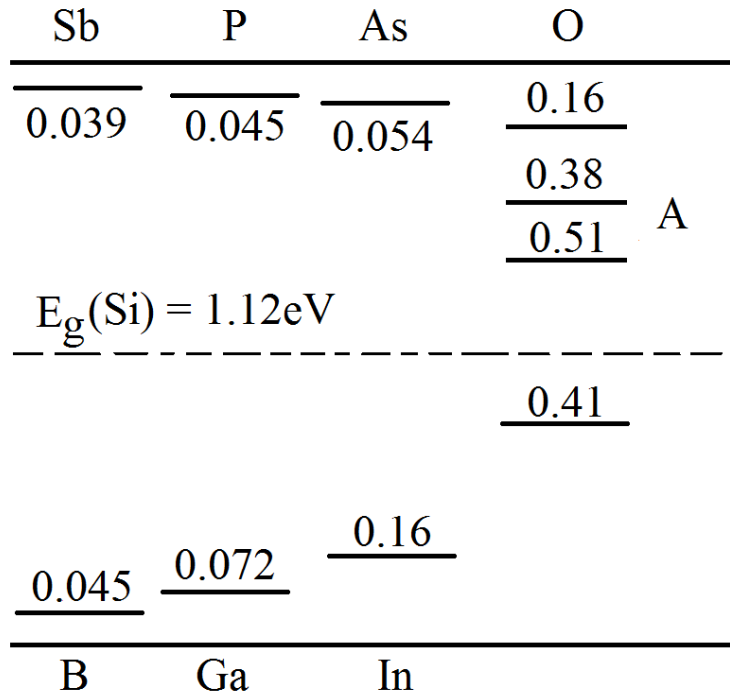


Figure 3. Measured ionization energies for select acceptors and donors in Si (in eV). Below the Fermi level, impurities are acceptors (unless otherwise noted); above the Fermi level, impurities are donors. (Figure derived from [3].)

Semiconductor Junctions.

When a *p*-type region is brought in contact with an *n*-type region, the result is called a junction. At this junction, if it is abrupt, a region of space charge develops. In his 1949 paper [4], Shockley succinctly describes a *pn* junction. In this work, a simple dopant profile leads to two separate regions (*p*- and *n*-type) with a transition region in between.

Due to diffusion and the spatial variation of charge distribution, electrons in the *n*-type material drift to towards the *p*-type just as holes move in the opposite direction. The width of this region is highly dependent on quantities such as the built-in voltage, V_{bi} , and the dopant concentration in the lighter-doped region, N_B . The depletion width, W , is described by

$$W = \sqrt{\frac{2\epsilon_s (V_{bi} - V)}{qN_B}} \quad (2)$$

where ϵ_s is the permittivity, V is an applied external voltage, and q is the elementary charge constant ($1.602 \times 10^{-19} C$). In real world applications of *pn*-junctions, the abrupt junction is not possible; however, it is often used as an approximation to simplify calculations.

The junction is a key inspection point, as much of the focus on displacement damage in a silicon bipolar junction transistor is put on the emitter-base junction. Defects in this region can affect the diffusion of charge carriers, which in turn affects the device's performance. This will be discussed in greater detail further in this document.

Semiconductor Device Types & Applications.

Elemental semiconductors such as germanium and silicon are most often used as radiation detectors. Additionally, germanium is used extensively as a gamma spectrometer. However, because of the small band-gap energy, it must be operated at low temperatures (~77K) to minimize electronic noise. Because of the small band-gap energy, thermal energy at room temperature provides enough energy to electrons in the valence band that they jump to the conduction band, providing a distorted signal. Silicon strip detectors are the choice of high-energy physics projects such as the Linear Hadron Collider (LHC). The larger band-gap energy and the fact that silicon is an indirect semiconductor, which means that energy *and* momentum must be applied to an electron for excitation to the conduction band, leads to low-noise operation at room temperature.

More often, semiconductor devices are created with junctions between *p*- and *n*-type regions. To be considered one or the other, the semiconductor region must be

doped with donors or acceptors so that there are more electrons in the conduction band (*n*-type) or more holes in the valence band (*p*-type) than are expected in an intrinsic semiconductor. Figure 3 displays select ionization energies for both donors and acceptors in silicon.

The *pn*-junction is the fundamental building block for the BJT. The BJT has been used extensively in high-speed analog and digital circuits, predominately as a current amplifier. These devices typically have three regions: the collector, the base, and the emitter; and these regions interact through the *pn* or *np* junctions. In the case of a silicon *p*⁺*np* transistor, the substrate is grown as lightly-doped *p*-type and acts as the collector. Next, *n*-type dopants are diffused into the substrate to create an *n*-type base region. Finally, a heavily-doped *p*-type region is diffused into the *n*-type base to create the emitter. Metal contacts are attached at each region to facilitate carrier flow. A schematic of an idealized *n*⁺*pn* BJT is displayed in Figure 4. For an *p*⁺*np* BJT, regions of *n*-type doping are replaced by regions of *p*-type, and *vice versa*.

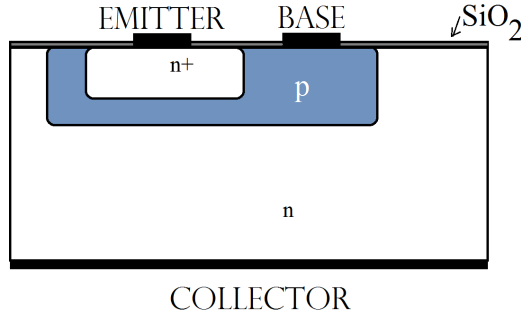


Figure 4. A schematic view of an idealized *n*⁺*pn* bipolar junction transistor. The silicon dioxide is used to passivate the surface boundary. (Figure derived from [3].)

In a BJT, charge carriers are classified as either the *majority* or *minority* carrier based on the extrinsic state of the device region. So, for example, in the emitter region of an *n*⁺*pn* BJT, which is *n*-type and doped with elements such as P or arsenic, the majority carrier is the electron while the minority carrier is the hole. However, as the

electron travels from the emitter into the base, which is *p*-type and may be doped with elements such as boron or gallium, it becomes the minority carrier.

When in thermal and electronic equilibrium, *i.e.* room temperature and no voltage bias applied to the device leads, the band structure of an n^+pn BJT would be represented as in Figure 5. There is band bending at the junctions due to the effect of space charge in the depletion region. The *Fermi level*, E_f is constant and its relationship with respect to the conduction and valence band is based on the carrier concentrations, which are affected by dopant levels in each region.

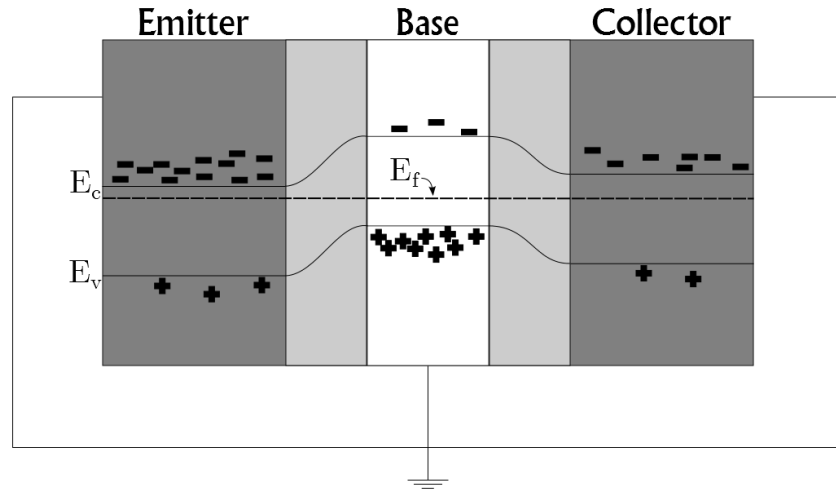


Figure 5. The Fermi level, E_f , is continuous across the entire bandgap schematic of an idealized n^+pn BJT in thermal and electronic equilibrium.

If a potential is applied to various regions of the BJT, the Fermi level is perturbed. An example of the n^+pn BJT from Figure 5 with positive bias applied to the collector and negative bias applied to the emitter is displayed in Figure 6. The positive potential applied to the *n*-type collector region causes the overall potential to decrease and puts the base-collector junction in reverse bias. Alternatively, the negative bias applied to the emitter causes the opposite effect, causing the base-emitter junction to operate in forward bias. For this particular configuration, the BJT is in *active mode*. A table of the four BJT modes is displayed in Table 1.

Table 1. Modes of BJT operation.

Base-Emitter Junction Bias	Base-Collector Junction Bias	Applied Voltages	Mode
Forward	Reverse	$E < B < C$	Forward-Active
Forward	Forward	$E < B > C$	Saturation
Reverse	Reverse	$E > B > C$	Cut-Off
Reverse	Forward	$E > B > C$	Reverse-Active

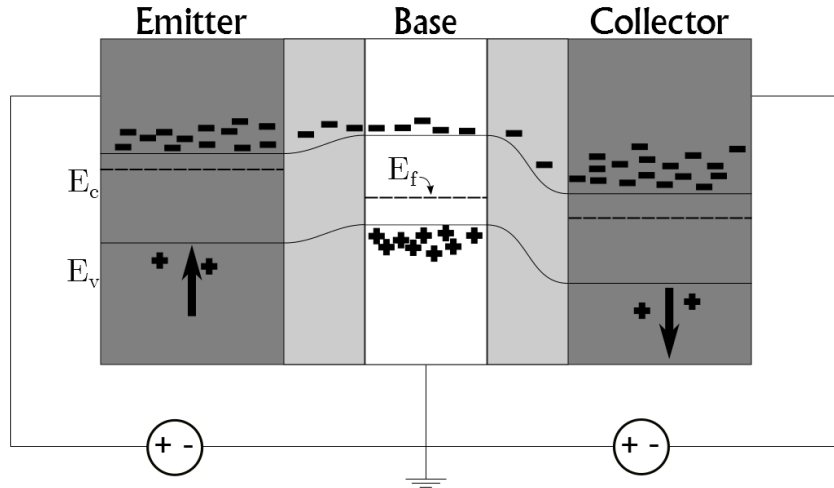


Figure 6. The BJT bandgap shifts as bias is applied. In this case, positive voltage is applied at the emitter, and negative voltage is applied to the collector while the base is kept at ground.

The BJT, specifically the current amplification BJT with the designation 2n2222A, is the semiconductor device that will be studied extensively in this research. For non-ionizing radiation, the base region is of greatest interest. As early as 1964, Goben and his colleagues reported a neutron-induced base current component which increases in proportion to neutron fluence [5–7]. This base current component is primarily responsible for gain degradation because of degradation of the emitter efficiency [8].

Current gain is one of the most important device properties that can be measured for the 2n2222A BJT. When in active mode, electrons from the emitter are injected into the base since the emitter-base junction is forward biased. If the base width is small compared with the diffusion length of the minority carriers (in this case,

electrons), most of the electrons survive and make it to the collector region [9]. This is often done intentionally to maximize carrier transport properties. The current gain, which can be called β or h_{fe} , is defined as $\beta = h_{fe} = I_c/I_b$ where I_c is the collector current and I_b is the base current.

To help further define the current gain, Figure 7 displays a schematic of the currents inside a BJT. The forward biased junction at the emitter-base interface injects electrons into the base where they diffuse, and this injected current of electrons is named I_{e_n} . Additionally, there is a current of holes in the emitter, I_{e_p} that, when considered together with the electron current, makes up the total current in the emitter. The electrons that do not recombine, surviving to the collector, make up the current of electrons in the collector, or I_{c_n} .

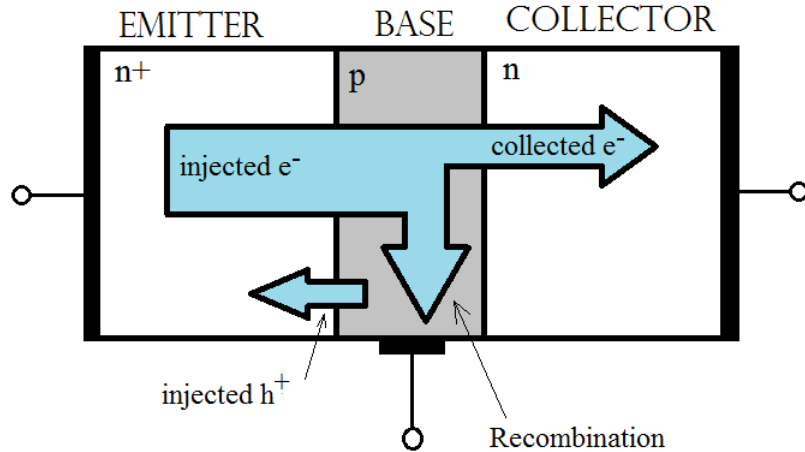


Figure 7. Idealized schematic of electron and hole currents in an n^+pn BJT.

To calculate h_{fe} , the base transport factor (α_T) and the emitter injection efficiency (γ) are necessary, as displayed in Equation Set 3.

$$\begin{aligned}
\gamma &= \frac{I_{e_n}}{I_{e_n} + I_{e_p}} \\
&= \left[1 + \left(\frac{p_{nE_o} D_{p_E} L_n}{n_{pB_o} D_{n_B} W_e} \right) \tanh \left(\frac{W_b}{L_n} \right) \right]^{-1} \\
\alpha_T &= \frac{I_{c_n}}{I_{e_n}} \\
&= \left[\cosh \left(\frac{W_b}{L_n} \right) \right]^{-1}
\end{aligned} \tag{3}$$

In Equation Set 3, p_{nE_o} and n_{pB_o} are the minority carrier concentrations for emitter and base, respectively; D_{p_E} and D_{n_B} are the diffusivity of the minority carriers for emitter and base, respectively; L_n is the diffusion length of electrons in the base; and W_b and W_e are the physical widths of emitter and base, respectively. The diffusion length is a measure of the average distance that an electron can travel from birth to recombination and is defined as $L = \sqrt{D_{n_B} \tau}$, where τ is the minority carrier lifetime.

The current gain in a semiconductor is then defined as

$$\beta = h_{fe} = \frac{\alpha_T \gamma}{1 - \alpha_T \gamma}. \tag{4}$$

It is β that will be the main focus of the empirical data collection efforts in this research. Since a number of the parameters that go into calculating it are affected by non-ionizing radiation, it will provide the best metric of damage in the 2N2222A Si BJTs.

2.2 Semiconductor Defects in Silicon

At the most basic level, the primary defect mode in solid state semiconductors is the Frenkel pair [1]. This type of defect is created when enough energy is transferred to an atom in the crystal lattice of the material so that it is relocated from its initial location. Often, this energy is deposited in the crystal lattice via incident particle

collisions, as in the case of neutrons colliding with silicon atoms in a single crystal. This relocation causes a *vacancy* defect at the initial location. Additionally, the displaced atom becomes an *interstitial* defect if its final resting place is not at the appropriate lattice-aligned location. The defects thus created become charge carrier traps that may act as recombination sites for electrons and holes if they lie within the bandgap. In essence, these defects become allowed states within the forbidden region of the semiconductor bandgap, increasing the possibility of recombination as electrons and holes drift and diffuse through the bulk material. Figure 8 is a schematic of the Frenkel pair creation that illustrates this process using neutron irradiation of the crystal lattice.

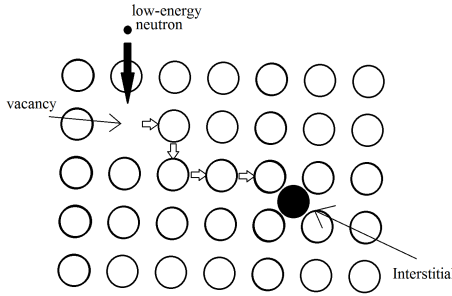


Figure 8. Schematic of the creation of a Frenkel pair (in this case using low-energy neutron bombardment of the crystal lattice). [10]

As the bombarding particle travels into the material, it collides with a stationary lattice atom, imparting energy and dislodging the atom. The electron may be absorbed or may continue on through the bulk, potentially colliding and causing other dislocations. The original atom is bumped out of place (diagonal arrow in Figure 8) where it replaces the atom at that site. This process may continue many times until the final atom comes to rest in between lattice sites (filled in circle in Figure 8). The time scale for this process is short and is often less than 10^{-7} seconds [11].

In addition to Frenkel pairs, there are other combinations of defects that are known by other names. Two vacancies adjacent to one another form a di-vacancy.

It is possible, but less common, for the same phenomenon to occur with interstitials, forming a di-interstitial. Also, it has been found that vacancies and interstitials in silicon act as drivers for various diffusion mechanisms; they can interact with impurities in the crystal to form complex defects [12]. One common example is the vacancy-phosphorus pair, known as the E center in irradiated Si [13]. This is quite common in *n*-type semiconductor material, as P is a very common donor atom. The result of defect formation in semiconductors is the insertion of allowable energies in the forbidden bandgap.

Table 2 presents a small selection of the more common defects as collected by Myers et al. [14]. In the table, ΔE is the activation barrier for electron and hole emission, σ is the capture cross section for electrons and holes, D_o is the diffusion prefactor, and E^d is the diffusion activation energy. In their study, Myers used this information to calculate clustering in pulsed-neutron irradiated silicon. The list of defects selected here displays some of the most common defects, but it is a very small portion of the total list. It is included here to show the complexity of defect formation.

Table 2. Select defect species and their electronic parameters. Here e^- denotes the conduction electron and h^+ denotes the hole, V is the vacancy, the subscript I denotes an interstitial atom, and charge states are indicated by superscripts. (Derived from [14])

Species	ΔE^e	ΔE^h	σ^e	σ^h	D_o	E^d
	[eV]	[eV]	[cm ²]	[cm ²]		
Si_I^0	0.62	0.86	3×10^{-15}	3×10^{-15}	10^{-3}	0.17
Si_I^{+1}	0.47	0.50	3×10^{-14}	3×10^{-16}	10^{-3}	0.50
Si_I^{-1}	0.26	1.01	3×10^{-16}	3×10^{-14}	10^{-3}	0.29
V^0	1.07	0.72	3×10^{-15}	3×10^{-15}	1.3×10^{-3}	0.45
VV^0	0.91	0.71	3×10^{-15}	3×10^{-15}		
B_I^0	0.13	0.75	3×10^{-15}	3×10^{-15}	2.3×10^{-5}	0.53
VP^0	0.85	0.68	3×10^{-15}	3×10^{-15}		

Shi et al. [15] found that initial defect formation is over on a nanosecond time

scale. In their work, they determined that after about 10^{-10} s, recombination and divacancy production are independent of a production constant, indicating that most of the interstitials and vacancies have annihilated. It is for this reason that the model that was developed in this research only included a generic *generation* term since the initial movement of silicon ions is over on such short time scales. The resulting defects then migrate under different mechanisms, and this behavior is the focus of the model.

Defect Clusters.

The most common damage mode in a fast-neutron irradiation is the defect cluster. While they still are not fully understood, there is extensive experimental data proving their existence including transmission electron microscopy (TEM) observations. They have been observed for silicon ion bombardment [16], medium [17] and heavy [18,19] ions, protons [20], and electrons [21].

In this mode, a significant amount of kinetic energy is deposited in the Primary Knock-on Atom (PKA). The PKA causes secondary and tertiary collisions in the surrounding lattice, depositing and dissipating energy in the form of thermal energy [22]. In Figure 9 is displayed a representative track for a PKA given a starting kinetic energy of 50 keV at the origin. There are a few very energetic collisions that give rise to other high-energy recoils, but low-energy transfers are more common. The lower-energy transfers often create Frenkel pairs that coalesce into stable defect clusters [15]. Each track path ends in a terminal cluster [23].

Gossick [25] proposed a physical model regarding defect clusters that involved a disordered volume surrounded by a depletion region. This occurs because the highly disordered region (defect cluster) captures majority carriers from the surrounding bulk, creating opposing space charge. Subsequent work from Bertolotti observed this phenomenon using electron microscopy and etching [26].

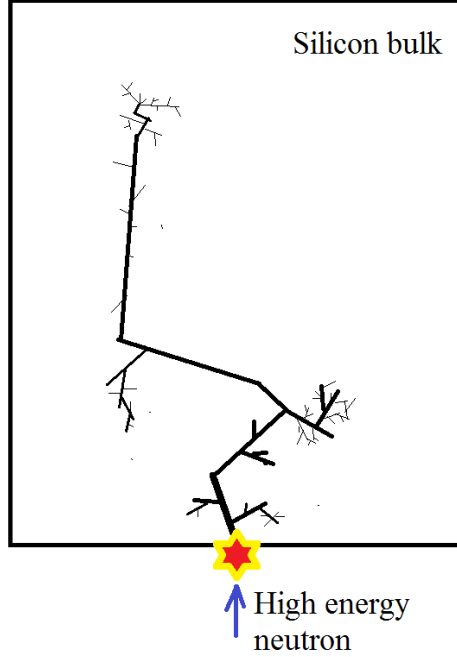


Figure 9. Recreation of a typical history track of a 50 keV recoil atom in silicon produced using a Monte Carlo simulation. [24]

Defect formation is thought to be energy dependent, meaning that the number of defects and the number of clusters that form depends on the PKA recoil energy. If a neutron deposits barely sufficient energy to cause a Frenkel pair, called the *threshold energy for displacement*, a simple defect forms. The threshold energy for silicon is about 20 eV [28]. However, for a fast neutron (one with higher energy) that deposits its energy to a silicon atom, it can create many thousands of defects which cluster as shown in Figure 9. This damage anneals in the short-term (up to about 10^3 seconds), as well as long-term.

Short Term Annealing.

The displacement damage caused in a BJT subjected to neutron irradiation under standard temperature (300K) usually finishes short-term annealing on the order of 10^3 seconds. Before this time, the clusters rearrange due to both thermal effects and injection annealing. It is important to note that, during this time, the damage

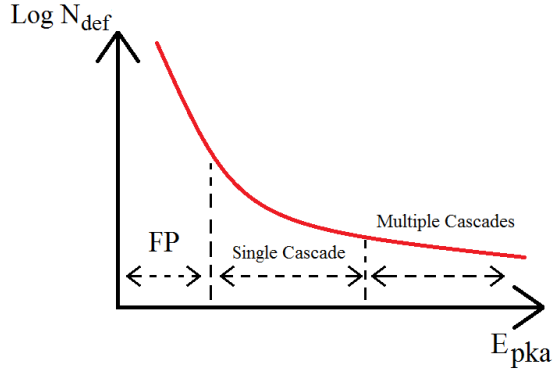


Figure 10. Schematic representation of defect and subcascade formation as a function of PKA energy. The y-axis of the plot is logarithmic and representative of the number of interactions [27].

constant is greater than for when the device is stable.

One measure of damage in the short term, *i.e.* before reaching the stable damage condition, is the annealing factor defined by Sander and Gregory [29–32] as

$$AF(t) = \frac{\beta(t)^{-1} - \beta_o^{-1}}{\beta_{\infty}^{-1} - \beta_o^{-1}}. \quad (5)$$

In Equation 5, β is the device gain, β_o is the pre-irradiation gain, and β_{∞} is the gain “at infinite time” which is usually simulated by performing an 80°C thermal annealing bake for 2 hours. Binder et al. [33] conjectured that the short term annealing is governed by a second order recombination of mobile and immobile defects inside a spherical defect cluster. The rapid recombination reaction is slowed down by diffusion out of the cluster.

The annealing factor is affected by temperature [34], injection level [35], and neutron energy levels. The short term annealing process is thermally activated, with longer decay times at lower temperatures [36]. This is due to the extra energy imparted to the lattice at higher temperatures and increases vibrational energy, which rearranges the defects faster.

In *p*-type silicon, high current injection causes the defects to anneal out of the

device faster. Conversely, in *n*-type silicon, high injection causes annealing to proceed more slowly [37]. The difference in annealing factor due to material type is attributed to higher vacancy mobility in its negative charge state [24]. This will have a great affect on the results as the *in situ* measurements will require the devices to be powered on, increasing current injection.

Finally, the annealing factor depends on the energy of the neutrons that are irradiating the silicon device. Srour and Curtis [38] found that the ratio of the annealing factor for 14 MeV neutrons to thermal neutrons at 10^{-2} s was about 1.25. However, at about 1 s, this difference is negligible.

In 1981, McMurray and Messenger [35] fit the device annealing factor to an analytical expression that was derived from an empirical nomograph. This equation is stated by Wrobel and Evans [39] as Equation 6.

$$AF = 1 + 230 \left[n_i \int_0^{\tau+t} \exp \left\{ \frac{qV_{be}(t)}{2kT} \right\} dt \right]^{-0.2} \quad (6)$$

where

t = time to device turn on [s],

τ = rise time of the injection signal [s],

n_i = intrinsic carrier concentration,

q = elementary charge constant = 1.62×10^{-19} [C],

k = Boltzmann's constant, 8.62×10^{-5} [ev/K],

T = temperature of operation [K],

$V_{be}(t)$ = base-emitter voltage [V].

It must be noted that this work was done using a high-flux, single pulse, fast-burst

reactor based neutron source. This will be compared to the results of such analysis done in different facility types to see how the annealing factor changes.

2.3 Radiation Environments and Hardness Testing

Semiconductors are used in a wide variety of applications that lead to their use in an equally wide variety of environments. Extremes of temperature, humidity, pressure, and other environmental variables are not uncommon for their operation. Radiation environments are no exception. Take, for example, the environment on a space-borne satellite. Charged particles from the Earth's Van Allen belt, gamma photons and protons from the sun, and exotic cosmic particles from space are a constant radiation source, which is time dependent.

For this reason, radiation hardness testing must be accomplished to determine the range of adverse conditions under which the devices will continue to operate. This testing may take many forms, depending on the device and environmental expectations. No matter the form, however, the testing is necessary to completely understand the operational limits of the devices in question.

Obviously, if operations in extreme environments are being tested, it is not always possible to test in the *exact* environment. As an example, the South Atlantic Anomaly (SAA) is a region of the world where the Earth's magnetic field and, thus, the Van Allen belts dip to less than 200 km from the surface [40]. For fiscal and logistical reasons, it would not be viable to test every lot of BJTs created for use in a satellite by sending a rocket into orbit with a sample set in its cargo bays and bound for the SAA. In addition, the devices often need to be tested for longevity, *e.g.* spending many years passing through the SAA. Experimenters could not wait for each batch to run their 20 year lifetime before sending the *actual* satellite into space. Therefore, the test environment often needs to be accelerated by increasing the flux to reach the

expected fluence faster. More feasible test-beds must be developed so that multiple, repeatable experiments can be undertaken to test for the environmental hardness.

Another key environment for military and civilian uses of transistor components is that of a nuclear weapon. This environment is extremely harsh with a short duration (but high flux) pulse of neutrons, gammas, x-rays, and charged particles. International law forbids detonating nuclear weapons for verification, thus there is a strong desire to find similar or comparable radiation testing environments for verification testing. Additionally, the neutron flux and spectrum shape are unique to the nuclear weapon environment, making it difficult to replicate.

In this work, only radiation hardness is investigated. Therefore, in the following sections, the testing for neutron displacement damage studies will be discussed in detail, and a few of the facilities that are used for neutron radiation testing will be described.

Description of hardness testing.

Radiation hardness testing is the act of evaluating a device or piece of equipment to understand the influence of radiation on its performance. The environment may single out a particular radiation or particle type, or it may be a test bed mixed radiation environment designed to more closely replicate the environment of interest, and thus, the real-world application of the device. These types of testing are done for different reasons; often they are done concurrently to fully understand device performance. By singling out a particular type of radiation, the experiment can provide information related to a particular damage mechanism. Otherwise, by including as many particle types as the environment of interest, the experiment may create coupling effects not measured when singling out particular particles. In some cases, the method by which the particle of interest is created at the facility leads to the creation of secondary

particles. These, and many other considerations must be made when selecting a facility used for radiation hardness testing.

Radiation Testing Facilities.

There are a variety of radiation testing facilities that have been developed to test electronic devices and systems of devices. They can be classified by the type of particle(s), radiation(s), or energy of radiation.

For charged particles, cyclotrons, linear accelerators, and their variations are most common. An example includes the Indiana University Cyclotron Facility, a schematic of which is found in Figure 11. Charged particles are relatively easy to work with, since they can be controlled and manipulated using electric or magnetic fields.

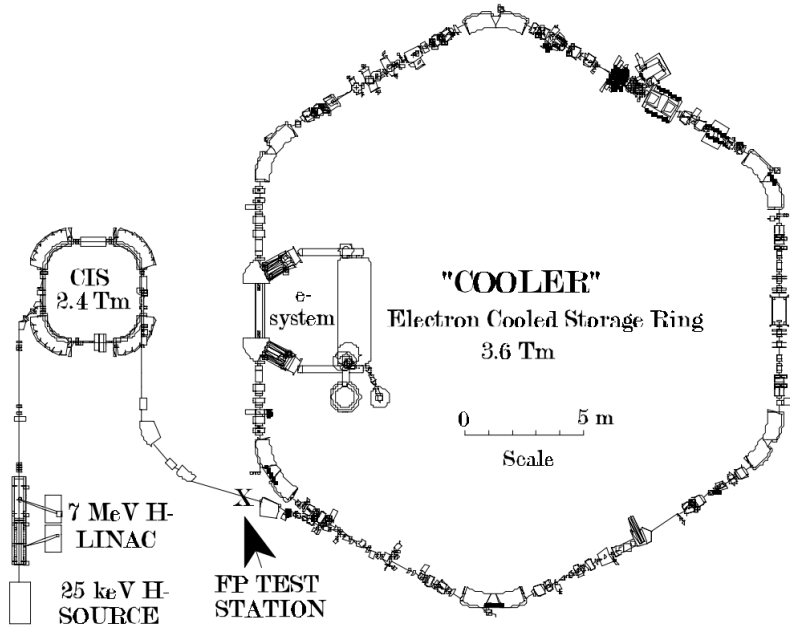


Figure 11. A schematic of the IUCF cyclotron is a proton accelerator that can provide 20 ns pulses of 200 MeV protons at about 2×10^{10} rad(Si)/s [41].

For a gamma *only* environment, facilities typically use radioactive materials that decay by gamma emission, often ^{60}Co . By choice of radioactive material and radioactivity, the experimenter can select the important energy and dose rate desired.

Mixed-radiation fields that include gamma rays result from reactions that provide direct or indirect emission of gamma photons. As an example, in a nuclear reactor, 2-3 neutrons are produced for each fission of ^{235}U . In addition to these 2-3 neutrons, energy is released in the form of gamma rays. The fission products are generally radioactive and often decay by gamma emission as well. In nuclear reactors, the gamma dose rate can be 8-10 times that of the neutron dose.

There are also many facilities that are capable of creating exotic particles, such as positrons or muons. These will not be discussed here, but they are prevalent in the academic community. They are not of much interest for radiation effects experiments.

It is very difficult for a neutron irradiation facility to provide an environment free of radiation other than neutrons. Therefore, for neutron irradiation testing, mitigation techniques must be used. In this research, two different facility types were used to induce displacement damage in silicon devices: the thermal neutron research reactor at the Ohio State Research Reactor (OSURR) and the IU Neutron Radiation Effects Facility (NREF). They are described in greater detail in the following sections.

Ohio State University Research Reactor.

This system consists of a light water, pool-type, thermal research reactor. It is licensed to operate up to 500 kW and, at maximum steady-state power, the average thermal neutron flux is approximately 5×10^{12} n/cm²/s.

There are a number of separate sub-facilities within the reactor core, displayed in Figure 12, that allow for different spectra and flux rates. The Central Irradiation Facility (CIF) has an inner diameter of 1.3 inches and extends from the top of the pool down to a central grid position within the core [42]. It has a maximum total flux of 2.3×10^{13} n/cm²/s and a maximum 1-MeV Equivalent (Si) flux of 4.52×10^{12} n/cm²/s with a hardness of $H = 0.20$. The calculation of 1-MeV Equivalent (Si) flux and the

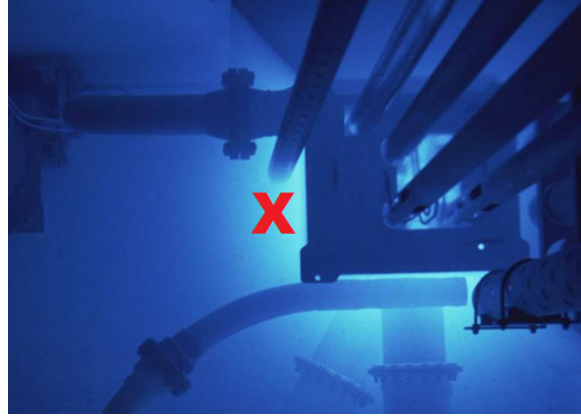


Figure 12. Reactor Core at the OSURR shows multiple irradiation facilities (CIF, AIF, PIF) as well as beam ports for external set-up and irradiation.

determination of hardness is accomplished using the method described in Section 2.3. The Auxiliary Irradiation Facility (AIF) is larger, at 2.5 inches in diameter, but the maximum fluxes are lower at $\phi_{tot} = 9.4 \times 10^{12}$ n/cm²/s and $\phi_{1-MeV} = 2.44 \times 10^{12}$ n/cm²/s with a hardness of 0.27. An advantage of this is that the gamma flux is also lower. The Peripheral Irradiation Facility (PIF) is also 2.5 inches in diameter and in a different position, with a maximum total flux of 5.3×10^{12} n/cm²/s.

Finally, a 7 inch tube can be moved anywhere in the reactor pool, but the standard position allows a maximum total flux of 1.5×10^{12} n/cm²/s and a 1-MeV Equivalent (Si) flux of 1.92×10^{11} n/cm²/s with a hardness of 0.13 and a gamma dose of 6.5×10^4 rad(Si)/hr. The maximum flux and hardness decreases because the 7 inch tube is positioned the furthest from the center of the core when compared with the other tubes. The additional distance leads to additional neutron thermalization as neutrons travel through the cooling water. The spectrum has been calculated using Monte Carlo simulations, and the calculations have been verified using foil activation analysis and spectrum unfolding using the Spectrum Analysis by Neutron Detectors (SAND-II) code [43]. The spectrum in the 7 inch tube is displayed in Figure 54.

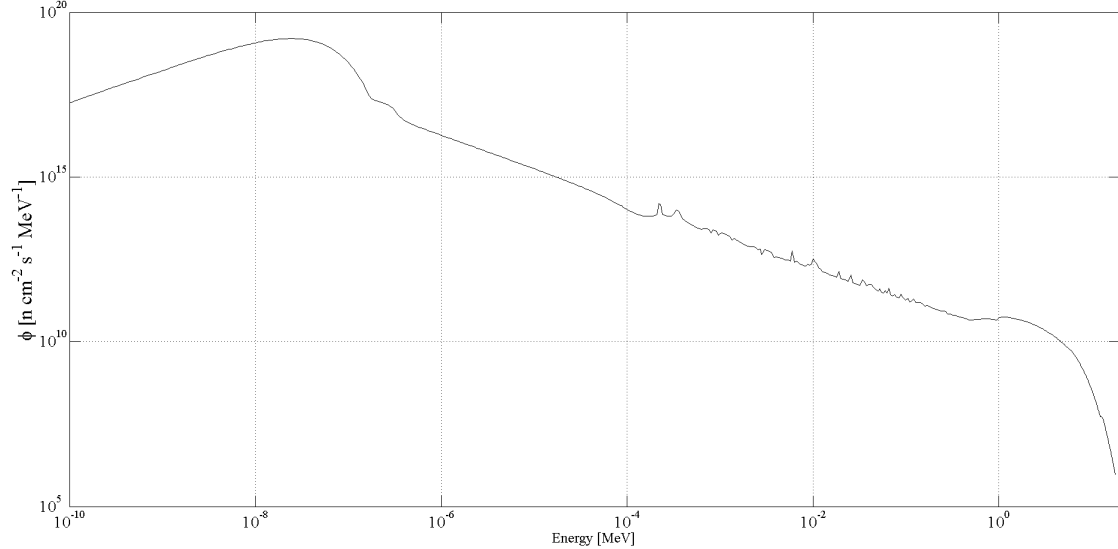


Figure 13. Neutron differential flux spectrum at the OSURR 7 inch tube at full power where the 1-MeV equivalent (Si) flux at this power level is 1.92×10^{11} n/cm²/s and the hardness is 0.13.

Indiana University Neutron Radiation Effects Facility.

At the IU CEEM, there is a pulsed neutron source that produces neutrons via the inelastic scattering of protons on beryllium. One of the two targets is used for neutron radiation effects in electronics studies, and it is called the NREF. A schematic of the facility is displayed in Figure 14.

The following description is taken from the Master's thesis of M.R. Halstead [44]:

Protons are created in an ion source, then are accelerated and directed onto a target assembly inside a moderator/reflector stack where neutrons are created. Each of these steps will now be explained in greater detail.

The protons are created by stripping an electron from elemental hydrogen in the ion source, displayed in the lower left corner of Figure 14. These protons are collected and focused into a 3 MeV Radio Frequency Quadrupole (RFQ) accelerator directly coupled to two Drift Tube LINACs (DTL), which accelerate protons to their final energy of 13 MeV. Proton acceleration is facilitated by three Litton 5773 klystron

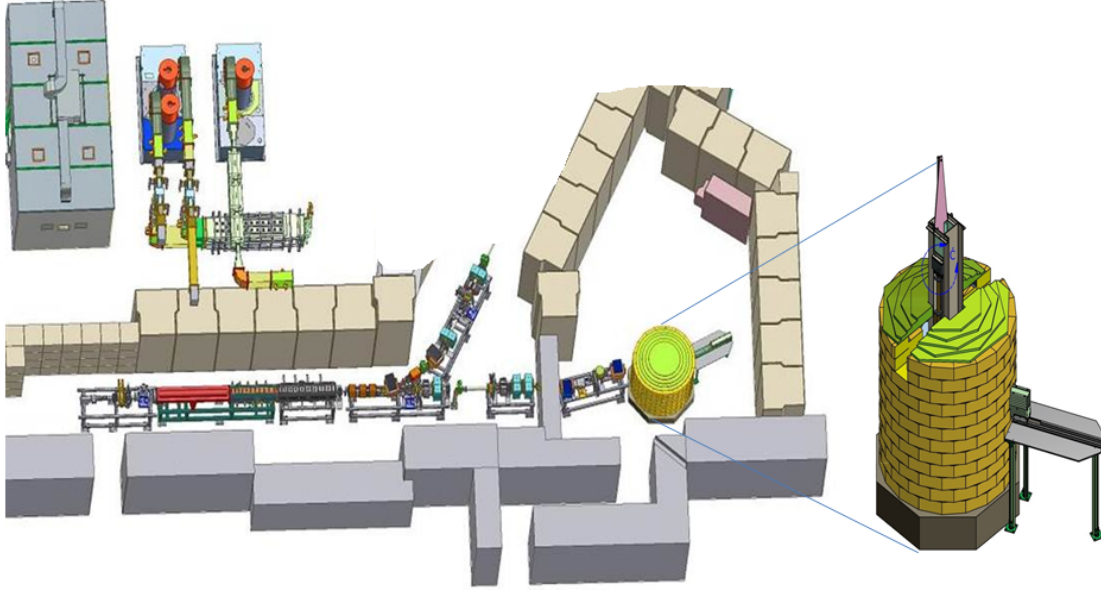


Figure 14. A schematic of the IU NREF beamline at the LENS.

RF tubes that provide 425 MHz microwave power to the RFQ and DTL components. Power delivered to the LINAC is approximately 1 MW with a 0.9% duty factor [45]. The duty factor is a measure of the time a pulsed beam is running. In essence, the duty factor can be described by $DF = \frac{PW}{t_{cycle}}$ where PW is the pulse width and t_{cycle} is the total time for one pulse cycle, which includes one proton pulse and one recovery period, and is defined as $t_{cycle} = f^{-1}$ where f is the accelerator frequency. The typical beam operating frequency is 20 Hz, making $t_{cycle} = 50$ ms.

After acceleration, the protons are focused using octupole magnets and directed down one of two beam lines using a selector magnet. The existence of two beam lines gives the facility increased flexibility in experiment set-up and operation. The first beam line is called the Low-Energy Neutron Source (LENS) beam line, while the second is called the Neutron Radiation Effects Program (NREP) beam line. Neutron production at the LENS target has been analyzed extensively [46], however the moderator configuration makes the LENS target impractical for use in radiation effects studies.

The NREP beam line terminates on a Target-Moderator-Reflector (TMR) stack, which contains a beryllium target assembly, space for a moderator containment vessel, and external shielding. The shielding primarily consists of borated polyethylene bricks to absorb neutrons and lead to absorb gamma radiation, with the goal of limiting radiation exposure outside the TMR.

Spectral Collapsing.

Since facilities produce neutrons in various ways, every facility is unique in its own neutron flux spectral shape. In order to compare results of experiments between facilities, a concerted effort was made to determine a standard method to collapse any spectral shape into an equivalent number of monoenergetic neutrons by means of a displacement damage kerma. Messenger [47] was the first to suggest a curve fit for experimental data from Smits and Stein [48]. The equation was

$$D(E) = AE \left[1 - e^{-B/E} \right], \quad (7)$$

where $D(E)$ is the lifetime damage constant, while A and B were fitting coefficients. From there, multiple researchers [49–53] have refined the curve.

Currently, the American Society for Testing and Materials (ASTM) publishes most of the community-developed standards for radiation effects testing, to include the standard by which a neutron spectrum can be collapsed. The standard number is E722-09e1, and the description is *Standard Practice for Characterizing Neutron Fluence Spectra in Terms of an Equivalent Monoenergetic Neutron Fluence for Radiation-Hardness Testing of Electronics*. It uses the damage kerma folded into the incident spectrum to determine equivalence.

The equivalent monoenergetic fluence, $\Phi_{eq,E_{ref},mat}$ is calculated as in Equation Set 8.

$$\Phi_{eq,E_{ref},mat} = \frac{\int_0^{\infty} \Phi(E) F_{D,mat}(E) dE}{F_{D,E_{ref},mat}} \quad (8)$$

$\Phi(E)$ = incident neutron spectrum, energy dependent

$F_{D,mat}(E)$ = displacement damage function for material
being irradiated, also energy dependent

$F_{D,E_{ref},mat}$ = reference value of damage function for
equivalent energy, E_{ref}

The radiation effects community typically uses 1 MeV as the reference standard, and the accepted reference value of the damage function at this energy is 95 MeV·mb. Therefore, the 1-MeV Equivalent (Si) neutron flux can be calculated as

$$\Phi_{eq,1-MeV,Si} = \frac{\int_0^{\infty} \Phi(E) F_{D,Si}(E) dE}{95[MeV \cdot mb]} \quad (9)$$

Additionally, the neutron energy spectrum hardness parameter for the irradiated material, H_{mat} , is defined as the ratio of the equivalent monoenergetic neutron fluence to the true total fluence [54], or

$$H_{mat} = \frac{\Phi_{eq,E_{ref},mat}}{\int_0^{\infty} \Phi(E) dE}. \quad (10)$$

This equivalence principle will be investigated during this research, and the results will be presented later in this document.

References

1. C. Kittel, *Introduction to Solid State Physics*, 8th ed. Wiley, 2004.
2. S. Sze and K. Ng, *Physics of Semiconductor Devices*. John Wiley & Sons, Inc., 2006.
3. S. Sze, *Semiconductor Devices: Physics and Technology*, 2nd ed. John Wiley & Sons, Inc., 2002.
4. W. Shockley, “The theory of *pn* junctions in semiconductors and *pn* junction transistors,” *Bell Syst. Tech. J.*, vol. 28, no. 3, pp. 435–489, 1949.
5. C. Goben, “Neutron bombardment reduction of transistor current gain,” Sandia Laboratory, Albuquerque, NM, Publication SCR-64-1373, 1964.
6. C. Goben and F. Smits, “Anomalous base current component in neutron irradiated transistors,” in *Presented at 1964 IEEE Nuclear and Space Radiation Effects Conference*, 1964.
7. C. Goben, “A study of the neutron-induced base current component in silicon transistors,” *IEEE Trans. Nucl. Sci.*, vol. 12, no. 5, pp. 134–146, 1965.
8. L. Su, G. Gassner, and C. goben, “Radiation and annealing characteristics of neutron bombarded silicon transistors,” *IEEE Trans. Nucl. Sci.*, vol. 15, no. 6, pp. 95–107, 1968.
9. R. Pierret, *Semiconductor device fundamentals*. Addison Wesley Longman, 1996.
10. T. Nagase, T. Sanda, A. Nino, W. Qin, H. Yasuda, H. Mori, Y. Umakoshi, and J. Szpunar, “MeV electron irradiation induced crystallization in metallic glasses: Atomic structure, crystallization mechanism and stability of an amorphous phase under the irradiation,” *Journal of Non-Crystalline Solids*, vol. 358, no. 3, pp. 502–518, February 2012.
11. Y. Shi, D. Shen, F. Wu, M. Deng, and K. Cheng, “On the formation of defect clusters in neutron-irradiated Si,” *Appl. Phys. A*, vol. 50, pp. 305–309, 1990.
12. M. Asom, J. Benton, R. Sauer, and L. Kimerling, “Interstitial defect reactions in silicon,” *Appl. Phys. Lett.*, vol. 51, pp. 256–258, 1987.
13. J. Srour, C. Marshall, and P. Marshall, “Review of displacement damage effects in silicon devices,” *IEEE Trans. Nucl. Sci.*, vol. NS-50, no. 3, pp. 653–670, 2003.
14. S. Myers, P. Cooper, and W. Wampler, “Model of defect reactions and the influence of clustering in pulse-neutron-irradiated Si,” *J. Appl. Phys.*, vol. 104, pp. 044507–1 – 044507–13, 2008.

15. Y. Shi, D. X. Shen, I. Wu, and K. J. Cheng, “A numerical study of cluster center formation in neutron irradiated silicon,” *J. Appl. Phys.*, vol. 67, no. 2, pp. 1116–1118, 1990. [Online]. Available: <http://scitation.aip.org/content/aip/journal/jap/67/2/10.1063/1.345799>
16. O. Holland, C. White, M. El-Ghor, and J. Budai, “MeV self-ion implantation in Si at liquid-nitrogen temperature – A study of damage morphology and its anomalous annealing behavioral,” *J. Appl. Phys.*, vol. 68, no. 5, pp. 2081–2086, 1990.
17. S. Campisano, S. Coffa, V. Raineri, P. F., and E. Rimini, “Mechanisms of amorphization in ion implanted crystalline silicon,” *Nucl. Instr. Meth. Phys. Res. B*, vol. 80-81, pp. 514–518, 1993.
18. I. Jencic and I. Robertson, “Regrowth of heavy-ion implantation damage by electron beams,” *Mater. Sci. Semicond. Process.*, vol. 3, pp. 311–315, 2000.
19. S. Donnelly, R. Birtcher, V. Vishnyakov, and G. Carter, “Annealing of isolated amorphous zones in silicon,” *Appl. Phys. Lett.*, vol. 82, no. 12, pp. 1860–1862, 2003.
20. M. Alurralde, F. Paschoud, M. Victoria, and D. Gavillet, “The displacement damage produced in Si by 590 MeV protons,” *Nucl. Instr. Meth. Phys. Res. B*, vol. 80-81, pp. 523–527, 1993.
21. J. Yamasaki, S. Takeda, and K. Tsuda, “Elemental process of amorphization induced by electron irradiation in Si,” *Phys. Rev. B*, vol. 65, pp. 115213–1–115213–10, 2002.
22. B. MacEvoy, G. Hall, and K. Gill, “Defect evolution in irradiated silicon detector material,” *Nucl. Instr. Meth. Phys. Res. A*, vol. 374, no. 1, pp. 12–26, 1996.
23. V. van Lint, “The physics of radiation damage in particle detectors,” *Nucl. Instr. Meth. Phys. Res. A*, vol. 253, no. 3, pp. 453–459, 1987.
24. V. van Lint, T. Flanagan, R. Leadon, J. Naber, and V. Rogers, *Mechanisms of radiation effects in electronic materials*. John Wiley & Sons, Inc., 1980, vol. 1, ch. 7.
25. B. Gossick, “Disordered regions in semiconductors bombarded by fast neutrons,” *J. Appl. Phys.*, vol. 30, pp. 1214–1218, 1959.
26. M. Bertolotti, “Experimental observations of damage clusters in semiconductors,” *Proc. Santa Fe Conf. Rad. Eff. in Semiconductors*, pp. 311–329, 1968.
27. S. Wood, N. Doyle, J. Spitznagel, W. Choyke, R. More, J. McGruer, and R. Irwin, “Simulation of radiation damage in solids,” *IEEE Trans. Nucl. Sci.*, vol. 28, no. 6, pp. 4107–4112, 1981.

28. M. Kuhnke, E. Fretwurst, and G. Lindstroem, “Defect generation in crystalline silicon irradiated with high energy particles,” *Nucl. Instr. Meth. Phys. Res. B*, vol. 186, pp. 144–151, 2002.
29. H. Sander, “Room temperature annealing of silicon transistor parameters degraded by a burst of neutrons,” Sandia Corporation, Tech. Rep. SC-R-64-192, July 1964.
30. H. Sander and B. Gregory, “Transient annealing in semiconductor devices following pulsed neutron irradiation,” *IEEE Trans. Nucl. Sci.*, vol. 13, no. 6, pp. 53–62, December 1966.
31. ——, “Circuit application of transistor annealing,” Sandia Laboratory, Tech. Rep. SC-R-72-2703, September 1971.
32. B. Gregory and H. Sander, “Transient annealing of defects in irradiated silicon devices,” in *Proceedings of the IEEE*, vol. 58, no. 9, 1970, pp. 1328–1341.
33. D. Binder, D. Butcher, J. Crepps, and E. Hammer, “Rapid annealing in silicon semiconductor devices,” Air Force Weapons Laboratory, Tech. Rep. AFWL-TR-69-3, September 1969.
34. L. Cheng and J. Lori, “Characteristics of neutron damage in silicon,” *Phys. Rev.*, vol. 171, p. 856, 1968.
35. L. McMurray and G. Messenger, “Rapid annealing factor for bipolar silicon devices irradiated by fast neutron pulse,” *IEEE Trans. Nucl. Sci.*, vol. 28, no. 6, pp. 4392–4396, Dec 1981.
36. F. McLean and T. Oldham, “Basic mechanisms of radiation effects in electronic materials and devices,” Harry Diamond Laboratories, Tech. Rep. HDL-TR-2129, 1987.
37. C. Mallon and J. Harrity, “Short-term annealing in transistors irradiated in the biased-off mode,” *IEEE Trans. Nucl. Sci.*, vol. 17, no. 6, pp. 45–49, 1970.
38. J. Srour and O. Curtis, “Short-term annealing in silicon devices following pulsed 14-MeV neutron irradiation,” *IEEE Trans. Nucl. Sci.*, vol. 19, no. 6, pp. 362–370, 1972.
39. T. Wrobel and D. Evans, “Rapid annealing in advanced bipolar microcircuits,” *IEEE Trans. Nucl. Sci.*, vol. 29, no. 6, pp. 1721–1726, Dec 1982.
40. J. Heirtzler, “The future of the south atlantic anomaly and implications for radiation damage in space,” *J. Atmos. Sol-Terr. Phys.*, vol. 64, no. 16, pp. 1701–1708, 2002. [Online]. Available: <http://www.sciencedirect.com/science/article/pii/S1364682602001207>

41. C. Foster, M. Krzesniak, V. McAtee, B. Hamilton, M. Ball, J. Titus, B. von Przewoski, T. Turflinger, E. Hall, G. East, D. Friesel, W. Sloan, T. Rinckel, K. Murray, M. Savage, Y. Kim, and J. Ramsey, “Exploration of the IUCF 220-MeV proton synchrotron as a flash proton source,” *J. Rad. Eff.*, vol. 18, 2000.
42. (2014, February) Research reactor — nuclear reactor lab. The Ohio State University Research Reactor. [Online]. Available: <http://reactor.osu.edu/facilities/research-reactor>
43. “Personal correspondance with Dr. Susan White at the OSURR,” March 2014.
44. M. Halstead, “Characterization of the energy spectrum at the Indiana University NREP neutron source,” Master’s thesis, Air Force Institute of Technology, March 2011.
45. A. Bogdanov, V. Anferov, M. Ball, D. Baxter, V. Derenchuk, A. Klyachko, T. Rinckel, P. Sokol, and K. Solberg, “Upgrade of the LENS proton LINAC: Commissioning and results,” in *Proceedings of PAC07*, 2007.
46. C. Lavelle, “The neutronic design and performance of the Indiana University Cyclotron Facility (IUCF) Low Energy Neutron Source,” Ph.D. dissertation, Indiana University, 2007.
47. G. Messenger, “Displacement damage in silicon and germanium transistors,” *IEEE Trans. Nucl. Sci.*, vol. 12, no. 2, pp. 53–74, 1965.
48. F. Smits and H. Stein, “Energy dependence of neutron damage in silicon,” *Bull. Am. Phys. Soc.*, vol. 9, p. 289, 1964.
49. E. Smith, D. Binder, P. Compton, and R. Wilbur, “Theoretical and experimental determinations of neutron energy deposition in silicon,” *IEEE Trans. Nucl. Sci.*, vol. 13, no. 6, pp. 11–17, 1966.
50. F. Wikner, D. Nichols, J. Nabor, T. Flanagan, H. Horiye, and V. van Lint, “Transient radiation effects final report,” NASA, Tech. Rep. DA-49-186-AMC-65(x)-1, 1967.
51. H. J. Stein, “Energy dependence of neutron damage in silicon,” *J. Appl. Phys.*, vol. 38, no. 1, pp. 204–210, 1967. [Online]. Available: <http://scitation.aip.org/content/aip/journal/jap/38/1/10.1063/1.1708956>
52. J. Wicklund, “Neutron fluence and damage in silicon for free air over an earth surface,” Harry Diamond Laboratories, Tech. Rep. HDL-TR-1494, 1970.
53. R. Holmes, “Carrier removal in neutron irradiated silicon,” *IEEE Trans. Nucl. Sci.*, vol. 17, no. 6, pp. 137–143, 1970.

54. ASTM Standard E722-09(e1), *Standard Practice for Characterizing Neutron Energy Fluence Spectra in Terms of an Equivalent Monoenergetic Neutron Fluence for Radiation-Hardness Testing of Electronics*, ASTM International, West Conshohocken, PA, 2009.

III. First-Principles Modeling of BJT Performance

In order to evaluate the relationship between short-pulse irradiation and model BJT gain degradation, a physics-based model with time-dependent formation and annealing was developed. In this section, the models used to describe gain degradation in BJT devices will be presented, the basics of a first-principles model will be developed, and preliminary validation and verification will be described.

3.1 Historical Modeling Efforts

The Non-Ionizing Energy Loss (NIEL), is a figure of merit that describes the damage potential for displacement by particle radiation in solids. NIEL can be correlated between particles (protons, neutrons, etc.) at any energy via

$$NIEL = \frac{N_{Av}}{A} (\sigma_e T_e + \sigma_i T_i), \quad (11)$$

where N_{Av} is Avagadro's number and A is the atomic weight. In Equation 11, σ is the cross section while T_i and T_e are the effective average recoil energies (corrected for ionization loss) for elastic, e , and inelastic, i , scatterings.

One of the main motives for use of NIEL in radiation effects experiments, as Srour et al. state [1], is “that the significant nuclear weapons effects database could be mined to predict a device response”. The copious experiments of the nuclear test era provided a treasure trove of data from measurements taken across a broad range of nuclear weapon types and yields. The various radiation environments explored allowed researchers to empirically correlate device responses and test their theories scaled down in the lab.

In these experiments, Equation 11 and the Messenger-Spratt Equation [2] were applied to bipolar technology since current gain scaled linearly with fluence. The

Messenger-Spratt Equation describes semiconductor material parameter response to incoming radiation. In this case, it was found that device current gain after irradiation, β_f , can be modeled as

$$\frac{1}{\beta_f} = \frac{1}{\beta_o} + K(E)\Phi(E) \quad (12)$$

where β_o is the initial device gain before irradiation, $K(E)$ is the particle- and energy-dependent damage factor, and $\Phi(E)$ is the incident particle fluence in n/cm^2 .

The Messenger-Spratt equation was proven by Messenger [3] in 1973 by using a series expansion of the base transport factor, α_T , per the work done by Gover [4]. The expansion is

$$\alpha_T = 1 - U_1 \frac{W^2}{L^2} + U_2 \frac{W^4}{L^4} - \dots \quad (13)$$

where W is the depletion width, $L = \sqrt{D\tau}$ is the diffusion length, and U is a coefficient determined by successive iteration of the equations for excess minority carrier concentration in the base and the minority current density (please see ?? for more detail). For the diffusion length, D is the diffusion constant and τ is the minority carrier lifetime. Messenger made the assumption that, since this series is rapidly convergent, it can be truncated after the U_1 term. Thus, from Equation 13 and a further assumption that base transport is the dominant factor in gain degradation,

$$\frac{1}{\beta} = \frac{U_1 W^2}{D\tau}. \quad (14)$$

Gover also showed that, if n/τ is described by a single time constant, $\omega = \frac{D}{U_1 W^2}$, where ω is 2π times the common emitter gain bandwidth product. From Messenger and Spratt's original discussion of carrier lifetime degradation,

$$\frac{1}{\tau} = \frac{1}{\tau_i} + \frac{\Phi}{K}. \quad (15)$$

where K is the carrier lifetime degradation coefficient. If Equations 14 and 15 are combined with the description of ω , the Messenger-Spratt equation is

$$\frac{1}{\beta_f} = \frac{1}{\beta_o} + \frac{\Phi}{\omega K} \quad (16)$$

which matches with Equation 12 if it is noted that the damage constant, $K(E)$, and $(\omega K)^{-1}$ are interchangeable since K is just a coefficient.

There have been numerous studies done over the intervening years that use Equation 12 to predict BJT performance. From the early years of Frank et al. [5] and Ramsey et al. [6] to the more recent Williams [7], Bielejec [8], Li [9], and Consolandi [10], the model of damage response in a silicon BJT has remained relatively unchanged. It is an adequate measure of BJT gain degradation in certain situations. However, it is extremely important to realize that there are numerous assumptions that are made.

The Messenger-Spratt equation assumes that the final gain, β_f is measured a long time after irradiation. In essence, the damage constant K only deals with the permanent defects left in the device after the short-term defects have annealed away.

The most important assumption used in the Messenger-Spratt equation is the lack of consideration of time. Since its development in the 1950's, the Messenger-Spratt equation has been based on the assumption that irradiation times for displacement damage experiments are very short.

The SPR-III was an often used and well-characterized irradiation facility, and it had two modes of operation: the more commonly used pulse mode and the less commonly used steady state mode. The steady state mode was less commonly used because it induced a large build-up of fission fragment inventory in the core [11]. For pulsed operation, bare uranium metal plates were brought together and the heat of fission caused the plates to expand far enough apart that it shut down the reaction in less than 1 ms. Neutron fluences, in terms of 1-MeV equivalent (Si) neutrons, in

the “glory hole” of the core were originally on the order of $10^{14} \frac{n}{cm^2 \cdot pulse}$. Through a number of upgrades and modifications to the system, the pulse width increased from 50 μs for SPR-II [12], to approximately 100 μs for SPR-III [13].

The emphasis on using a pulsed neutron source is that, if neutrons interact over short time intervals, the defects created in the silicon bulk in BJT devices do not have time to migrate and form additional complexes before the pulse is complete. Most of the point defects, vacancies and interstitials, have recombined in the first 10 ns [14]; however, short term migration and rearrangement of the permanent defects can take 10^{-2} to 10^3 s.

Another point to note about the application of the Messenger-Spratt equation is that it contains theory that is based solely on experimental evidence. Short pulse, low-flux experiments would underestimate the combined effects of co-located damage sites and long interaction times would overestimate. The expression was developed by assuming Shockley-Read-Hall recombination [15], while the defects introduced by irradiation were considered as recombination centers. At no point is time or defect density considered, thus it is intrinsically time-independent. It is an adequate description for most of the analysis accomplished over the last 60 years because it was used on single-pulse neutron irradiation facilities and reactors.

3.2 Model Development Progression

A mathematical model was sought that would predict the degradation of BJT performance parameters with neutron irradiation. This model had a number of steps in its progression, which will now be described in greater detail.

Step One – General Defect Mode.

The Messenger-Spratt relationship for gain is given in Equation 12. Equation 12 could be rewritten as

$$\sum_{i=1}^n K_{d,i} N_{d,i} = \frac{1}{\beta_f} - \frac{1}{\beta_o}, \quad (17)$$

where $K_{d,i}$ and $N_{d,i}$ are the i^{th} damage constant and defect population. That is to say that the damage in the device is directly proportional to the defect species concentration. This means that the best way to predict the gain response as a function of a time-dependent flux of neutrons such as the one found at the IU NREF is to properly model the defects as they are created and anneal. As a first order approach, a Bateman-like [16] equation can be developed that describes the time rate of change of the number of defects in the device, N_d , as

$$\frac{dN_d}{dt} = \text{Created} - \text{Destroyed} = \sigma_d \phi - \frac{1}{\tau_d} N_d, \quad (18)$$

where σ_d is the cross section for formation of a defect, ϕ is the defect-forming particle flux, and τ_d is the defect lifetime. This is a relatively simple first-order, linear, ordinary differential equation that has an exact solution, which is

$$N_d(t) = \sigma_d \Phi(t) \tau_d - \xi e^{-t/\tau_d}, \quad (19)$$

where ξ is the constant of integration. If the initial population is $N_d = 0$, then Equation 19 becomes,

$$N_d(t) = \sigma_d \Phi(t) \tau_d (1 - e^{-t/\tau_d}). \quad (20)$$

A plot of this result is displayed in Figure 15. As is expected, Equation 20 depicts growth in the population of defects that approaches an asymptote at $\sigma_d \phi \tau_d$ with a characteristic time constant. However, if the flux were turned off (*i.e.* $\phi \rightarrow 0$), the

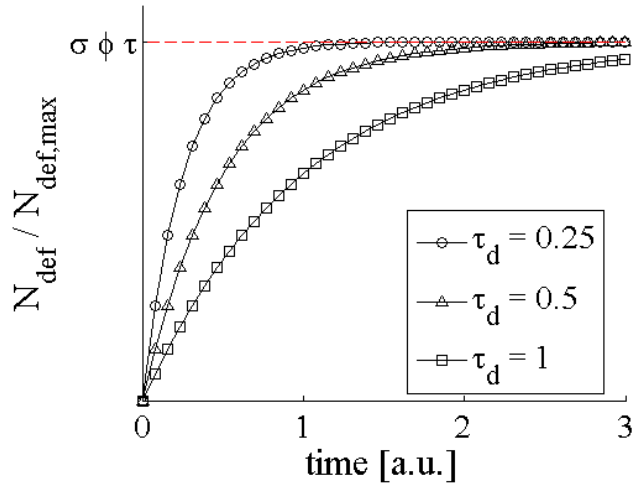


Figure 15. Using a single defect species results in the growth of the defect population that approaches an asymptote with a time constant characteristic of the relaxation of defect species during irradiation.

model predicts an exponential drop in the defect population to 0. From literature, this cannot be the case as some displacement damage is residual in the material. Therefore, the model must be developed further, and the next step is to include multiple defect species interactions.

Step Two – Model Including Multiple Defect Species.

If this concept is extended to two defect types, vacancies and di-vacancies, the physical description becomes more complicated. Both defects have a finite probability, σ_v and σ_{vv} , of being created via the neutron flux. Additionally, both defect species may anneal back to a “perfect” crystal lattice with some lifetime, τ_v and τ_{vv} . However, there is also a chance that a vacancy can become a di-vacancy by capturing another vacancy. Additionally, there is the chance that a di-vacancy can become a single vacancy by splitting or having one vacancy recombine. This description can be translated into two differential equations as Equation Set 21.

$$\begin{aligned}\frac{dN_v}{dt} &= \sigma_v \phi - N_v \left(\frac{1}{\tau_v} + \frac{1}{\tau_{v \rightarrow vv}} \right) + N_{vv} \left(\frac{1}{\tau_{vv}} + \frac{1}{\tau_{vv \rightarrow v}} \right) \\ \frac{dN_{vv}}{dt} &= \sigma_{vv} \phi - N_{vv} \left(\frac{1}{\tau_{vv}} + \frac{1}{\tau_{vv \rightarrow v}} \right) + N_v \left(\frac{1}{\tau_v} + \frac{1}{\tau_{v \rightarrow vv}} \right)\end{aligned}\quad (21)$$

In Equation Set 21, ϕ is the flux of incident damaging particles and $\tau_{v \rightarrow vv}$ and $\tau_{vv \rightarrow v}$ are the lifetimes of a vacancy capturing another vacancy to become a di-vacancy and of a di-vacancy splitting into two vacancies, respectively.

As this step of the process is still hypothetical, arbitrary values for lifetime and cross section were selected to illustrate the model behavior. Figure 16 displays an example of the two defect model showing how the vacancy population rises quicker than the di-vacancy population, but it reaches an equilibrium faster due to its shorter lifetime. In this example, the parameter values were set as shown below:

$$\tau_v = \tau_{vv} = \tau_{vv \rightarrow v} = 0.05s,$$

$$\tau_{v \rightarrow vv} = 0.5s,$$

$$\phi = 100 \text{ cm}^{-2} \text{ s}^{-1},$$

$$\sigma_v = 0.1 \text{ cm}^2,$$

$$\sigma_{vv} = 0.01 \text{ cm}^2.$$

This system of equations can be solved analytically; and, using the parameters selected above, the resultant time-dependent equations are described as Equation Set 22.

$$\begin{aligned}N_v(t) &= 0.56 + 0.12e^{-\frac{79}{3}t} - 0.68e^{-\frac{41}{3}t} \\ N_{vv}(t) &= 0.61 + 0.58e^{-\frac{79}{3}t} - 1.19e^{-\frac{41}{3}t}\end{aligned}\quad (22)$$

These first steps in the model development were purely hypothetical, as it is known that displacement damage in semiconductors cannot be lumped into one or two categories of defects. Even a model using two species does not incorporate the

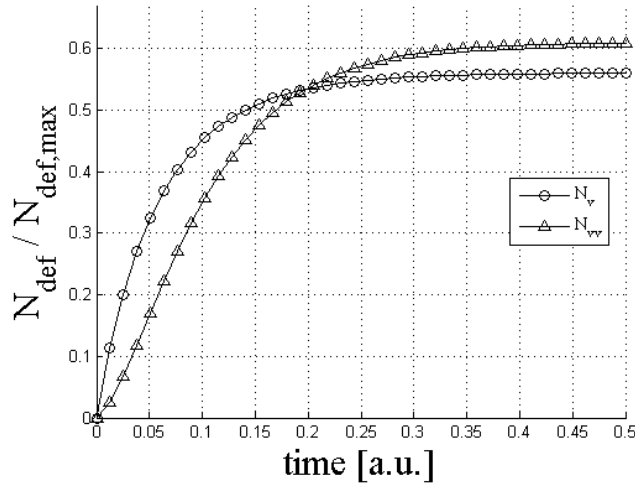


Figure 16. For this arbitrary selection of parameters, the vacancy population rises quickly, but reaches a secular equilibrium at a lower level than the di-vacancies during irradiation.

complexity necessary to account for many of the behaviors of device performance under irradiation.

Step Three – Incorporation of Precursors.

Next, the model was further developed to include precursors. In any crystalline matrix, there are imperfections and bonding sites where a silicon atom or atoms are still a part of the lattice structure but are not properly aligned. This can essentially be accounted for by considering these sites as a separate species with a cross section for conversion into vacancy or divacancy, $\sigma_{Si' \rightarrow v}$ and $\sigma_{Si' \rightarrow vv}$ respectively. However, if it is assumed that these precursors cannot be regenerated, then it is represented by an extension of Equation 21 as

$$\begin{cases} \frac{dN_v}{dt} = \sigma_v \phi - \frac{N_v}{\tau_v} + \frac{N_{vv}}{\tau_{v \rightarrow vv}}, \\ \frac{dN_{vv}}{dt} = \sigma_{vv} \phi - \frac{N_{vv}}{\tau_{vv}} + \frac{N_v}{\tau_{vv \rightarrow v}}, \\ \frac{dN_{Si'}}{dt} = -N_{Si'} \sigma_{Si' \rightarrow v} \phi(t) - N_{Si'} \sigma_{Si' \rightarrow vv} \phi(t) + c_o, \end{cases} \quad (23)$$

where c_o is a generation mechanism for the silicon precursors. Equation Set 23 can be rearranged to solve for each of the three species and collected into a vector equation as in Equation Set 24.

$$\vec{N}'(t) = \mathbf{A}\vec{N}(t) + \vec{b}$$

$$N'(t) = \begin{pmatrix} N'_v \\ N'_{vv} \\ N'_{Si'} \end{pmatrix}, \vec{N}(t) = \begin{pmatrix} N_v \\ N_{vv} \\ N_{Si'} \end{pmatrix},$$

$$\mathbf{A} = \begin{pmatrix} a_1 & a_2 & \phi\sigma_{Si' \rightarrow v} \\ a_2 & a_1 & \phi\sigma_{Si' \rightarrow vv} \\ 0 & 0 & -\phi(\sigma_{Si' \rightarrow v}\sigma_{Si' \rightarrow vv}) \end{pmatrix} \quad (24)$$

$$\vec{b}(t) = \begin{pmatrix} \sigma_v\phi \\ \sigma_{vv}\phi \\ c_o \end{pmatrix}$$

In Equation Set 24, $a_1 = \tau_v^{-1} + \tau_{v \rightarrow vv}^{-1}$ and $a_2 = \tau_v^{-1} + \tau_{vv \rightarrow v}^{-1}$. The general solution to Equation Set 24 is,

$$\vec{N}(t) = k_1 e^{\lambda_1 t} \vec{\xi}_1 + k_2 e^{\lambda_2 t} \vec{\xi}_2 + k_3 e^{\lambda_3 t} \vec{\xi}_3. \quad (25)$$

In Equation 25, λ_1 , λ_2 , and λ_3 are the eigenvalues found by $\det(\mathbf{A} - \lambda\mathbf{I}) = 0$; k_1 , k_2 , and k_3 are constants, and $\vec{\xi}_1$, $\vec{\xi}_2$, and $\vec{\xi}_3$ are eigenvectors corresponding to the eigenvalues. These constants are determined using the initial conditions, which are

$$N_v(0) = N_{v,o}, N_{vv}(0) = N_{vv,o}, \text{ and } N_{Si'}(0) = N_{Si',o}.$$

Equation 25 can be solved for three eigenvalues using the solution for the roots of a cubic equation. This indicates that the analytic solution of a model containing just

three defect species was much more complicated than the two-defect model. At this point, analytic solutions were abandoned in favor of numerical solution methods such as Runge-Kutta Ordinary Differential Equation (ODE) solvers implemented using the Matlab [17] mathematical software package.

Step Four – Incorporating Concentrations, C_{def} .

In order to better incorporate experimental results into the model, the equations were converted to concentration variables, denoted with square brackets, $[]$, instead of absolute population variables. This approach is described in the following subsections.

Change to Concentration Variables.

The following was done after considering the work of Verner, Gerasimenko, and Corbett [18] in which they consider the reaction kinetics of defects in semiconductor processing. Thus, there are formation and dissociation reactions, driven by capture and dissociation rates. For example, a vacancy combining with another vacancy to form a divacancy can be written as,



The capture rate, α_{cap} , and dissociation rate, α_{diss} , are given by

$$\begin{aligned} \alpha_{cap} &= 4\pi D_v r_{cap}, \\ \alpha_{diss} &= \nu_{diss} \exp \left\{ -E_{diss} / (k_B T) \right\}, \end{aligned} \quad (27)$$

D_v is the diffusion coefficient for vacancies (and the assumption is made that the diffusion rate of a higher order vacancy complex is very small in comparison, to make it negligible and set equal to 0), r_{cap} is the capture radius of one species by another,

ν_{diss} is the vibrational frequency of dissociation for a particular species, E_{diss} , is the energy associated with that dissociation, k_B is Boltmann's constant, and T is the temperature.

Additionally, annihilation occurs when a vacancy [V] combines with an interstitial [I] as $[V] + [I] \rightarrow Lattice$. In this case, the annihilation rate coefficient would be $\alpha_{ann} = 4\pi (D_v + D_i) r_{cap,V+I}$. Since the interstitial and vacancy are capable of diffusing with comparable speeds throughout the semiconductor, both diffusivities should be considered in creating the rate coefficient of annihilation. This may not be the case for point defects interacting with larger clusters or large impurity atoms whose diffusivities are much smaller and, thus, negligible in comparison with those of the point defects.

Impurity interactions also occur. For example, a vacancy may interact with an impurity, [X], and this can be denoted as $[V] + [X] \longleftrightarrow [V \cdot X]$ with relevant capture and dissociation coefficients. The impurity is often considered "stationary" in regards to the vacancy, so it has no diffusion coefficient. The same development can be applied to all possible defect species, so the problem has a large number of unknowns and equations. Therefore, the problem must be focused on those that affect the device operation in order for the solution to be tractable.

For this research, many combinations of defect species were considered. Initially, the list of species was limited to vacancies, divacancies, interstitials, vacancy-impurity complexes, divacancy-impurity complexes, and impurities. There are nine interactions that account for creation or destruction of these six species. They are tabulated in Table 3.

Table 3. Description of nine interactions used for six defect species model.

Formula	Creation	Annealing
$G_v \rightarrow [V]$	Generation of Vacancies	N/A
$G_i \rightarrow [I]$	Generation of Interstitials	N/A
$[V] + [V] \xrightleftharpoons[\alpha_2]{\alpha_1} [VV]$	Capture of vacancy by another vacancy to become divacancy	Dissociation of divacancy into two vacancies
$[V] + [I] \xrightarrow{\alpha_3} \text{Lattice}$	N/A	Annihilation of vacancy with interstitial to become lattice
$[V] + [X] \xrightleftharpoons[\alpha_5]{\alpha_4} [VX]$	Capture of vacancy by impurity	Dissociation of vacancy-impurity complex
$[V] + [VX] \xrightleftharpoons[\alpha_7]{\alpha_6} [VVX]$	Capture of vacancy by vacancy-impurity complex	Dissociation of divacancy-impurity complex
$[I] + [VX] \xrightarrow{\alpha_8} [X]$	Capture of interstitial by vacancy-impurity complex	N/A
$[I] + [VVX] \xrightarrow{\alpha_9} [VX]$	Capture of interstitial by divacancy-impurity complex	N/A
$[VV] + [X] \xrightleftharpoons[\alpha_{11}]{\alpha_{10}} [VVX]$	Capture of divacancy by impurity	Dissociation of divacancy-impurity complex

Each of these interactions can be converted into differential equations and collected into a system of six ODEs. As an example, $[V] + [V] \xrightleftharpoons[\alpha_2]{\alpha_1} [VV]$ models a reaction going to the right as a *destruction* of 2 vacancies. Therefore, they can be written as

$$\frac{dC_v}{dt} = -2\alpha_1 C_v C_v. \quad (28)$$

This reaction also models the *creation* of one divacancy, so,

$$\frac{dC_{vv}}{dt} = 2\alpha_1 C_v C_v. \quad (29)$$

After considering each reaction and reversibility/irreversibility of the reaction, the system of differential equations becomes:

$$\begin{aligned} \frac{dC_v}{dt} &= G_v - 2\alpha_1 C_v C_v + 2\alpha_2 C_{vv} - \alpha_3 C_v C_i - \alpha_4 C_v C_x + \alpha_5 C_{vx} - \alpha_6 C_v C_{vx}, \\ &\quad + \alpha_7 C_{vvx}, \\ \frac{dC_{vv}}{dt} &= \alpha_1 C_v C_v - \alpha_2 C_{vv} - \alpha_{11} C_{vv} C_x + \alpha_{10} C_{vvx}, \\ \frac{dC_i}{dt} &= G_i - \alpha_3 C_v C_i - \alpha_8 C_i C_{vx} - \alpha_9 C_i C_{vvx}, \\ \frac{dC_{vx}}{dt} &= \alpha_4 C_v C_x - \alpha_5 C_{vx} - \alpha_6 C_v C_{vx} + \alpha_7 C_{vvx} + \alpha_9 C_i C_{vvx}, \\ \frac{dC_{vvx}}{dt} &= \alpha_6 C_v C_{vx} - \alpha_7 C_{vvx} - \alpha_9 C_i C_{vvx} - \alpha_{10} C_{vvx} + \alpha_{11} C_{vv} C_x, \\ \frac{dC_x}{dt} &= -\alpha_4 C_v C_x + \alpha_5 C_{vx} + \alpha_8 C_i C_{vx} - \alpha_{11} C_{vv} C_x + \alpha_{10} C_{vvx}. \end{aligned} \quad (30)$$

In this system of equations, the concentration notation, $[]$, was replaced with the letter C and a subscript. For example, the concentration of vacancies noted previously as $[V]$ was changed to C_v . Additionally, while impurities cannot be created, complexes that include clusters may dissociate into the constituent parts, leaving the impurity atoms behind. For the sake of the model, this is equivalent to “creating” them.

Generation Rate of Defects.

In the system of equations, G_v and G_i are the generation rates of the vacancies and interstitials, respectively. These are functions of the neutron flux and lattice properties. The model provides a method for generation of Frenkel pairs by incorporating the displacement damage kerma along with the expected neutron flux spectrum. The displacement damage kerma in silicon is tabulated in ASTM Standard E722-09, the *Standard Practice for Characterizing Neutron Energy Fluence Spectra in Terms of an Equivalent Monoenergetic Neutron Fluence for Radiation-Hardness Testing of Electronics* [19], and is displayed in Figure 17. In this standard, the user is directed to ICRU reports 13 [20] for more information on the kerma.

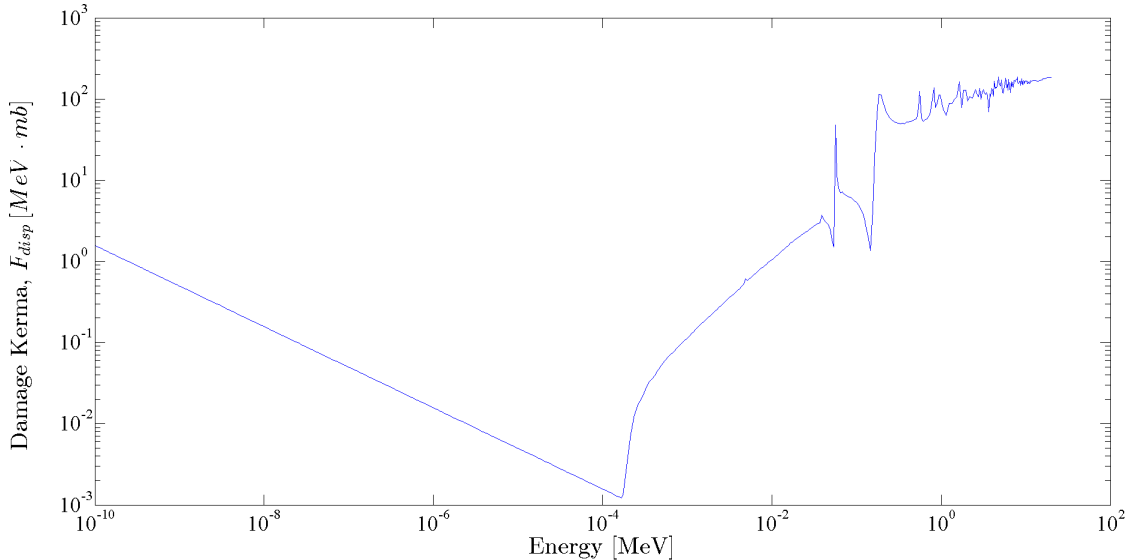


Figure 17. The displacement damage kerma for a silicon semiconductor as tabulated in the ASTM Standard E722 [19].

In the model developed in this research, it is assumed that Frenkel pairs can be created when the interacting particle deposits energy surpassing a threshold value, E_{fp} . Therefore, the generation rate of Frenkel pairs is defined as

$$G_v = G_i = \frac{\int \Phi(E)F(E)dE}{E_{fp}}, \quad (31)$$

where $F(E)$ is the displacement kerma for neutrons in silicon. This results in a constant generation rate in the bulk silicon that is directly dependent upon the flux.

Step Five – Development of Reaction Rate Parameters.

The system of non-linear differential equations developed in Section 3.2 can be solved if the reaction coefficients are known. Each reaction has a reaction rate coefficient that dictates the process progression and can be listed in two categories: *capture* and *dissociation* rates. Every α in Equation 30 designates a rate coefficient. Rates are most often empirically derived due to their many dependencies, most on material quality. Therefore, they have large uncertainties. In the following subsections, the diffusion coefficients of vacancies and interstitials, capture radii, and the dissociation frequency are investigated in more detail. These parameters fit into model as a part of many rate coefficients, α .

Vacancy and Interstitial Diffusion Coefficient.

As an example of the uncertainty in knowledge of the rate parameters, Wang et al. [21] stated that the diffusion coefficient of vacancies in Si at room temperature is between $3.4 \times 10^{-8} \text{ cm}^2/\text{s}$ and $14.0 \times 10^{-8} \text{ cm}^2/\text{s}$. However, in 1998, Hallén et al. [22] measured the vacancy diffusivity in Si at room temperature as $4.2 \times 10^{-9} \text{ cm}^2/\text{s}$. Voronkov and Falster [23] have measured a value at room temperature of $3.0 \times 10^{-10} \text{ cm}^2/\text{s}$ and indicate it has an Arrhenius behavior with a pre-factor of $2.3 \times 10^{-4} \text{ cm}^2/\text{s}$ and an associated energy barrier of 0.35 eV. This leads to a room temperature value of $1.85 \times 10^{-10} \text{ cm}^2/\text{s}$. In essence, there is no single definitive value for the diffusion coefficient of vacancies in silicon at room temperature.

The diffusion coefficient for interstitials is similar. Hallén et al. [22] measured a value of $3.2 \times 10^{-14} \text{ cm}^2/\text{s}$ at room temperature, whereas Libertino and Coffa [24, 25],

measured values of 1.5×10^{-15} cm²/s and 2.0×10^{-15} cm²/s. Consistent in the literature is that vacancies are substantially more mobile than interstitials.

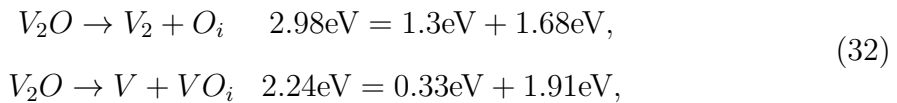
Capture Radii.

Less information exists regarding capture radii for the various species. Cowern et al. [26] report effective capture radii for boron interstitials and substitutionals on the order of 0.25-1 nm. This is reasonable, as the typical spacing between two silicon atoms is about 0.2 nm.

Dissociation Frequency.

The “vibrational frequency” of dissociation describes the rate at which larger defect species, such as the vacancy-impurity complex, obtain enough vibrational energy to break part into their constituent parts. In their seminal 1965 paper, Watkins and Corbett [27] state a value of approximately 10¹³ s⁻¹ for something they call the “frequency factor” for silicon defect dissociation. With this exception, there is no other information on the rate at which defect species may dissociate.

Furuhashi and Taniguchi [28] state that the activation energy of dissociation is defined as the sum of the binding energy of the complex with the smaller migration energies of the separated defects. Using values for a divacancy-oxygen complex, one gets



where O_i represents an oxygen interstitial. Both reactions in Equation Set 32 can occur, but the second is more likely because of its smaller activation energy. In this same paper, they provide barrier energies for multiple species as $E_b(Vacancy) = 0.33$ eV, $E_b(Divacancy) = 1.3$ eV, $E_b(VO) = 2.0$ eV, $E_b(O_i) = 2.53$ eV.

Step Six – Gain, β , Calculation.

From Section 2.1, device gain in a semiconductor is defined as in Equations 3 and 4. Each parameter in Equation 3 is device-dependent, in that they rely upon the characteristics of a particular device that has been fabricated; and defect-dependent, in that they rely on the amount and type of defects in the material.

Semiconductor Parameters.

Minority carrier concentrations are determined from basic principles. For doped, or extrinsic, semiconductor material, a region is *n*- or *p*-type material if the majority carrier is electrons or holes, respectively. This is done by adding electron donor or acceptor impurities. In an n^+pn BJT such as the 2n2222A, the base is *p*-type, while the emitter and collector are *n*-type. Physical characterization of the 2n2222A devices was not possible for this work. However, Keiter, Russo, and Hembree [13] used spreading resistance measurements as well as Secondary Ion Mass Spectroscopy (SIMS) to characterize the 2n2222A silicon BJTs that they were testing, and this profile is adopted as a “typical” device doping profile for the sake of analysis. A replotting of their data is displayed in Figure 18.

From a depth of 0-1.5 μm , the phosphorous donor impurity atoms dominate the boron acceptor impurity atoms, thus the region is *n*-type and represents the emitter region. On the other hand, from 1.5-3.0 μm , the opposite is true, making the region *p*-type and the base. Since both impurity types are present in each region, it is compensation doped, meaning some impurity sites are canceled out by those of the opposite type. Assuming full ionization of donors and acceptors, the majority and minority carrier concentrations in the base are

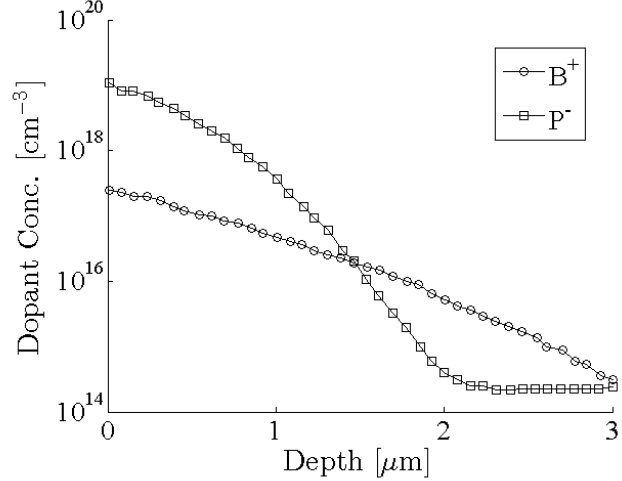


Figure 18. The dopant concentrations (B^+ and P^-) in the base-emitter region of a 2n2222A silicon BJT were determined from spreading resistance measurements and SIMS data [13].

$$p_p = \frac{1}{2} \left[N_A - N_D + \sqrt{(N_D - N_A)^2 + 4n_i^2} \right], \quad (33)$$

$$n_p = \frac{n_i^2}{p_p},$$

while, in the n -type emitter,

$$n_n = \frac{1}{2} \left[N_D - N_A + \sqrt{(N_A - N_D)^2 + 4n_i^2} \right], \quad (34)$$

$$p_n = \frac{n_i^2}{n_n},$$

where N_A and N_D are the acceptor and donor dopant concentrations, respectively, and n_i is the intrinsic carrier concentration, which is $9.65 \times 10^9 \text{ cm}^{-3}$ for room temperature silicon.

From Figure 18, the phosphorous donor concentration varies from approximately 10^{19} cm^{-3} to 10^{18} cm^{-3} across its depth. However, using the abrupt junction approximation to simplify the analysis, a constant value of $5 \times 10^{18} \text{ cm}^{-3}$ is assumed. The same approximation is done for the base, resulting in an average value of $5 \times 10^{17} \text{ cm}^{-3}$.

in the region. Since Figure 18 does not explicitly describe the collector concentration, it is assumed that they are 10^{15} cm^{-3} P donors and 10^{14} cm^{-3} B acceptors. Therefore, using Equations 33 and 34, the emitter, base, and collector carrier concentrations are

$$\begin{aligned} n_{n_E} &= 4.6 \times 10^{18} [\text{cm}^{-3}], p_{n_E} = 20 [\text{cm}^{-3}], \\ p_{p_B} &= 9 \times 10^{15} [\text{cm}^{-3}], n_{p_B} = 10^4 [\text{cm}^{-3}], \\ n_{n_C} &= 9 \times 10^{14} [\text{cm}^{-3}], p_{n_C} = 10^5 [\text{cm}^{-3}]. \end{aligned} \quad (35)$$

Of particular note from these results is that the donor concentration drives the emitter electron concentration, leaving few holes in this region, which is a very desirable condition because it increases the emitter efficiency.

Reexamining Equation 3, the two important concentration values for calculating gain are p_{n_E} and n_{p_B} , or the minority carrier concentrations for both emitter and base. An assumption already made but restated here is that the neutron-induced defect concentration will be on the order of the dopant concentrations of the emitter, and thus the hole concentration in the emitter will not be affected by the neutron radiation environment. From the results displayed in Equation 35,

$$p_{n_{Eo}} = p_{n_E}(t) = 20 [\text{cm}^{-3}], \quad (36)$$

for all times, t . On the other hand, the electron concentration in the base will be strongly dependent on the neutron flux, since the number of defects in a typical irradiation cycle will approach and possibly exceed the dopant concentration.

The diffusivity of the minority carriers in the emitter and base, D_{p_E} and D_{n_B} , depend on the carrier trap density in these regions. In the emitter, it is assumed that the radiation-induced defect concentration never approaches that of the donor concentration, N_{D_E} . Therefore, the donor concentration can be used to calculate the

diffusivity and mobility of holes in the emitter by interpolating from the empirical data in Sze [29], displayed in Figure 19. In the base, however, the concentration of neutron-induced trap sites caused by displacement damage can be on the same level or higher than the number of acceptors. Therefore, the sum of the two is necessary when calculating the interpolated value of diffusivity.

The diffusion length is the average length that the particular carrier will travel in the device region, which is a function of the square root of the product of diffusivity and carrier lifetime. Extending this, the carrier lifetime for some carrier x is calculated using the mobility of that carrier, μ_x , as $\tau_x = (\mu_x \cdot m_n) / q$ where m_n is the rest mass of the electron and q is the fundamental charge constant, set at 1.602×10^{-19} C. This particular parameter will be affected, albeit indirectly, by neutron-induced trap sites due to the change in mobility and diffusivity.

The change in the physical dimensions, *i.e.* W_b and W_e , are assumed to be negligible. While the introduction of additional trap sites may alter the regions of the BJT, it will be small compared to the actual dimensions of these regions. Therefore, they are set at a constant value and are unchanged during simulation.

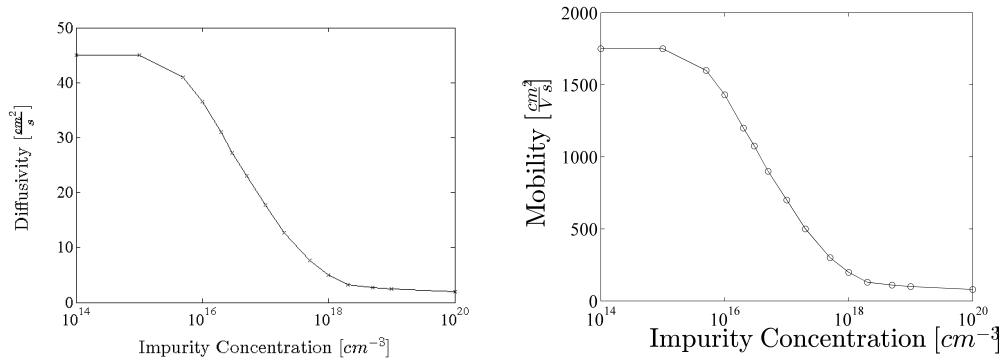


Figure 19. Diffusivity (left) and mobility (right) as a function of impurity concentration in the semiconductor bulk is flat till 10^{15} cm^{-3} ; it can be affected by radiation induced defects adding to the impurity concentration.

Results of Initial Model Implementation.

At this stage of development, the model contained 6 coupled, non-linear ODEs for the interactions of vacancies, divacancies, interstitials, impurity-vacancy complexes, impurity-divacancy complexes, and impurities. A test of the model using hypothetical parameters was accomplished to determine the validity of the results, and this is plotted in Figure 21.

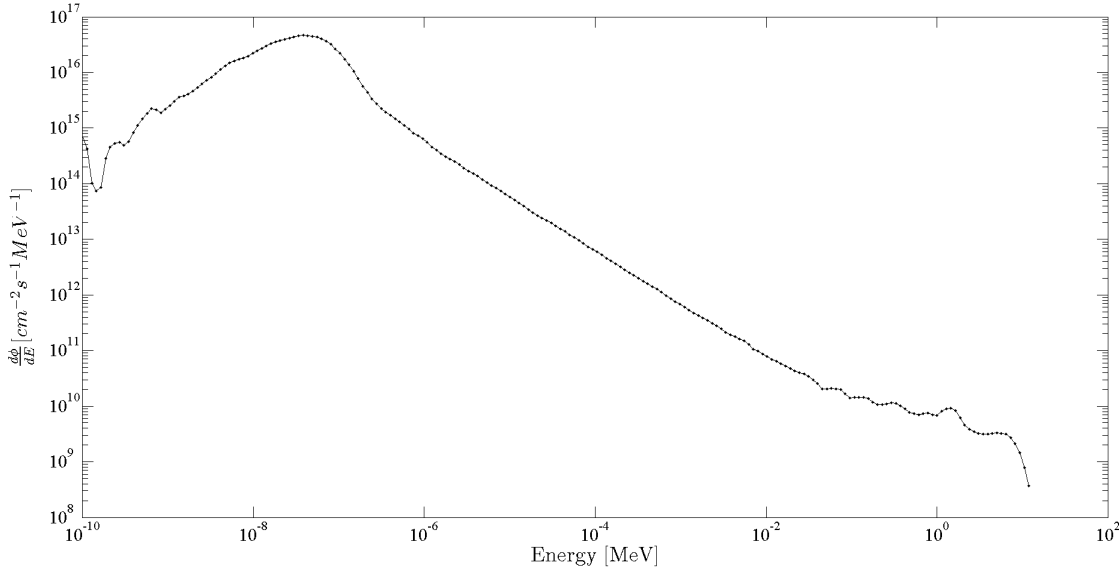


Figure 20. The neutron flux for the hypothetical situation in Figure 21 corresponds to a 1-MeV equivalent (Si) flux of 5×10^{10} n/cm²/s using the ASTM standard method of calculation.

The spectrum that was used for generation of defects was the time-averaged neutron spectrum from the IU NREF beamline. This was determined using MCNP-X and verified using multiple foil activation analysis. It is plotted in Figure 20. The initial concentration of all species except impurities was set to 10^{10} cm⁻³ to simulate a non-zero but negligible amount in relation to the number density of silicon atoms. The impurity concentration was the one exception, as it was set to 5×10^{15} at/cm³ to correspond to the typical dopant concentration in the 2n2222A base region. The vacancy, interstitial, and divacancy diffusivities were set to 3×10^{-10} cm²/s, 2×10^{-15}

cm^2/s , and $1 \times 10^{-16} \text{ cm}^2/\text{s}$, respectively. These values were selected because they fall within the typical range found in literature. The vibrational frequency of dissociation was also set to a value found in literature of 10^{13} s^{-1} for all defect species capable of dissociation (divacancies, vacancy-impurities, and divacancy-impurities). The capture radii were set to 1 \AA for all species.

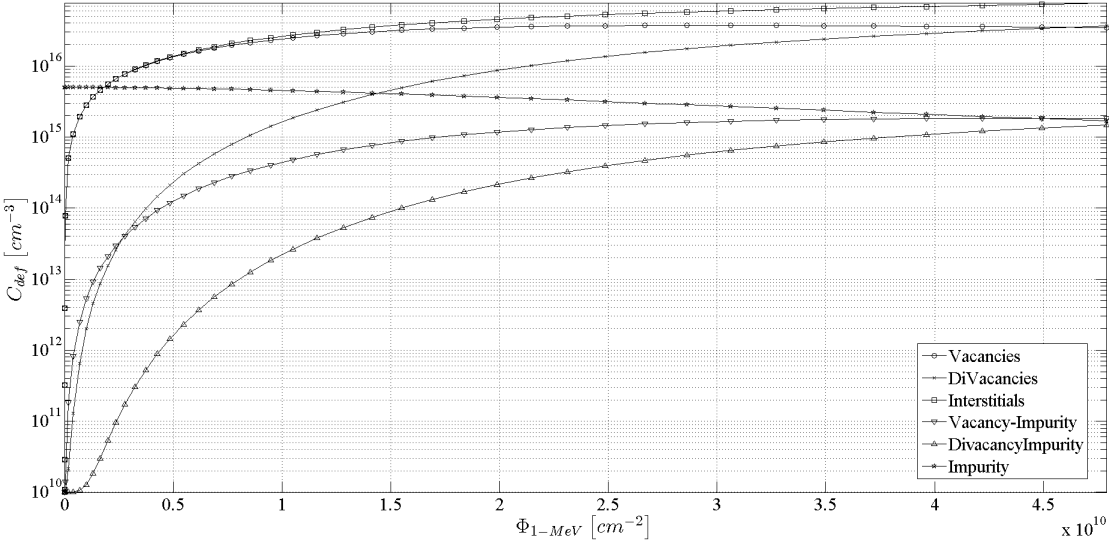


Figure 21. The first simulation using the model with six defect species and a time-averaged 1-MeV equivalent neutron flux of $5 \times 10^{10} \text{ n/cm}^{-2}/\text{s}$ and an initial impurity concentration of $5 \times 10^{15} \text{ at/cm}^3$.

Figure 21 presents the result of species formation during a simulated constant neutron flux. Most species initially rise in concentration, but there is a decline of vacancies after peaking at about $\Phi = 3 \times 10^{10} \text{ cm}^{-2}$. As in the previous model development steps, most of the defect species rise asymptotically as they approach the secular equilibrium between their respective creation and destruction mechanisms. However, vacancies and impurities are the exception. Vacancies rise asymptotically, but begin to decline after a time. This is due to an increase in the concentrations of defect species to which they can combine, such as other vacancies, interstitials, or other higher-order complexes. The impurity concentration declines because there are many avenues of removal with very few “creation” mechanisms for the impurity,

and those few creation paths have low probabilities of occurrence with the current parameter values used in the model.

Utilizing the results from this simulation and applying Equation 3 with the parameters already described, the device gain can be calculated. The result of this is plotted in Figure 22. The device gain response should be linear with respect to the fluence if the Messenger-Spratt equation is applicable. In examining Figure 22, the relation is initially linear but becomes sub-linear at approximately $1 \times 10^{10} \text{ cm}^{-2}$ and peaks around $3 \times 10^{10} \text{ cm}^{-2}$. This indicates that the modeled device anneals while still being irradiated due to the increase in vacancies and recombining events. It is because of this behavior that the model was further amended.

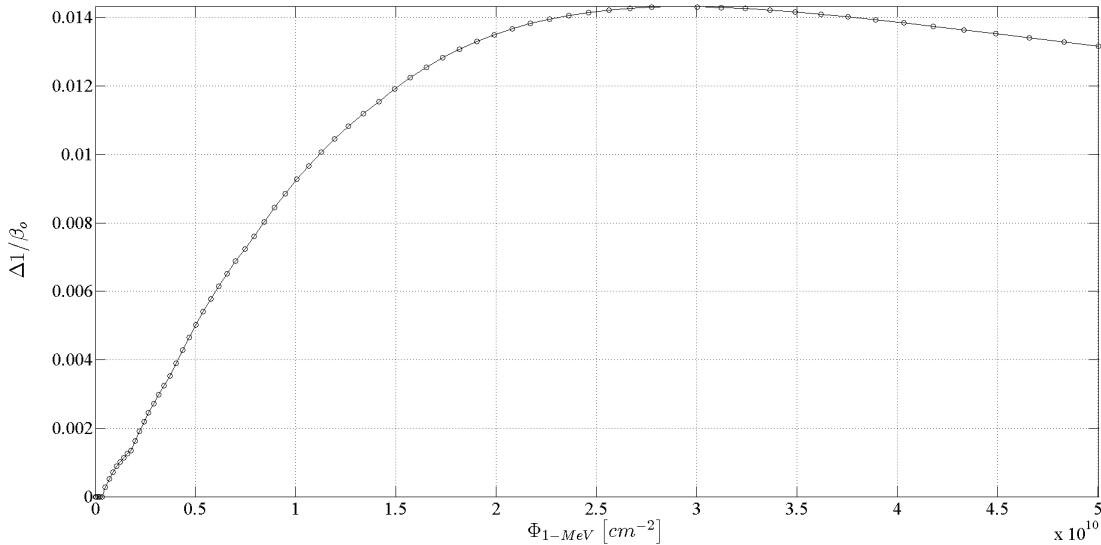


Figure 22. Results of the calculation of gain change as a function of fluence for the hypothetical situation uncover an issue with the model as it shows that the change in gain would begin to recover during irradiation, which is not observed in literature.

Step Seven – Adding Additional Species.

In the previous step, the high diffusivity of vacancies coupled with the additional destruction paths caused the vacancy concentration to decrease during irradiation.

This behavior lead to $\Delta(1/\beta)$ getting smaller while the device was being irradiated. This phenomenon has not been observed in literature.

Chakravarthi and Dunham discuss the fact that a “high supersaturation of vacancies... can lead to their aggregation into vacancy clusters” [30]. One aspect of neutron displacement damage that was not addressed in the initial model was the formation of vacancy clusters. These clusters form when one or more vacancies are in close proximity to other vacancies without filling adjacent lattice sites. By occupying close but not adjacent sites, they retain their original properties and do not become a divacancy, which occupies a different location within the silicon bandgap. However, because the silicon lattice is perturbed, vacancy mobility is decreased, and the vacancies do not anneal as quickly.

Therefore, two new species were created in the model representing called \mathcal{Z} - and \mathcal{S} -vacancy clusters. These clusters were added to the model in two ways. First, clusters were able to grow or dissolve with the collection or expulsion of a vacancy. Second, the clusters could interact with interstitials. These two processes are described by Equation Set 37.



The rate of increase of a species is given by $\alpha_{increase} = 4\pi D_v r_{capture}^{species}$ where D_v is the vacancy diffusion coefficient and $r_{capture}^{species}$ is the capture radius of the $n-1$ cluster. On the other hand, the rate of decrease for a cluster is given by Equation 38,

$$\alpha_{decrease} = \frac{1}{5 \times 10^{22}} \exp \left\{ \frac{E_b}{k_B T} \right\}, \tag{38}$$

where E_b is the barrier energy of breaking apart the cluster, k_B is the Boltzmann constant, and T is the temperature. The pre-factor of $(5 \times 10^{22})^{-1}$ was determined from atomistic calculations performed by Bongiorno et al. [31]. One could add as

many of these clusters as is feasible for time and computational resources. However, for this analysis, only the 2- and 3-vacancy clusters were considered. Taking the new processes into account yields two new equations,

$$\begin{aligned}\frac{dC_{2v}}{dt} &= \alpha_{12}C_vC_v - \alpha_{13}C_{2v} - \alpha_{14}C_iC_{2v} + \alpha_{15}C_v + \alpha_{16}C_iC_{3v} - \alpha_{17}C_{2v}, \\ \frac{dC_{3v}}{dt} &= \alpha_{18}C_vC_{2v} - \alpha_{19}C_{3v} + \alpha_{17}C_{2v} - \alpha_{16}C_iC_{3v}.\end{aligned}\quad (39)$$

However, this does not fully address the formation of defect clusters, since the model only allows them to be formed by vacancies being captured by other vacancies. However, this method was investigated to analyze the effects of clusters on the model.

The 2- and 3-vacancy cluster calculations lead to 8 total species being addressed. In order to verify the completeness of the system of differential equations, a 9thspecies was added: the *annihilation* species. This additional species accounts for the concentration of annihilations that occur between vacancies and interstitials in the bulk. Since the total number of vacancies that are created in the material can be directly tracked as a function of time, it can be compared against the number of vacancies that currently reside in the material at any time to ensure conservation of defects in the system of equations. Since this species is only included for accounting purposes, it can only be created. Therefore,

$$\frac{dC_{ann}}{dt} = \alpha_3C_vC_i + \alpha_8C_iC_{vx} + \alpha_9C_iC_{vvx} + \alpha_{14}C_iC_{2v} + \alpha_{16}C_iC_{3v}. \quad (40)$$

Now, if Equations 39 and 40 are added to Equation 30, the model becomes

$$\begin{aligned}
\frac{dC_v}{dt} &= G_v - 2\alpha_1 C_v C_v + 2\alpha_2 C_{vv} - \alpha_3 C_v C_i - \alpha_4 C_v C_x + \alpha_5 C_{vx}, \\
&\quad - \alpha_6 C_v C_{vx} + \alpha_7 C_{vvx} - 2\alpha_{12} C_v C_v + 2\alpha_{13} C_{2v} + \alpha_{14} C_i C_{2v}, \\
&\quad - \alpha_{15} C_v - \alpha_{18} C_v C_{2v} + \alpha_{19} C_{3v}, \\
\frac{dC_{vv}}{dt} &= \alpha_1 C_v C_v - \alpha_2 C_{vv} - \alpha_{11} C_{vv} C_x + \alpha_{10} C_{vvx}, \\
\frac{dC_i}{dt} &= G_i - \alpha_3 C_v C_i - \alpha_8 C_i C_{vx} - \alpha_9 C_i C_{vvx} - \alpha_{14} C_i C_{2v} + \alpha_{15} C_v, \\
&\quad - \alpha_{16} C_i C_{3v} + \alpha_{17} C_{2v}, \\
\frac{dC_{vx}}{dt} &= \alpha_4 C_v C_x - \alpha_5 C_{vx} - \alpha_6 C_v C_{vx} + \alpha_7 C_{vvx} + \alpha_9 C_i C_{vvx} - \alpha_8 C_i C_{vx}, \\
\frac{dC_{vvx}}{dt} &= \alpha_6 C_v C_{vx} - \alpha_7 C_{vvx} - \alpha_9 C_i C_{vvx} - \alpha_{10} C_{vvx} + \alpha_{11} C_{vv} C_x, \\
\frac{dC_x}{dt} &= -\alpha_4 C_v C_x + \alpha_5 C_{vx} + \alpha_8 C_i C_{vx} - \alpha_{11} C_{vv} C_x + \alpha_{10} C_{vvx}, \\
\frac{dC_{2v}}{dt} &= \alpha_{12} C_v C_v - \alpha_{13} C_{2v} - \alpha_{14} C_i C_{2v} + \alpha_{15} C_v + \alpha_{16} C_i C_{3v} - \alpha_{17} C_{2v}, \\
\frac{dC_{3v}}{dt} &= \alpha_{18} C_v C_{2v} - \alpha_{19} C_{3v} + \alpha_{17} C_{2v} - \alpha_{16} C_i C_{3v}, \\
\frac{dC_{ann}}{dt} &= \alpha_3 C_v C_i + \alpha_8 C_i C_{vx} + \alpha_9 C_i C_{vvx} + \alpha_{14} C_i C_{2v} + \alpha_{16} C_i C_{3v}.
\end{aligned} \tag{41}$$

With the model in this form, the conservation of vacancies can be verified if

$$C_{v,o} + G(t) \cdot t = C_v(t) + 2C_{vv}(t) + C_{vx}(t) + 2C_{vvx}(t) + 2C_{2v}(t) + 3C_{3v}(t), \tag{42}$$

which shows that the sum of the initial concentration and the total generation of vacancies at any time, t , is equal to the sum of all the concentrations of species with vacancies, subject to the number of vacancies within each one. Stated in another fashion, if

$$\frac{Vac_{accounted\ for} - Vac_{created}}{Vac_{created}} < \text{tolerance},$$

then conservation criteria have been satisfactorily met. Figure 23 is a plot of this

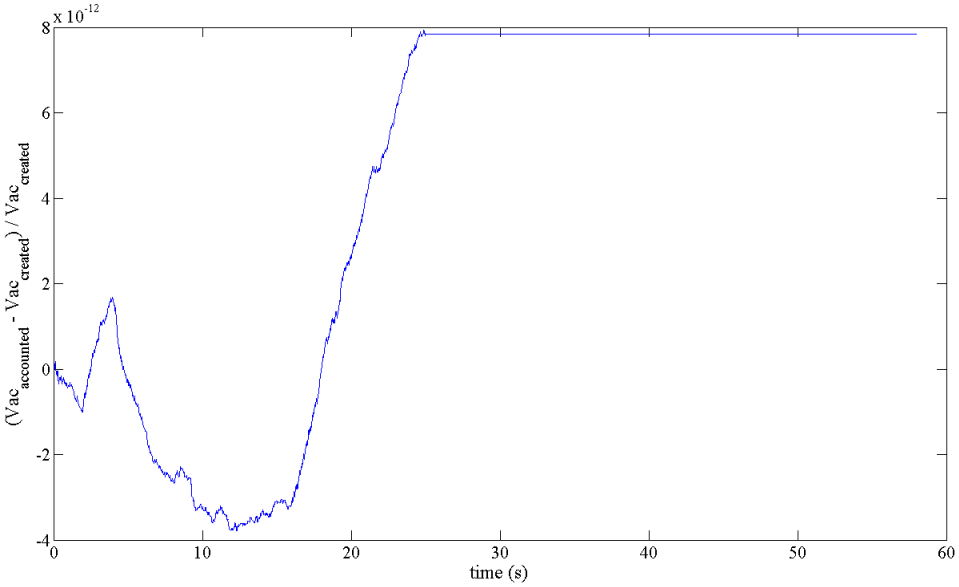


Figure 23. The calculation of residuals between vacancies “created” and vacancies “accounted for” is below the tolerance set for noise in the calculation, meaning that the value is effectively zero at all x-axis values.

calculation, showing that the residual stays under 8×10^{-12} at all times, which is below the tolerance set for machine precision in the numerical calculation of the residual itself.

Having ensured conservation criteria, there is one last couplet of species that was modeled. Originally, the carrier concentrations within the base were assumed constant. This is not realistic, as the radiation-induced defects very strongly affect the number of charge carriers. Therefore, two additional species were modeled: the holes (majority carrier) and electrons (minority carrier) in the base.

Typically, divacancy defect species lie at the approximate center of the bandgap in silicon semiconductors. Therefore, thermal generation of carriers occurs from these trap sites adding electrons and holes. Additionally, divacancies act as recombination centers for the minority carrier, removing electrons due to recombination. These phenomena are implemented in the following equations,

$$\begin{aligned}\frac{dC_{h^+}}{dt} &= G_\gamma + \alpha_{20} C_{vv}, \\ \frac{dC_{e^-}}{dt} &= G_\gamma - \alpha_{21} C_{vv} C_{e^-} + \alpha_{22} C_{vv},\end{aligned}\tag{43}$$

where G_γ is the generation rate of electron-hole pairs due to deposition of ionization energy from gamma interactions in the silicon semiconductor. In this equation,

$$\begin{aligned}\alpha_{20} &= v_{th} \sigma_{p^+} n_i \exp \left\{ (E_t - E_i) / (k_B T) \right\}, \\ \alpha_{21} &= v_{th} \sigma_{n^-}, \\ \alpha_{22} &= v_{th} \sigma_{n^-} n_i \exp \left\{ (E_i - E_t) / (k_B T) \right\}.\end{aligned}\tag{44}$$

where v_{th} is the thermal velocity of the electron, E_t is the mid-gap energy, and E_i is the intrinsic Fermi level within the bandgap. The thermal velocity is calculated as $v_{th} = \sqrt{3k_B T/m_n} = 2.29 \times 10^7 \text{ cm/s}$. For silicon, $E_t = 1.1/2 = 0.55 \text{ eV}$. The intrinsic Fermi level can be calculated as

$$E_i = \frac{E_g}{2} + \frac{1}{2} k_B T \ln \left(\frac{N_v}{N_c} \right),\tag{45}$$

where $N_v = 2.66 \times 10^{19} \text{ cm}^{-3}$ and $N_c = 2.86 \times 10^{19} \text{ cm}^{-3}$ are the density of states in the valence and conduction bands, respectively, for room temperature silicon.

Finally, Equation 43 can be combined with Equation 41 to reach the model state with eleven tracked species. This is given in Equation Set 46.

$$\begin{aligned}
\frac{dC_v}{dt} &= G_v - 2\alpha_1 C_v C_v + 2\alpha_2 C_{vv} - \alpha_3 C_v C_i - \alpha_4 C_v C_x + \alpha_5 C_{vx} \\
&\quad - \alpha_6 C_v C_{vx} + \alpha_7 C_{vwx} - 2\alpha_{12} C_v C_v + 2\alpha_{13} C_{2v} + \alpha_{14} C_i C_{2v} \\
&\quad - \alpha_{15} C_v - \alpha_{18} C_v C_{2v} + \alpha_{19} C_{3v} \\
\frac{dC_{vv}}{dt} &= \alpha_1 C_v C_v - \alpha_2 C_{vv} - \alpha_{11} C_{vv} C_x + \alpha_{10} C_{vwx} \\
\frac{dC_i}{dt} &= G_i - \alpha_3 C_v C_i - \alpha_8 C_i C_{vx} - \alpha_9 C_i C_{vwx} - \alpha_{14} C_i C_{2v} + \alpha_{15} C_v \\
&\quad - \alpha_{16} C_i C_{3v} + \alpha_{17} C_{2v} \\
\frac{dC_{vx}}{dt} &= \alpha_4 C_v C_x - \alpha_5 C_{vx} - \alpha_6 C_v C_{vx} + \alpha_7 C_{vwx} + \alpha_9 C_i C_{vwx} - \alpha_8 C_i C_{vx} \\
\frac{dC_{vwx}}{dt} &= \alpha_6 C_v C_{vx} - \alpha_7 C_{vwx} - \alpha_9 C_i C_{vwx} - \alpha_{10} C_{vwx} + \alpha_{11} C_{vv} C_x \tag{46} \\
\frac{dC_x}{dt} &= -\alpha_4 C_v C_x + \alpha_5 C_{vx} + \alpha_8 C_i C_{vx} - \alpha_{11} C_{vv} C_x + \alpha_{10} C_{vwx} \\
\frac{dC_{2v}}{dt} &= \alpha_{12} C_v C_v - \alpha_{13} C_{2v} - \alpha_{14} C_i C_{2v} + \alpha_{15} C_v + \alpha_{16} C_i C_{3v} - \alpha_{17} C_{2v} \\
\frac{dC_{3v}}{dt} &= \alpha_{18} C_v C_{2v} - \alpha_{19} C_{3v} + \alpha_{17} C_{2v} - \alpha_{16} C_i C_{3v} \\
\frac{dC_{ann}}{dt} &= \alpha_3 C_v C_i + \alpha_8 C_i C_{vx} + \alpha_9 C_i C_{vwx} + \alpha_{14} C_i C_{2v} + \alpha_{16} C_i C_{3v} \\
\frac{dC_{h^+}}{dt} &= G_\gamma + \alpha_{20} C_{vv} \\
\frac{dC_{e^-}}{dt} &= G_\gamma - \alpha_{21} C_{vv} C_{e^-} + \alpha_{22} C_{vv}
\end{aligned}$$

Step Eight – Temporal Profile Capability.

The final step in the model development involved adding the ability to simulate a continuously pulsing radiation environment. While the model could address constant fluence sources such as a nuclear reactor, accelerator-driven neutron sources such as the Indiana University (IU) Neutron Radiation Effects Facility (NREF) operate in pulsed modes. During each cycle, there is a period of beam “on” followed by a period of beam “off”. Therefore, the model must be able to account for this.

An approach was taken by breaking the calculation steps into individual cycles of operative and inoperative mode. During each irradiation cycle, the generation rates are set to positive values and calculation progresses for the period of time correlating to the pulse width of the proton source. Then, when switching to the “off” cycle, the initial conditions of the simulation are set to the final conditions of the previous cycle, the generation rates are set to zero, and the calculation again progresses for the period of time that correlates to the remainder of a single pulse period. As an example, if the beam frequency is 20 Hz and the pulse width is 400 μ s, this means that the operative mode would be 400 μ s while the “off” state would last 49.6 ms.

3.3 Initial Model Results

An initial set of model simulations was accomplished to assess the performance and computational intensity of the model. The parameter set for this analysis are tabulated in Table 4.

The simulation was a 10 s irradiation by a neutron source with energy and flux similar to the IU NREF accelerator-driven source followed by a 10 s annealing period. The spectrum was as shown in Figure 20, and it has a time-averaged 1-MeV equivalent(Si) neutron flux of approximately 5×10^{10} n/cm²/s.

The simulation was then conducted for irradiation and annealing times from 10 through 1000 s, in order to monitor model computation times and ensure that the simulation was stable and repeatable. Figure 24 displays the results of these simulations.

As expected, the required computational time was roughly linear with respect to the simulated irradiation time. The data can be fit to a plane by $t_{comp} = 0.7t_{irr} + 0.128t_{anneal} + 13.36$. If this result can be extrapolated to longer irradiation and annealing intervals, a 20 minute irradiation followed by a 20 minute annealing interval

Table 4. Model parameters selected for test run of final model design. The lattice constant a_o for silicon at room temperature is 5.4307×10^{-8} cm.

Parameter	Species	Value	Units
D	Vacancy	10^{-10}	cm^2/s
	Interstitial	10^{-15}	
	Divacancy	10^{-15}	
E_{barrier}	Divacancy	1.6	eV
	Vac-Imp	1.7	
	Divac-Imp to Vac/Vac-Imp	2.24	
	Divac-Imp to Divac/Imp	2.98	
ν_{diss}	Divacancy	10^{13}	1/s
	Vac-Imp	10^{13}	
	Divac-Imp	10^{13}	
r_{cap}	V and I	$2a_o$	cm
	V and V	$2a_o$	
	V and Imp	$2a_o$	
	V and Vac-Imp	$10a_o$	
	I and Vac-Imp	$10a_o$	
	I and Divac-Imp	$10a_o$	
	Divac and Imp	$10a_o$	
Init. Cond.	Vacancies	10^{13}	cm^{-3}
	Divacancies	10^{13}	
	Interstitials	10^{13}	
	Vac-Imp	10^{10}	
	Divac-Imp	10^{10}	
	Impurities	5×10^{15}	
	2-Vac Clusters	10^{10}	
	3-Vac Clusters	10^{10}	
	Annihilations	10^{10}	
	Electrons	10^4	
E_{fp}	Holes	C_{imp}	
I_{beam}	N/A	40	eV
f_{beam}	N/A	20	mA
PW_{beam}	N/A	20	Hz
		400	μs

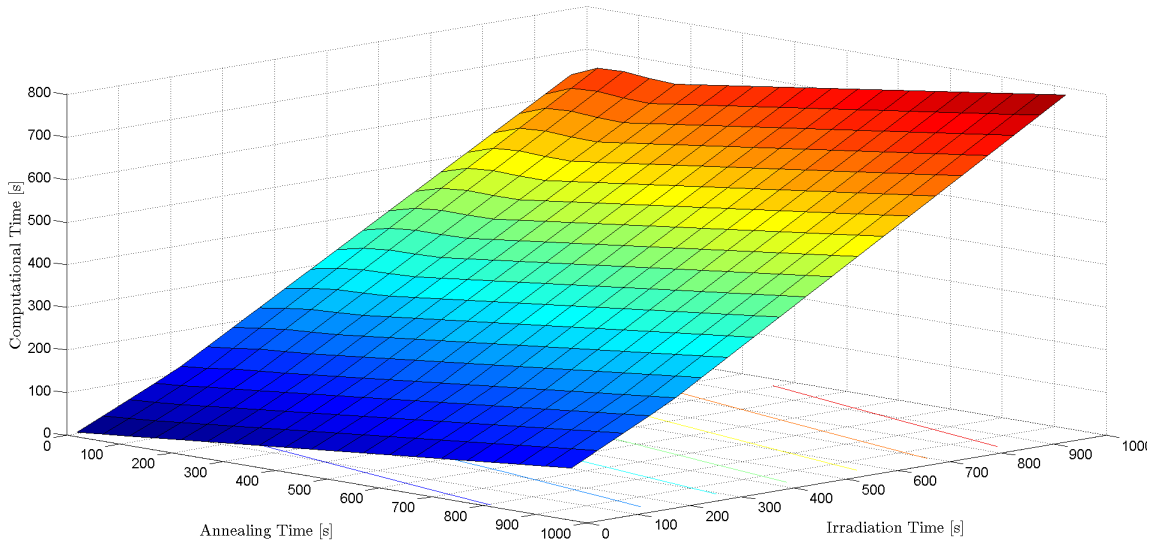


Figure 24. The test of computational time versus irradiation and annealing time showed a nearly linear relationship from 0 s to 1200 s.

would take almost 17 minutes, and an hour long irradiation followed by a 3 hour long annealing interval would require just over an hour of computational time. Thus, simulating short irradiation periods is feasible but longer irradiations become time-intensive and may require code modifications to accelerate convergence.

Also, for longer irradiation times, the longer it takes to fully anneal defects, which increases overall computation time. This was also expected due to the way that annealing time was addressed in the code. Since there was no pulsing during annealing, the entire annealing interval could be approached as a single solution step. This is in contrast to the irradiation time, where each interval of irradiation and annealing must be calculated separately. In the end, the model was found to be stable and the computational times reasonable for the current application.

After testing for stability and repeatability, one of the simulation sets was analyzed for important features. The 10 s irradiation and annealing interval simulation is plotted in Figure 25. The first feature to note is that the vacancy concentration, which starts at 10^{13} cm^{-3} rises quickly to 10^{16} cm^{-3} , and there is a very distinct

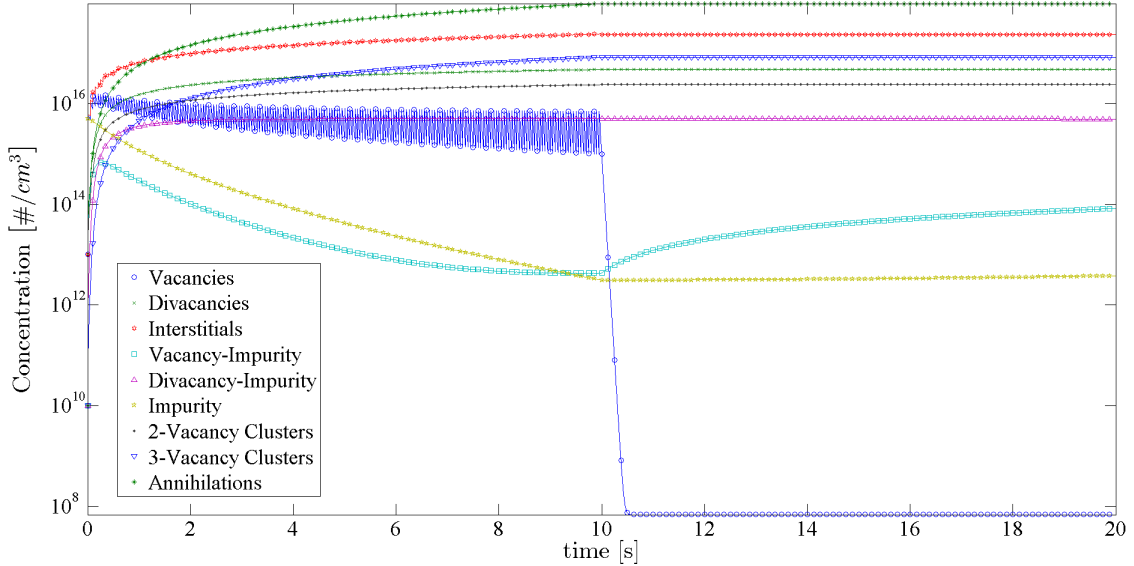


Figure 25. The plot of species concentrations after simulating a 10 s irradiation period followed by a 10 s annealing period displays a noticeable vacancy defect concentration increase and subsequent annealing during each pulse cycle.

growth and annealing of the vacancies during each pulse cycle. This leads to a distinctive sawtooth pattern in the $\Delta(1/\beta)$ versus fluence graph. Additionally, when the irradiation is stopped at 10 s, the vacancy concentration drops quickly as they are consumed by annealing. The other defect species rise asymptotically, as in the previous versions of the model; and after irradiation, they remain constant over the time interval simulated.

In Figures 26 and 27, gain is calculated and plotted for the irradiation and annealing phases of the model. In Figure 26, the change in gain with neutron fluence is plotted during the irradiation interval. The slope of this curve is $2.5 \times 10^{-13} \text{ cm}^2/\text{n}$ and is a direct measurement of the damage constant for these simulation parameters, due to the Messenger-Spratt equation. This value of the damage constant is about two orders of magnitude larger than the 1.5×10^{-15} stated in literature [32] for 2N2222 Si BJTs for 1-MeV equivalent neutrons in silicon. This may be indicative of parameter values that are incorrect. It may also indicate that there are other physical processes at work that are not captured in the model.

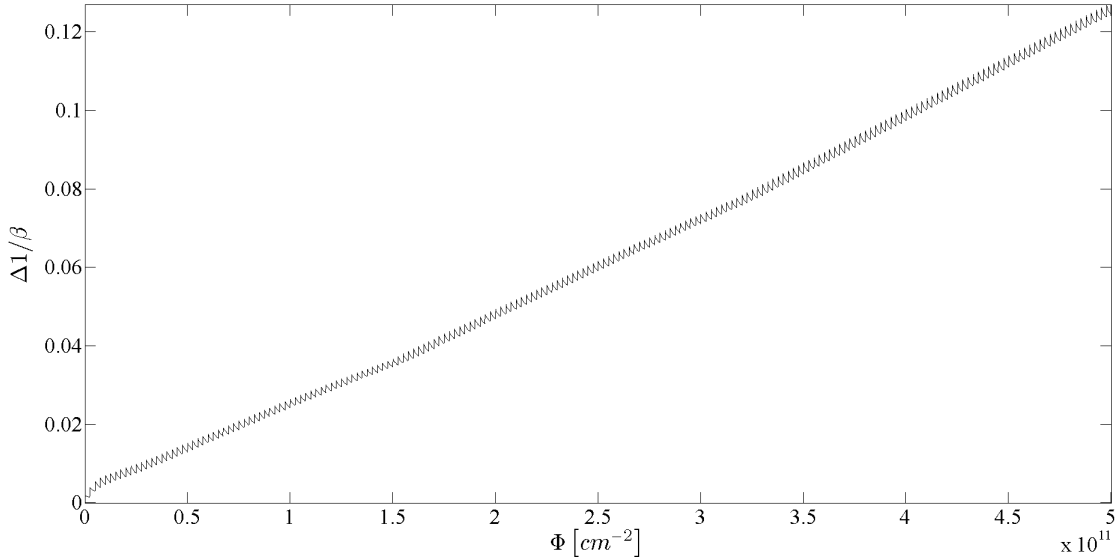


Figure 26. The change in gain as a function of fluence during irradiation calculated using the model developed in this research. It simulates a 10 s irradiation period and displays a generally linear response with a sawtooth-like pattern corresponding to irradiation and annealing during a pulse cycle.

When considering the annealing behavior, the *annealing factor* is an additional measure of the transient annealing response in devices. The annealing factor is defined [33] as

$$AF(t) = \frac{1/\beta(t) - 1/\beta_o}{1/\beta_f - 1/\beta_o}.$$

The initial gain in the device is β_o , which acts as a normalizing factor that takes variability in device parameters into account, β_f is the final gain in the device at long time, and $\beta(t)$ is the gain at a particular time, t .

The first trend to notice in Figures 26 and 27 is that $\Delta(1/\beta)$ approaches its final value, *i.e.* that value where $1/\beta \rightarrow 1/\beta_f$ and annealing is complete, in under 1 s. This is not supported by experiments or literature. However, the model is stable and results are repeatable. With these initial results, experimental results were needed.

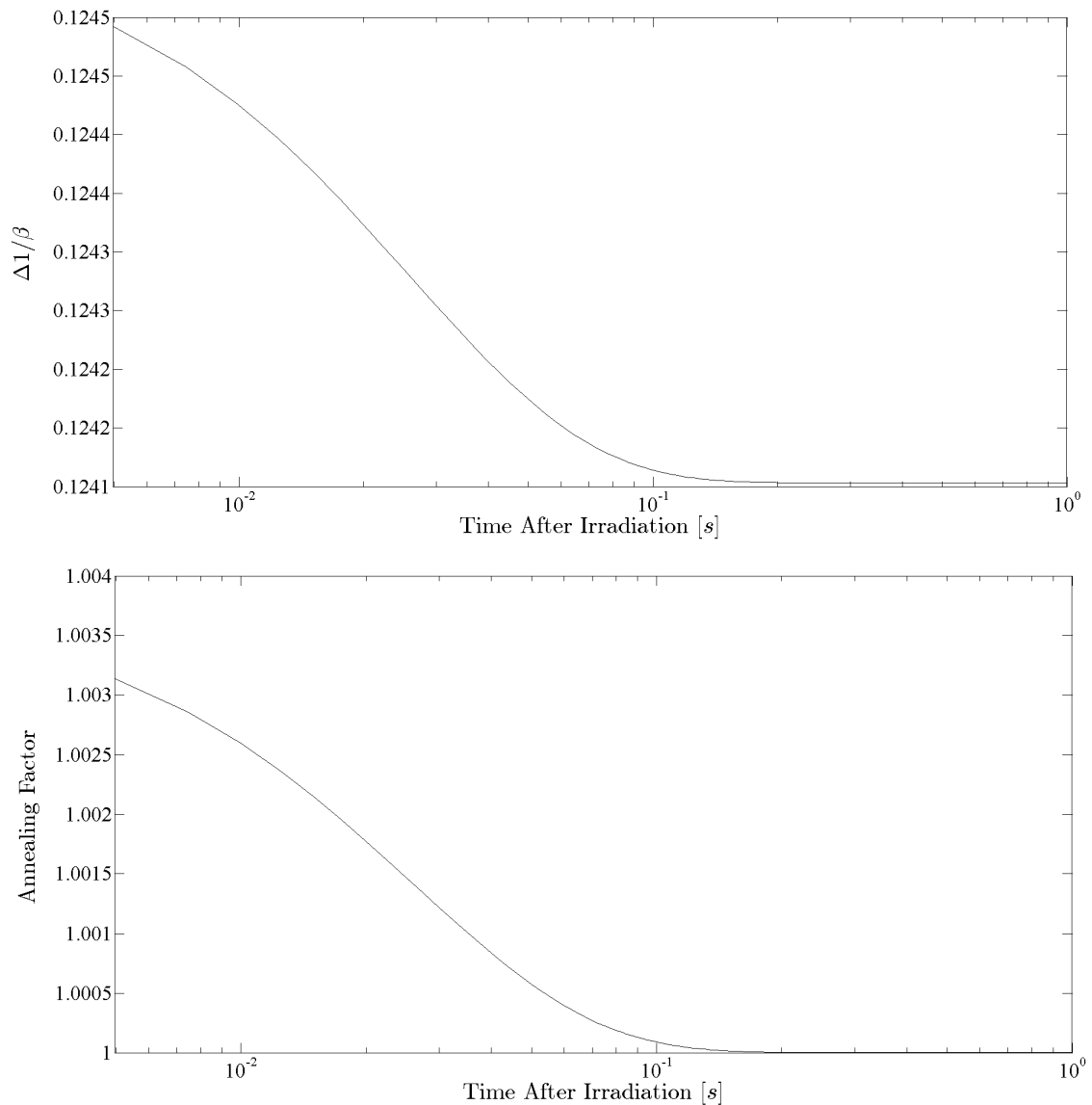


Figure 27. (Top) The simulated change in gain during annealing. (Bottom) The simulated annealing factor after irradiation. Annealing in the model occurs quite quickly and approaches the final value within less than 1 s.

References

1. J. Srour, C. Marshall, and P. Marshall, "Review of displacement damage effects in silicon devices," *IEEE Trans. Nucl. Sci.*, vol. NS-50, no. 3, pp. 653–670, 2003.
2. G. Messenger and J. Spratt, "The effects of neutron irradiation on silicon and germanium," in *Proc. IRE*, vol. 46, June 1958, pp. 1038–1044.
3. G. Messenger, "A general proof of the β degradation equation for bulk displacement damage," *IEEE Trans. Nucl. Sci.*, vol. 20, no. 1, pp. 809–810, 1973.
4. A. Gover, J. Grinberg, and A. Seidman, "Computation of bipolar transistor base parameters for general distribution of impurities in base," *IEEE Trans. Elect. Dev.*, vol. ED-19, no. 8, pp. 967–975, 1972.
5. M. Frank and F. Larin, "Effect of operating conditions and transistor parameters on gain degradation," *IEEE Trans. Nucl. Sci.*, vol. 12, no. 5, pp. 126–133, 1965.
6. C. Ramsey and P. Vail, "Current dependence of the neutron damage factor," *IEEE Trans. Nucl. Sci.*, vol. 17, no. 6, pp. 310–316, 1970.
7. J. Williams, P. Griffin, D. King, D. Vehar, T. Schnauber, S. Luker, and K. De Priest, "Simultaneous evaluation of neutron spectra and 1-MeV-equivalent (Si) fluences at SPR-III and ACRR," *IEEE Trans. Nucl. Sci.*, vol. 54, no. 6, pp. 2296–2302, 2007.
8. E. Bielejec, G. Vizkelethy, N. Kolb, D. King, and B. Doyle, "Damage equivalence of heavy ions in silicon bipolar junction transistors," *IEEE Trans. Nucl. Sci.*, vol. 53, no. 6, pp. 3681–3686, 2006.
9. X. Li, H. Geng, M. Lan, D. Yang, S. He, and C. Liu, "Degradation mechanisms of current gain in npn transistors," *Chin. Phys. B*, vol. 19, no. 6, pp. 066103–1 – 066103–8, 2010.
10. C. Consolandi, P. D'Angelo, G. Fallica, R. Mangoni, R. Modica, S. Pensotti, and P. Rancoita, "Systematic investigation of monolithic bipolar transistors irradiated with neutrons, heavy ions and electrons for space applications," *Nuclear Instruments and Methods in Physics Research Section B: Beam Interactions with Materials and Atoms*, vol. 252, no. 2, pp. 276 – 284, 2006.
11. J. Rosenfeld, *TREE Simulation Facilities*, 2nd ed., General Electric Company, Santa Barbara CA TEMPO, January 1979.
12. I. Arimura, "Effects of circumvention and temperature on neutron-induced rapid annealing," *IEEE Trans. Nucl. Sci.*, vol. 17, no. 6, pp. 348–353, December 1970.

13. E. Keiter, T. Russo, C. Hembree, and K. Kambour, “A physics-based device model of transient neutron damage in bipolar junction transistors,” *IEEE Trans. Nucl. Sci.*, vol. 57, no. 6, pp. 3305–3313, Dec 2010.
14. Y. Shi, D. Shen, F. Wu, M. Deng, and K. Cheng, “On the formation of defect clusters in neutron-irradiated Si,” *Appl. Phys. A*, vol. 50, pp. 305–309, 1990.
15. W. Shockley, “The theory of *pn* junctions in semiconductors and *pn* junction transistors,” *Bell Syst. Tech. J.*, vol. 28, no. 3, pp. 435–489, 1949.
16. H. Bateman, “Solution of a system of differential equations occurring in the theory of radioactive transformations,” *Proc. Cambridge Philos. Soc.*, vol. 15, no. pt V, pp. 423–427, 1910. [Online]. Available: <http://citebank.org/node/122715>
17. Matlab - the language of technical computing. [Online]. Available: <http://www.mathworks.com/products/matlab/>
18. I. Verner, J. Corbett, and N. Gerasimenko, *Chaos and stability in defect processes in semiconductors*. Trans Tech Publications, 1993.
19. ASTM Standard E722-09(e1), *Standard Practice for Characterizing Neutron Energy Fluence Spectra in Terms of an Equivalent Monoenergetic Neutron Fluence for Radiation-Hardness Testing of Electronics*, ASTM International, West Conshohocken, PA, 2009.
20. ICRU 13, “Neutron fluence, neutron spectra, and kerma,” International Commission on Radiation Units and Measurements, 7910 Woodmont Ave., Bethesda, MD 20814, Tech. Rep., 1969.
21. K. Wang, Y. Lee, and J. Corbett, “Defect distribution near the surface of electron irradiated silicon,” *Appl. Phys. Lett.*, vol. 33, no. 6, pp. 547–548, 1978.
22. A. Hallén, N. Keskitalo, and B. Svensson, “Diffusion and reaction kinetics of fast-ion-induced point defects studied by deep-level transient spectroscopy,” *Defect Diffus Forum*, vol. 153-155, pp. 193–204, 1998.
23. V. Voronkov and R. Falster, “Vacancy-type microdefect formation on Czochralski silicon,” *J. Crys. Growth*, vol. 194, pp. 76–88, 1996.
24. S. Libertino and S. Coffa, “Room temperature diffusivity of self-interstitials and vacancies in ion-implanted Si probed by *in situ* measurements,” *Appl. Phys. Lett.*, vol. 73, no. 23, pp. 3369–3371, 1998.
25. ——, “Room temperature point defect migration in crystalline Si,” *Solid State Phenom*, vol. 82-84, pp. 201–212, 2002.
26. N. Cowern, G. Van de Walle, P. Zalm, and D. Oostra, “Reactions of point defects and dopant atoms in silicon,” *Phys. Rev. Lett.*, vol. 69, no. 1, pp. 116–119, 1992.

27. G. Watkins and J. Corbett, “Defects in irradiated silicon: EPR of the divacancy,” *Phys. Rev.*, vol. 138, no. 2A, pp. A543–A555, 1965.
28. M. Furuhashi and K. Taniguchi, “Formation mechanisms of divacancy-oxygen complex in silicon,” *J Electrochem. Soc.*, vol. 155, no. 3, pp. H160–H163, 2008.
29. S. Sze, *Semiconductor Devices: Physics and Technology*, 2nd ed. John Wiley & Sons, Inc., 2002.
30. S. Chakravarthi and S. Dunham, “Modeling of vacancy cluster formation in ion implanted silicon,” *J. Appl. Phys.*, vol. 89, p. 4758, 2001.
31. A. Bongiornio, L. Colombo, and T. Diaz De la Rubia, “Structural and binding properties of vacancy clusters in silicon,” *Europhys. Lett.*, vol. 43, p. 695, 1998.
32. ASTM Standard E1855-10, *Standard Test Method for Use of 2N2222A Silicon Bipolar Transistors as Neutron Spectrum Sensors and Displacement Damage Monitors*, ASTM International, West Conshohocken, PA, 2010.
33. B. Gregory and H. Sander, “Transient annealing of defects in irradiated silicon devices,” in *Proceedings of the IEEE*, vol. 58, no. 9, 1970, pp. 1328–1341.

IV. Experimental Verification

In the first step of this work, a time-dependent system of coupled, non-linear ODEs was solved using reaction kinetics to determine defect species' concentrations as they formed, interacted, and were annihilated. The solution of this system of equations provides insight into the concentration and type of defects that affect device gain through their effect on the base dopant and minority carrier parameters.

While the development of this model is an important step in the process of investigating temporal and spectral dependence in neutron displacement damage studies, the next step is to use experimental measurements to validate the findings. This data will help to predict the device gain, using a controlled laboratory environment. Additionally, the question arises as to whether the flux temporal and spectral profiles have an effect on the device performance. This can be investigated by comparing results of measurements from two different facilities: the accelerator-driven neutron source at IU NREF and a steady-state neutron source at the Ohio State University Research Reactor (OSURR). The facility at IU NREF has a much harder spectrum approximately 8 neutrons for every gamma ray, while the thermal spectrum at the OSURR has approximately 10 gamma photons emitter per neutron. These two facilities will provide a good contrast in both time and neutron energy spectrum for this comparison. It is expected that the neutron source temporal profile will affect the rate at which damage is occurring, and that the neutron energy spectrum shape will affect the defect species being created, and thus the damage manifested in the device.

In the following sections, the experimental work that was completed during this research will be presented in detail, to include the procedures, the equipment used, and the methodology employed. The results, which show that device performance degradation during irradiation is definitely different for a varying flux profile, will be presented and analyzed.

4.1 IU NREF Experiments

In this set of experiments, the IU NREF neutron source, which is a continuously-pulsed neutron source, was used to damage silicon BJTs and the device gain was recorded to measure the amount of displacement damage that occurred in the device. Three types of experiments were accomplished: an interval test, a multiple-fluence test, and an ASTM standard-based test. Gain was measured in two ways, as described in Table 5. First, the collector and base were sourced with a constant voltage, the emitter was sourced with a constant current, and the current of the collector and base was measured. Second, the base voltage and emitter current were sourced, but the voltage on the collector was swept from -1 to +10 V, while the base and collector currents were again measured.

Table 5. BJT operating parameters for two measurement methods.

Leg	#1	#2
Collector [V]	+10	Swept from -1 to +10
Base [V]	0	0
Emitter [μ A]	-220	-220

The results of these experiments show that the device gain degradation follows a Messenger-Spratt linear relationship. However the damage constant is greater than the value specified in the ASTM E1855-10, the Standard Test Method for Use of 2N2222A Silicon Bipolar Transistors as Neutron Spectrum Sensors and Displacement Damage Monitors [1]. In the following subsections, the facilities at IU NREF will be explained in greater detail, the equipment used for each of the experiment sets will be described, and the results and analysis of each experiment set will be presented.

Facility Description.

At the IU Center for Exploration of Energy and Matter (CEEM), there is a pulsed neutron source that produces neutrons via the inelastic scattering of protons on beryl-

lium. Protons are created in an ion source, then are accelerated and directed onto a target assembly inside a moderator/reflector stack where neutrons are created. A more detailed description of the facility can be found in other sources [2–5], and a schematic of the facility is displayed in Figure 28.

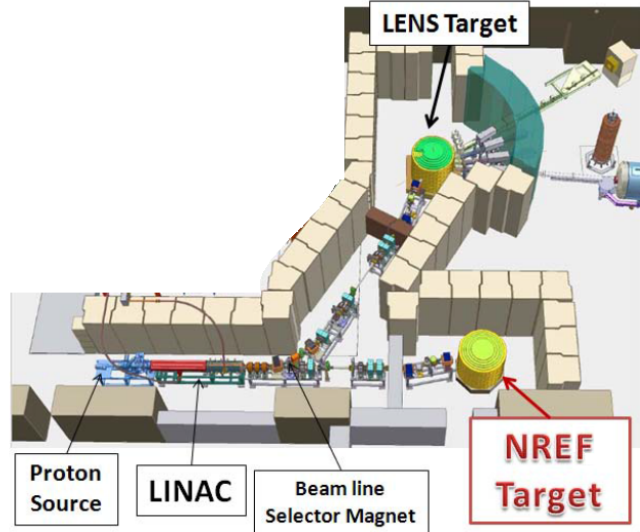


Figure 28. The IU LINAC Facility schematic shows the proton source and LINAC at bottom left; the beam is split to targets in lower right and upper middle [6].

On a basic level, the IU NREF facility is made up of a linear accelerator that bombards a beryllium target with protons, producing neutrons primarily via the (p,n) inelastic reaction. The linear accelerator is capable of a maximum energy of 13 MeV using one radio-frequency quadrupole and two drift tube Linear Accelerators (LINAC). The LINAC is powered by klystrons and must be pulsed in a repetitious manner, leading to a distinct duty factor. This duty factor is variable, but the NREF is typically operated with a duty factor of around 0.8%. The frequency of operation is 20 Hz and the pulse width of the proton packets is between 100-1000 μs . An example of a proton pulse flux profile is displayed in Figure 29.

After acceleration through the RFQ and LINACS, the protons can be directed down one of two beam lines using a selector magnet. The existence of two beam

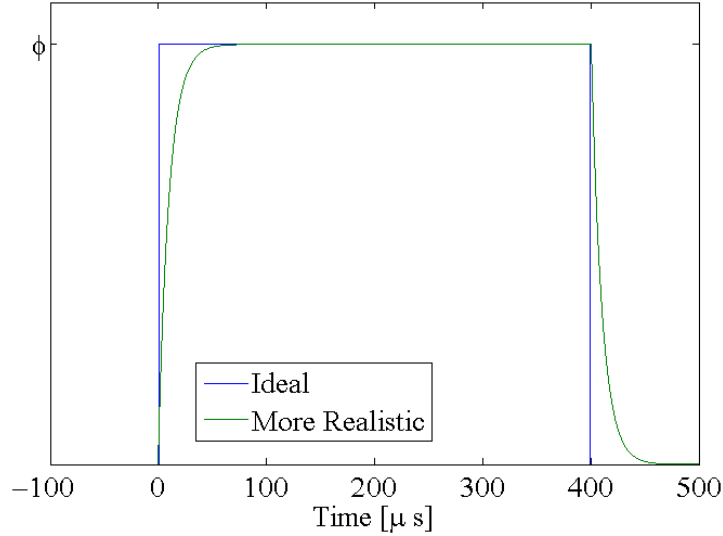


Figure 29. The IU NREF beam is pulsed, and the duty cycle is typically around 0.8% with the current configuration. Ideally, the beam pulse is a square wave; however, each pulse has a rise and fall transient.

lines gives the facility increased flexibility in experiment set-up and operation. The first beam line is called the Low-Energy Neutron Source (LENS) beam line, while the second is called the Neutron Radiation Effects Facility (NREF) beam line. Neutron production at the LENS target has been analyzed extensively [7], however the moderator configuration makes the LENS target impractical for use in radiation effects studies of this type.

In previous work by this author and others [2–4, 7–10], the neutron energy spectra for the LINAC’s two beamlines (the LENS and the NREF) has been characterized. The spectrum of the LENS is significantly moderated, *i.e.* slowed down, so that the neutrons may interact with and probe the structure of materials. Since one of our main goals in doing neutron displacement damage studies is to simulate (as closely as possible) the environment in which the devices may have to operate, this facility is not of great interest. Additionally, the extremely low energy of the neutrons of the LENS will be so small that very little damage will occur. It is for these reasons that the NREF is the beamline of greater interest in this research.

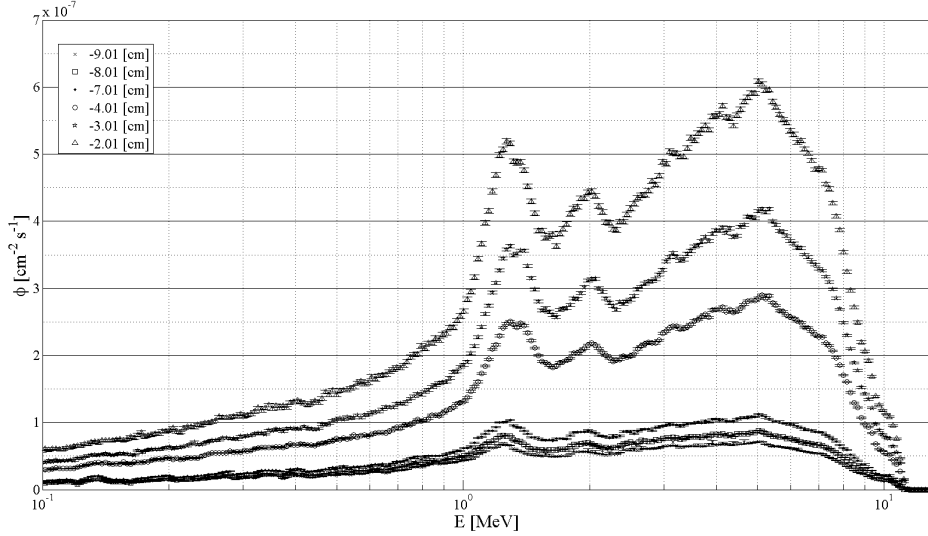


Figure 30. Using Monte Carlo particle simulation software and an input deck provided by IU NREF personnel [11], the neutron spectrum was calculated on a *per proton* basis and at different distances from the beryllium target; this can then be scaled based on the proton source specifications for a particular run.

The NREF has been modified recently to accommodate the radiation effects on electronics community. The spectrum was hardened, meaning that the average neutron energy is skewed to higher energy; and the maximum neutron energy is approximately 11 MeV. In Figure 30, the neutron energy spectrum is plotted as a function of energy and per a single, incident proton. In this way, the spectrum can be scaled for any proton beam current, which is dependent on the beam’s operating parameters. Usually, the beam is operated at a current of 20 mA, and this scaled spectrum is plotted in Figure 31.

NREF Experiment 1: Exploration Experiments.

The first set of experiments at the IU NREF was an investigation of the feasibility of the experimental method devised to collect BJT gain degradation data. To this end, a number of procedures were tested for use in the second set of experiments.

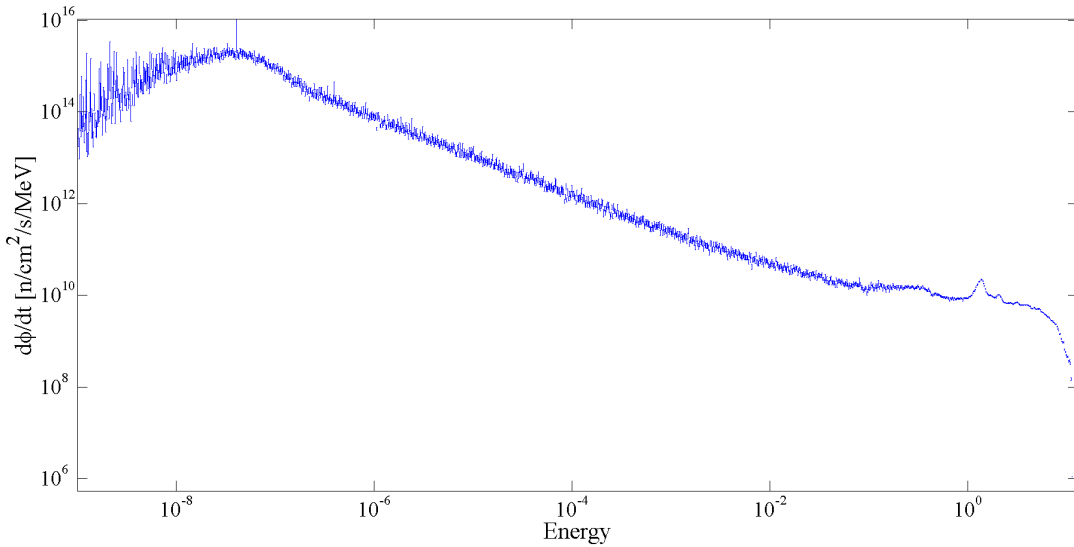


Figure 31. When operating the proton source at a current of 20 mA, the resultant neutron spectrum is scaled to a 1-MeV equivalent (Si) neutron flux of $> 6 \times 10^{10}$ n/cm²/s.

Test Equipment.

The equipment used for this experiment included three Keithley 237 Source Measurement Units (SMU), a switchbox, and a test fixture. The latter two pieces of equipment were built specifically for this experiment. Figure 32 displays a picture of the equipment set-up for the irradiation portion of the experiment.

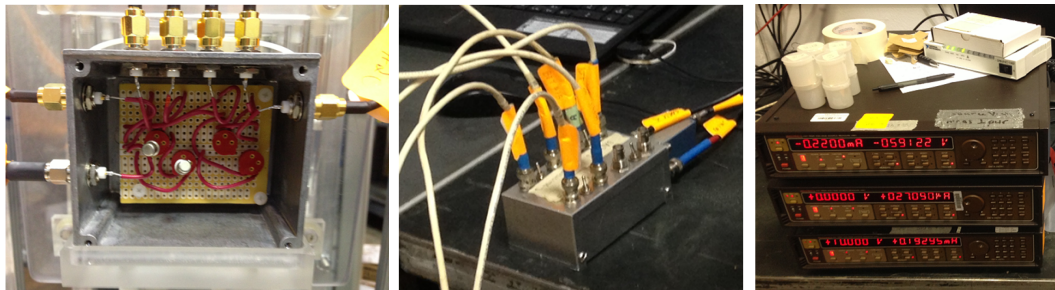


Figure 32. A close-up of the DuT fixture (left), switchbox (middle), and SMUs (right). In the text fixture and switchbox, the aluminum box acted as an EMI shield.

Using the standard DuT mount, the 1-MeV neutron flux at the IU NREF is 2×10^{10} n/cm²/s. A modification was made to increase the flux by using an acrylic jack to reposition the DuT approximately 4-6 cm from the beryllium target. This

modification increased the flux by as much as a factor of 2.5. The jack was supported by a 6 inch tall block of acrylic. This positioned the BJTs along the neutron source center line, maximizing the flux incident on the device by minimizing streaming loss. A picture of this set-up is displayed in Figure 33.



Figure 33. The test set-up inside the TMR included a block of acrylic to position the DuT fixture at the centerline of the beam. The acrylic jack sat atop this block. The aluminum test rig is positioned to the left of the jack and is facility the beryllium target (which is out of sight below and to the left of the set-up).

Test Procedures.

Two types of experiments were accomplished: the Multiple Sequential Interval (MSI) Test and the Single Long Interval (SLI) Test. These two experiments were conducted on the same day with the same beam parameters in order to minimize variations in the neutron flux spectrum.

The gamma-induced photocurrent was mitigated by using a second shunting BJT [12]. Figure 34 displays a schematic of the experimental circuit in the common base

configuration. The shunt BJT was selected to most closely match the DuT gain. The collector of the shunting BJT was connected to the base in the test BJT to ensure that the base-collector junction remained reverse-biased during the irradiation. Because the gamma flux from the NREF is relatively low, especially when compared with a nuclear reactor, its effect was minimal.

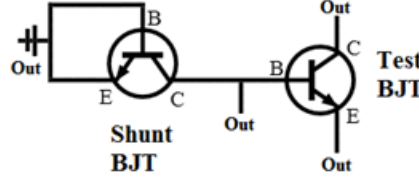


Figure 34. A schematic of the shunt and test BJTs. The BJT being analyzed is in Common Ground configuration.

In the MSI experiment, the beam was set to the parameters found in Table 6. For the initial interval, the device was irradiated until the gain was reduced to 75% of the range between its starting value and 30. Then, the beam was shut off for 30 s of annealing. This was repeated three more times, and the gain was reduced by 25% of the range each time until the gain was 30 after the fourth irradiation interval. Then, the device was allowed to anneal. For example, the BJT pre-irradiation gain was 147.4. The beam was shut down when the device gain was 118, 88.5, 59, and stopped when it reached 30.

Table 6. Beam parameters on the day of experiment.

Beam Parameter	Value
Current [mA]	20
Max. Proton Energy [MeV]	13
Frequency [Hz]	20
Pulse Width [μ s]	400

The SLI experiment followed the MSI experiment. The beam was turned on for a specified interval of time at the same flux, thereby corresponding to a desired total

fluence. The BJT being irradiated was constantly biased with +10 V on the collector, 0 V on the base, and -220 μ A on the emitter. After the desired time was reached, the beam was turned off while measurements of the powered devices continued. After an interval of measuring the device annealing, power from the SMU was turned off and the devices were removed from the TMR vault.

Neutron Dosimetry.

The neutron source energy spectrum has been quantified via Monte Carlo simulations using MCNP-X Version 2.7.0 [13] along with verification using sulfur foil activation analysis.

Table 7. Activation analysis results from sulfur foils.

Irr Time (min.)	$\phi_{measured}$ [$\frac{n}{cm^2 \cdot s}$]	ϕ_{MCNP} [$\frac{n}{cm^2 \cdot s}$]	Ratio	Avg.
30	3.29×10^{10}	3.55×10^{10}	0.927	0.996
	3.78×10^{10}	3.55×10^{10}	1.065	
60	3.26×10^{10}	3.55×10^{10}	0.918	0.948
	3.47×10^{10}	3.55×10^{10}	0.977	
90	3.59×10^{10}	3.55×10^{10}	1.011	0.966
	3.27×10^{10}	3.55×10^{10}	0.921	

Table 7 displays the results of neutron activation analysis completed for the 30, 60, and 90 min irradiations. Sulfur provided good agreement with simulation (within 5%, which is a common factor of systemic uncertainty for neutron activation analysis) so that the simulated neutron energy spectrum can be accepted. Thus, the resulting 1-MeV equivalent (Si) neutron flux for the new position dictated by the acrylic jack was found to be $4.42(\pm 0.22) \times 10^{10}$ n/cm²/s, or about a factor of 2 larger than the reported value of flux for the standard position without the jack.

Results and Analysis.

The MSI experiment raw results are displayed in Figure 35. The SLI experiment raw results are presented in Figure 36.

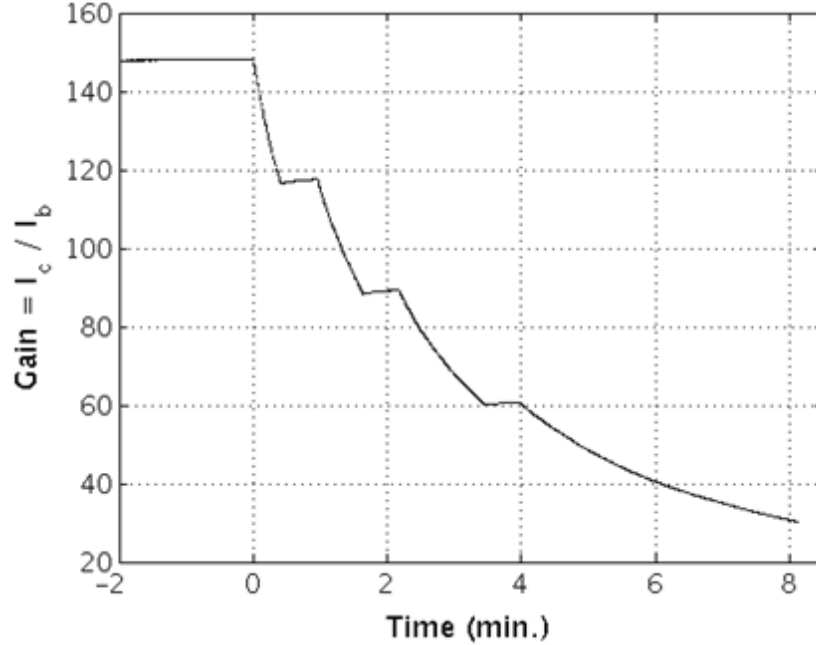


Figure 35. BJT gain as a function of time for the MSI test. The intervals of irradiation and intervals of annealing were fit to the Messenger-Spratt equation and a power function, respectively.

The gain for each interval of irradiation was fit to the Messenger-Spratt equation using the equation,

$$\beta(t) = \frac{1}{\left(\frac{1}{\beta_o}\right) + Dt} \quad (47)$$

where D is the fitting coefficient, which encompasses both the damage constant $K(E)$ and the flux $\phi(E)$. The first three intervals of annealing were 30 s long. Not seen in Figure 35 is the final interval of annealing, which was also 30 s. Annealing was found to follow a power law function as in Equation 48,

$$\beta(t) = At^C + B \quad (48)$$

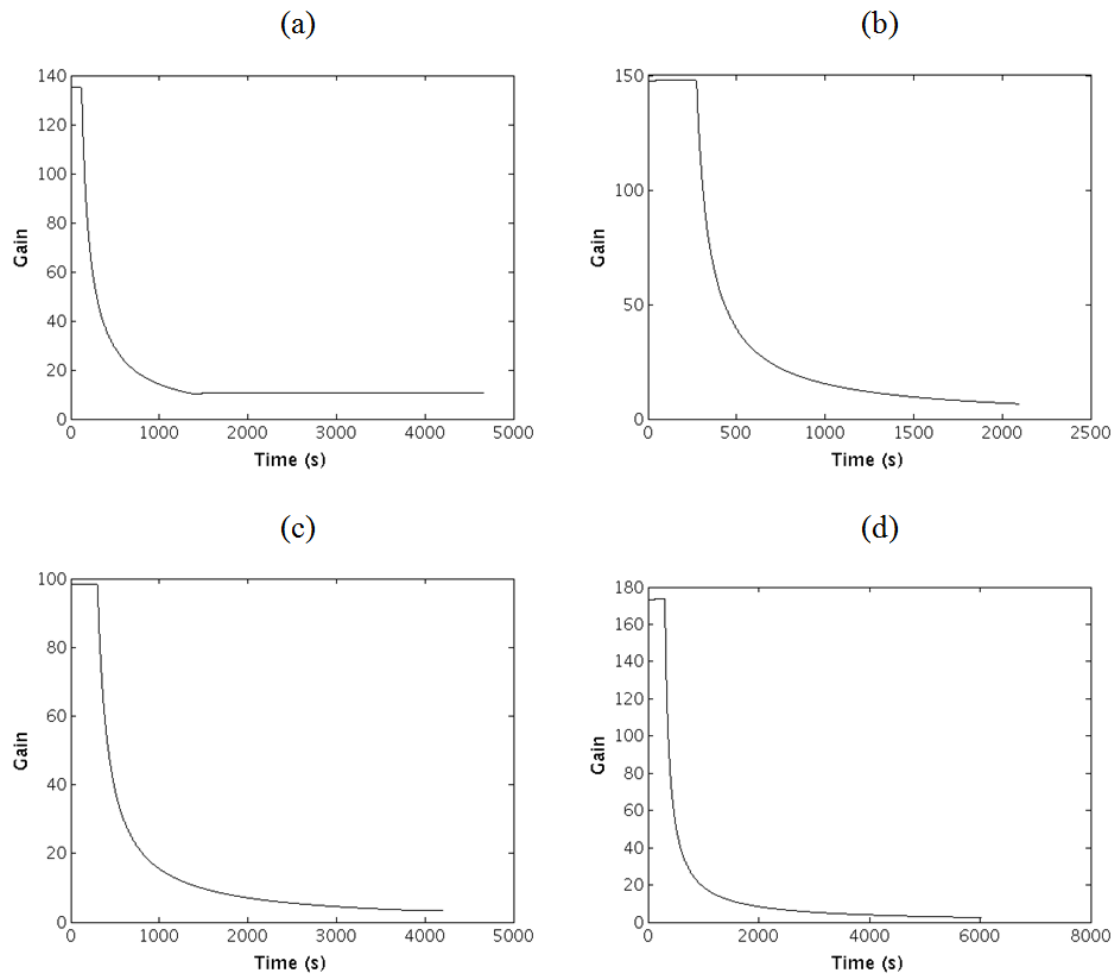


Figure 36. Gain as a function of time for continuous irradiations of (a) 20 min, (b) 30 min, (c) 60 min, and (d) 90 min. Note that in (a) there is a significant annealing time (approximately 60 min), while in the other three cases (b-d) there is only a 5 min annealing measured following irradiation.

where A , B , and C are fitting coefficients. By inspection, B is the device gain at the start of the annealing interval.

After nonlinear regression was accomplished and the coefficients were determined, D provided an estimate of the damage constant, K , and how it compared with the accepted value in literature, $K_{1-MeV} \approx 1.5 \times 10^{-15}$ cm²/n. This information is tabulated in Table 8.

Table 8. Fitting coefficients from gain degradation intervals with extracted damage constant, K .

Int.	D	Std. Err.	K	1-R ²
1st	7.55×10^{-5}	19.6%	1.72×10^{-15}	5.84×10^{-6}
2nd	6.95×10^{-5}	18.3%	1.58×10^{-15}	1.09×10^{-5}
3rd	7.09×10^{-5}	6.6%	1.61×10^{-15}	4.57×10^{-6}
Last	6.70×10^{-5}	2.4%	1.52×10^{-15}	4.65×10^{-6}
20 min	7.31×10^{-5}	0.04%	1.65×10^{-15}	1.65×10^{-4}
30 min	8.30×10^{-5}	0.05%	1.88×10^{-15}	5.09×10^{-4}
60 min	7.87×10^{-5}	0.02%	1.78×10^{-15}	1.56×10^{-4}
90 min	6.81×10^{-5}	0.02%	1.54×10^{-15}	1.60×10^{-4}
Average	7.32×10^{-5}	47.03%	1.66×10^{-15}	1.27×10^{-4}

The same nonlinear regression fitting was accomplished for annealing, however it was fit to a power function as presented in Equation 48. The results of this are displayed in Table 9.

Table 9. Fitting coefficients from annealing intervals.

Interval	A	Err.	B	Err.	C	Err.	1-R ²
First	2.9×10^{-1}	6.7%	116.2	0.022%	0.45	3.3%	4.0×10^{-8}
Second	1.9×10^{-2}	5.8%	88.21	0.018%	0.50	2.7%	3.6×10^{-8}
Third	6.2×10^{-2}	4.1%	60.07	0.008%	0.69	1.5%	1.6×10^{-7}
Final	3.0×10^{-2}	4.7%	30.22	0.008%	0.62	1.9%	8.5×10^{-9}
20 min	2.2×10^{-3}	5.5%	10.33	0.003%	0.79	1.8%	3.4×10^{-9}
60 Min	2.6×10^{-4}	12.0%	3.405	0.002%	0.84	3.8%	2.3×10^{-9}
90 Min	2.8×10^{-4}	10.3%	2.652	0.002%	0.71	3.8%	1.2×10^{-9}

The fitting coefficient B is observed to be the BJT gain at the start of the annealing interval. The A and C coefficients follow a general downward trend as irradiation time

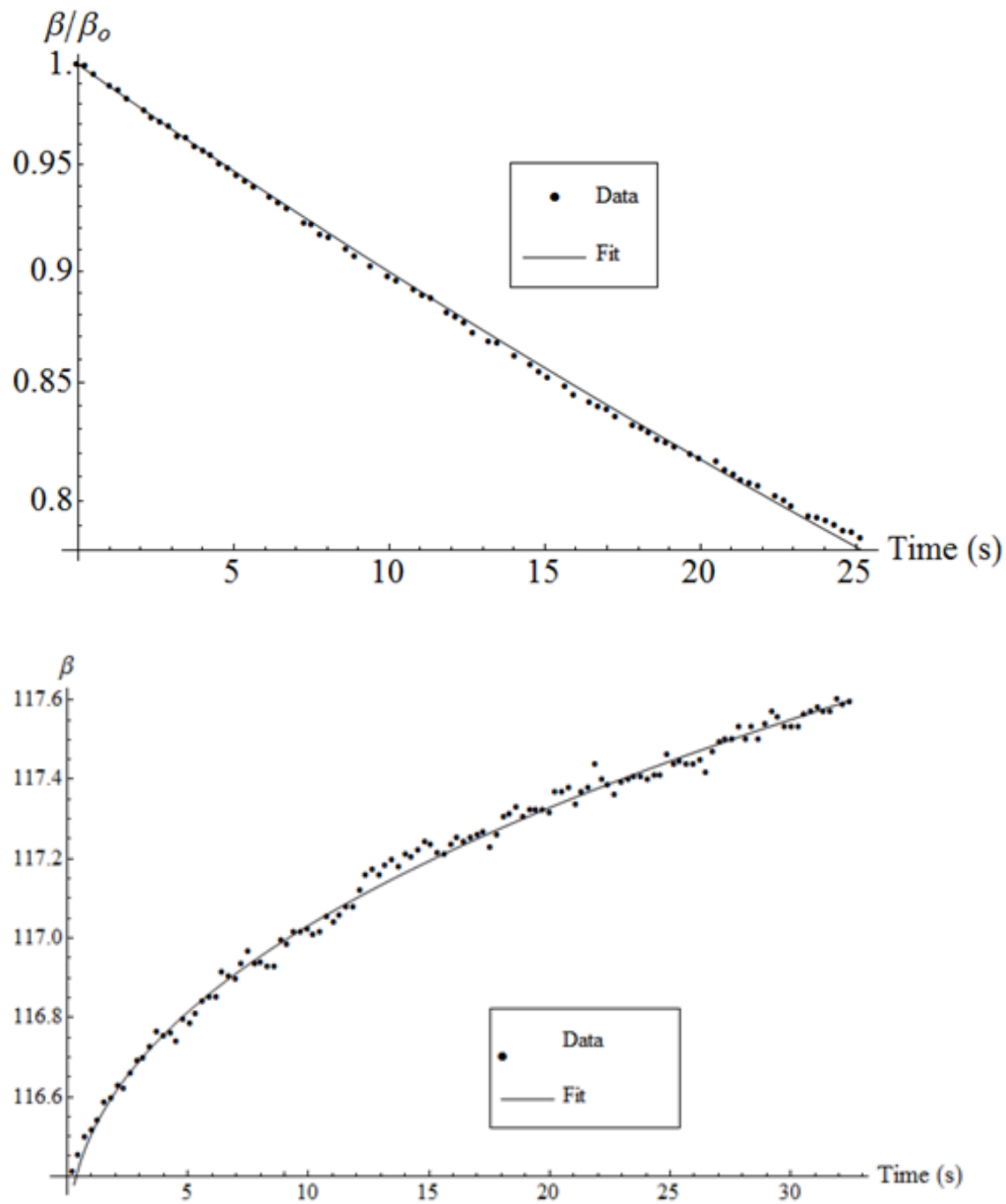


Figure 37. Examples of the curve fitting for both degradation (top) and annealing (bottom). Note that in the top chart, gain was normalized to the precharacterization gain, while on the bottom it has not been normalized.

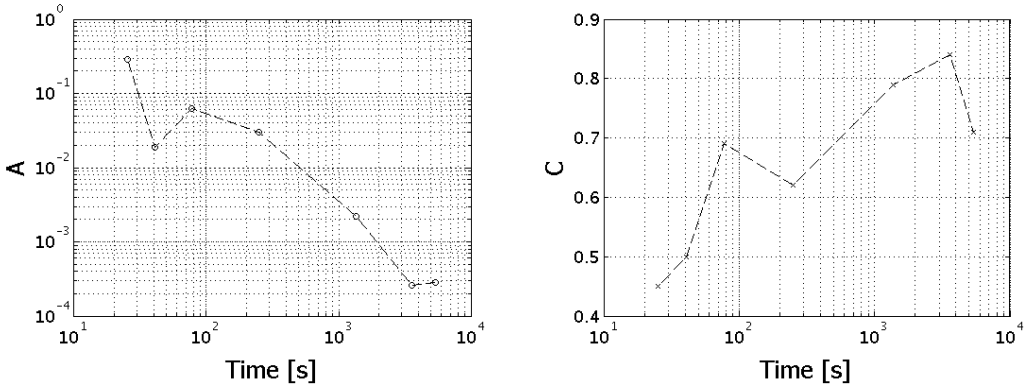


Figure 38. The A and C coefficients are plotted as a function of time. The connecting dotted lines in the figures are just for presentation and analysis.

increases. If it is possible to determine the functionality of A and C with fluence and annealing, it may lead to a better understanding of how to incorporate relaxation into the model. However, this still has not been resolved and requires further investigation. The coefficients are plotted as a function of time in Figure 38.

In Figure 39, a comparison of the change in gain relative to the beginning of the annealing interval is presented as a function of time from the start of the annealing interval for the MSI experiment. In this format, one can see that annealing in the BJT devices occurs faster when the device has been damaged less. This is verification of a prediction by the mathematical model developed in Chapter III.

After removing the devices from the IU NREF vault, three of the irradiated BJTs were placed in a laboratory oven and baked from at 150°C. Afterward, they were removed from the oven and allowed to cool to room temperature. During this entire process, the gain was measured *in-situ* using an HP4145A Semiconductor Parameter Analyzer [14]. The results, after being normalized, are plotted in Figure 40.

Comparison with traditional single-pulse system.

One of the main interests in this research was to compare the NREF neutron source with other neutron sources. One of the best ways to do this is to obtain

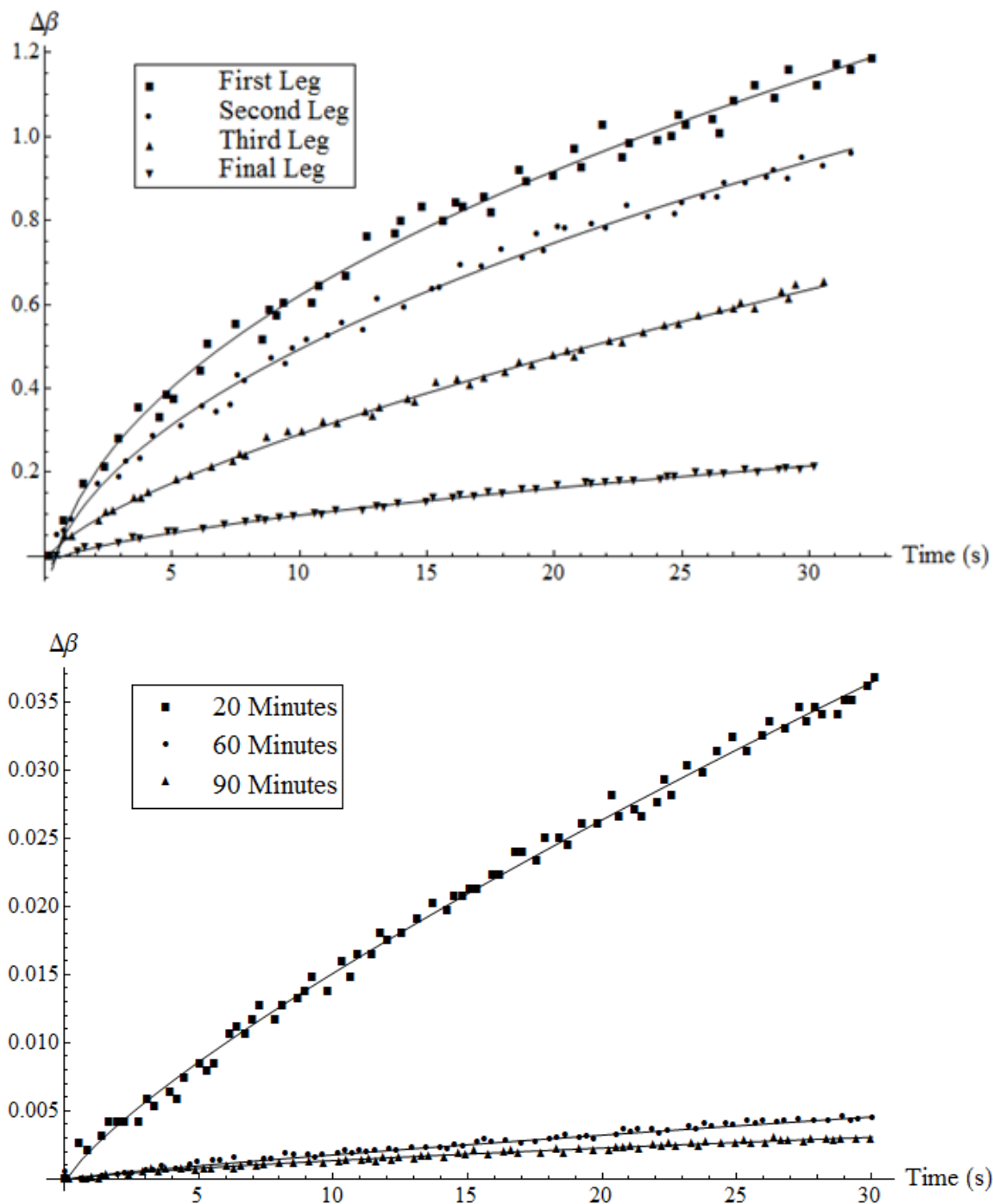


Figure 39. Comparison of the annealing of BJT gain for multiple sequential interval (top) and single long interval (bottom) tests. The y-axis is the change in gain relative to the start of annealing interval.

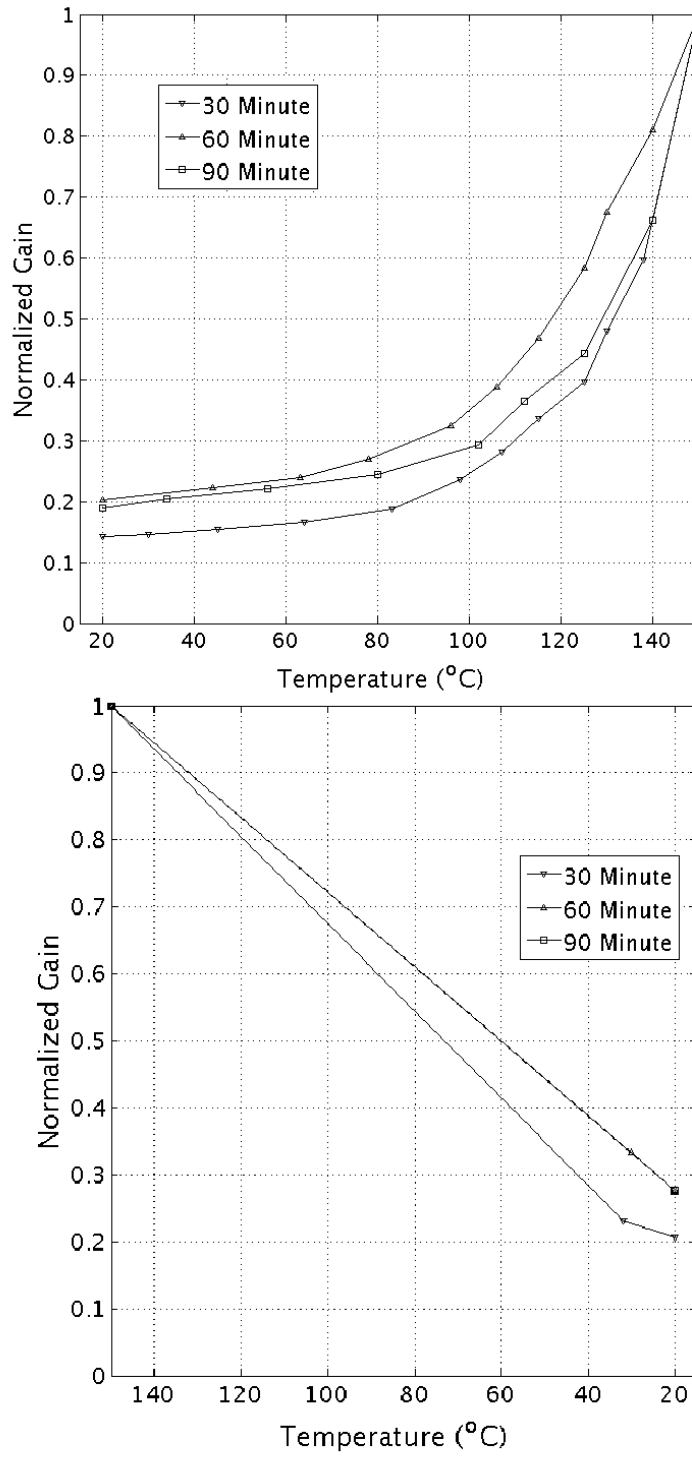


Figure 40. (Top) Gain as a function of temperature during a post-irradiation thermal anneal. Gain was measured *in-situ* while being baked and normalized to the gain at 150°C. (Bottom) Gain as a function of temperature as the devices were allowed to come back to room temperature after the thermal anneal. Gain in both plots has been normalized to the maximum value (at 150°C).

gain degradation data at multiple 1-MeV equivalent (Si) neutron fluences and make a direct comparison of the change in gain, $\Delta(1/\beta)$.

Figure 41 displays a plot that compares data as collected from four widely-used and well characterized single pulse neutron sources [12]. These four systems are the Sandia Pulsed Reactor (SPR-III), White Sands Missile Ranges Fast Burst Reactor (WSMR FBR), the Annular Core Research Reactor (ACRR), and the Los Alamos Neutron Science Center (LANSCe). These four systems are traditional, single pulse, high intensity neutron sources that provide neutrons with a small pulse width. Data from these systems match well with the typically accepted value for the damage constant for 2N2222A BJTs in the Messenger-Spratt Equation, from 1 to 2×10^{-15} cm^2/n .

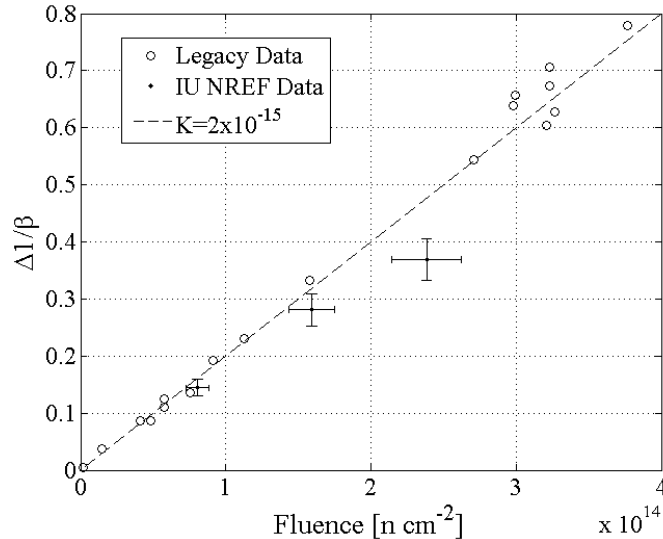


Figure 41. A comparison of gain degradation as a function of fluence for multiple systems. "Legacy data" includes data from SPR-III, WSMR FBR, ACRR, and LANSCe. The dotted line represents the $\Delta(1/\beta)$ using the accepted value of the damage constant, K .

However, when the IU NREF data are plotted along with the legacy data, the device degradation at higher fluences is different due to annealing. In all cases, the NREF data fall below the expected values; thus, the device final gain is higher than

would be expected to correspond to the neutron fluence levels. Unfortunately, each of these IU NREF data points in Figure 41 is a single measurement, and it could just be experimental or systemic error. Therefore, a second set of experiments was planned at IU NREF with more rigor applied and more devices irradiated to get better statistics.

NREF Experiment 2: Expanded Dataset.

The purposes of the second set of experiments at the IU NREF beamline were twofold. First, the second set of experiments employed more rigorous dosimetry, to include additional neutron activation foils as well as thermoluminescent dosimeters (TLD) as prescribed by ASTM standard methods. Second, better statistics were obtained by irradiating more devices, thereby expanding the dataset for analysis.

As was done during the first experimental series at IU NREF, BJTs were irradiated by neutrons and the performance degradation was measured *in-situ*. In the following sections, the equipment used, procedures followed, and results obtained are presented.

Test Equipment.

During irradiation, the BJTs being tested were under constant electrical bias. To accomplish this, three Keithley 237 SMUs were set up inside the vault but outside the TMR. Each BJT leg was connected to an SMU via approximately 10 to 15 ft of BNC cabling. The SMU output was fed to a laptop that was running a custom-built LabView virtual instrument, via General Purpose Interface Bus (GPIB) cables and a National Instruments Ethernet-to-GPIB converter.

As with the first experiment, a custom-built acrylic jack was placed on the TMR positioning platform inside the open-air cavity to properly position the DuT for maximum neutron flux. Additionally, the BJTs being irradiated were contained within a custom-built aluminum enclosure for EMI protection. This enclosure used SMA

through-bulkhead connectors to connect to the measurement equipment positioned outside the TMR, but inside the vault. Also similar to the first experiment, a second BJT was connected to the base leg of the original device in order to shunt the gamma-induced photocurrent.

Test Procedures.

For all irradiations, the BJT for which gain was being measured was under constant bias with +10V on the collector, -220 A on the emitter, and the base was set to SMU ground. The collector and base SMUs were set to source voltage and measure current, while the emitter SMU was set to source current and measure voltage. This configuration ensured that the collector-base junction was reverse-biased, while the emitter-base junction was forward-biased, causing the BJT to be in forward active mode at all times. It is in this mode that BJTs are designed to provide the greatest current gain; this also means that gain sensitivity to changes in the defect species populations is maximized.

For four experiment runs, the IU NREF beamline was switched on with a nominal beam current of 20 mA, a pulse width of 400 s, and a beam repetition rate of 20 Hz. The SMU output from all three legs was collected using a custom-built LabView virtual instrument. After 20 min, the beamline was switched off but the SMU output continued recording for 5-10 min afterward. The purpose of this experiment set was to ensure a consistent, repeatable experiment that complies with community standards, specifically the American Society for Testing and Materials (ASTM) standards such as E265-07(2013) *Standard Test Method for Measuring Reaction Rates and Fast-Neutron Fluences by Radioactivation of Sulfur-32* [15] and E1855-10 *Standard Test Method for Use of 2N2222A Silicon Bipolar Transistors as Neutron Spectrum Sensors and Displacement Damage Monitors* [1].

In a second set of irradiations, devices were exposed to different total neutron fluences, starting with 40 and increasing to 60, 90, and 120 min total irradiation periods. BJTs were irradiated and the gain degradation measured *in-situ* before, during, and after irradiation. Because the beam capacitor faulted down during the first 40 min irradiation, an additional irradiation period of 4 min was added to the experiment. The neutron flux from the first set of experiments at the IU NREF was 4.4×10^{10} n/cm²/s when the DuT was approximately 4-6 cm from the beryllium target, which corresponds to fluences of 0.96, 1.44, 2.16, and 2.88×10^{14} n/cm²/s.

The IU NREF beamline operational parameters for this experiment was a nominal beam current of 20 mA, a pulse width of 400 s, and a beam repetition rate of 20 Hz.

The SMU output from all three legs was collected using the same custom-built LabView program. After the specified time, the beamline was switched off but the SMU output continued recording for 5-10 min afterward. The purpose of this experiment set was to verify the data points on Figure 41 and fill in additional fluence values to better understand the IU NREF damage coefficient.

Neutron Dosimetry.

The first set of 4 BJTs was irradiated for 20 min each. One S pellet, one Fe foil, and one TLD were positioned within 6 cm of the BJT being irradiated to determine the neutron and gamma doses incident on the BJTs. Before irradiation, the mass of the S pellets and Fe foils used in neutron activation analysis were measured using a standard digital laboratory scale.

This information is tabulated in column 3 of Table 10 and Table 11. The average S mass was 0.590 ± 0.01 g while the average Fe mass was 0.303 ± 0.003 g. This information was then used to calculate the atomic number density of the relevant isotopes (³²S for the sulfur pellets and ⁵⁴Fe and ⁵⁶Fe for the iron foils). Number

density, N_x , is where ρ_x is the density of the x^{th} isotope, N_{Av} is Avagadros number at 6.022×10^{23} at/mol, and M_x is the atomic mass of the x^{th} isotope. The atomic mass of S and Fe are assumed to be 32.065 ± 0.005 g/mol and 55.845 ± 0.002 g/mol, respectively.

Table 10. Iron foil mass measurement.

#	Mass (g)	+/-	N_{Fe-54}	+/-	N_{Fe-56}	+/-
1	0.2998	0.0001	1.89×10^{20}	8.60×10^{16}	2.97×10^{21}	1.26×10^{18}
2	0.3062		1.93×10^{20}	8.65×10^{16}	3.03×10^{21}	1.26×10^{18}
3	0.3036		1.91×10^{20}	8.63×10^{16}	3.00×10^{21}	1.26×10^{18}
4	0.3002		1.89×10^{20}	8.60×10^{16}	2.97×10^{21}	1.26×10^{18}

Table 11. Sulfur pellet mass measurement.

#	Mass (g)	+/-	N_{S-32}	+/-
1	0.5913	0.0001	1.05×10^{22}	3.98×10^{18}
2	0.599		1.07×10^{22}	4.01×10^{18}
3	0.5972		1.07×10^{22}	4.01×10^{18}
4	0.574		1.02×10^{22}	3.92×10^{18}

The Fe foil is used to best measure the epithermal region of a neutron spectrum, that is the region between thermal (<0.25 eV) and fast (>1 MeV) neutron energies. There are two main reactions of interest in Fe foils in the spectrum at the IU NREF, which are described in the following list along with some of the pertinent information about these reactions:

1. $^{54}Fe(n,p)^{54}Mn$ - There is a low percentage of ^{54}Fe atoms in each iron sample, and the 834.8 keV gamma ray can be difficult to differentiate from gamma emitted by ^{56}Mn .
2. $^{56}Fe(n,p)^{56}Mn$ - This isotope of manganese has two dominant gamma rays at 846.8 keV and 1810.7 keV. The second (photopeak) is easily identified and used in calculation of the radioactivity.

Table 12. Gamma peak information for the iron foils.

#	E_{peak}	σE_{peak}	I_γ Frac.	σI_γ	Peak Area	PA ±
1	834.838	0.003	0.9998	0.001	1.49×10^3	38.71
	846.7638	0.0019	0.989	0.3	3.03×10^3	54.32
	1811	0.004	0.287	0.8	3.57×10^2	22.66
2	834.838	0.003	0.9998	0.001	1.41×10^3	38.57
	846.7638	0.0019	0.989	0.3	3.75×10^3	60.48
	1811	0.004	0.287	0.8	4.15×10^2	24.08
3	834.838	0.003	0.9998	0.001	1.37×10^3	37.78
	846.7638	0.0019	0.989	0.3	3.65×10^3	59.8
	1811	0.004	0.287	0.8	4.18×10^3	23.04
4	834.838	0.003	0.9998	0.001	9.85×10^2	32.37
	846.7638	0.0019	0.989	0.3	2.82×10^3	52.68
	1811	0.004	0.287	0.8	3.28×10^2	21.79

The use of Fe foils as a neutron activation analysis dosimeter is delineated by the ASTM Standard E263-13, *Standard Test Method for Measuring Fast-Neutron Reaction Rates by Radioactivation of Iron* [16]. To calculate and correct for the activity at infinite irradiation time, the total counts under the peak is used in Equation 49:

$$A_\infty = \frac{\lambda(C - B) \exp\{\lambda t_w\}}{\epsilon [1 - \exp\{-\lambda t_i\}] [1 - \exp\{-\lambda t_c\}]}, \quad (49)$$

where γ is the isotopic decay constant; C and B are the measured counts under the peak and background counts in the detector, respectively; t_i , t_w , and t_c are the irradiation, waiting, and counting times, respectively; and ϵ is the detector efficiency factor. Figure 42 displays a visual description of the respective times for Equation 49. The tabulated results of this analysis are displayed in Table 13.

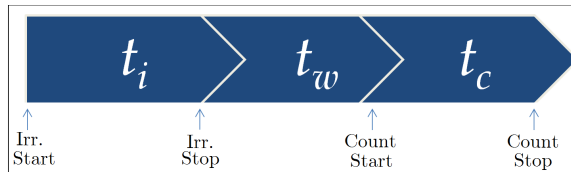


Figure 42. Timeline representing irradiation, waiting, and counting times for neutron activation analysis.

Table 13. Calculation of measured 1-MeV Equivalent (Si) neutron flux using iron foils.

#	E _{peak} [keV]	C $\frac{C}{\varepsilon}$	A _∞ [dps]	N _{isotope} [cm ⁻³]	$\frac{A_{\infty}}{N_{isotope}}$	ϕ_{eff} [cm ⁻² s ⁻¹]
1	835	1.85×10^5	1.67×10^6	1.89×10^{20}	8.85×10^{-15}	6.00×10^{10}
	847	3.89×10^5	1.01×10^6	2.97×10^{21}	3.40×10^{-16}	2.31×10^9
	1811	4.03×10^5	1.05×10^6	2.97×10^{21}	3.52×10^{-16}	2.39×10^9
2	835	1.75×10^5	1.51×10^6	1.93×10^{20}	7.81×10^{-15}	5.29×10^{10}
	847	4.82×10^5	9.26×10^5	3.03×10^{21}	3.06×10^{-16}	2.07×10^9
	1811	4.69×10^5	9.01×10^5	3.03×10^{21}	2.97×10^{-16}	2.02×10^9
3	835	1.70×10^5	1.54×10^6	1.91×10^{20}	8.03×10^{-15}	5.45×10^{10}
	847	4.69×10^5	9.84×10^5	3.00×10^{21}	3.28×10^{-16}	2.22×10^9
	1811	4.72×10^5	9.91×10^5	3.00×10^{21}	3.30×10^{-16}	2.24×10^9
4	835	1.22×10^5	1.10×10^6	1.89×10^{20}	5.82×10^{-15}	3.95×10^{10}
	847	3.62×10^5	6.60×10^5	2.97×10^{21}	2.22×10^{-16}	1.51×10^9
	1811	3.70×10^5	6.75×10^5	2.97×10^{21}	2.27×10^{-16}	1.54×10^9

To determine the effective flux, ϕ_{eff} , the activity calculated in Equation 49 was used via Equation 50.

$$A_{\infty} = N_{isotope} \sigma_{isotope}^{avg} \phi_{eff}. \quad (50)$$

In Equation 50, $N_{isotope}$ is the number density of the parent isotope and $\sigma_{isotope}^{avg}$ is the spectrum-averaged microscopic cross section of the reaction of interest in the parent isotope that creates the radioactive daughter. The spectrum-averaged cross section is defined as

$$\sigma_{isotope}^{avg} = \frac{\int_E^{\infty} \sigma(E') \phi(E') dE'}{\int_E^{\infty} \phi(E') dE'}, \quad (51)$$

where $\sigma(E')$ is the energy-dependent cross-section and $\phi(E')$ is the energy-dependent neutron spectrum determined using MCNP. From MCNP calculations, the expected spectrum-averaged cross section for Fe is 1.47×10^{-25} cm² or 0.147 b.

The S pellet was used to measure the fast region of a neutron spectrum. There is one reaction of interest in S pellets, which is the (*n,p*) inelastic collision resulting in radioactive ³²P. This phosphorus isotope decays by beta emission with a maximum energy of 1709 keV. At IU, the induced activity in the S pellets after irradiation was

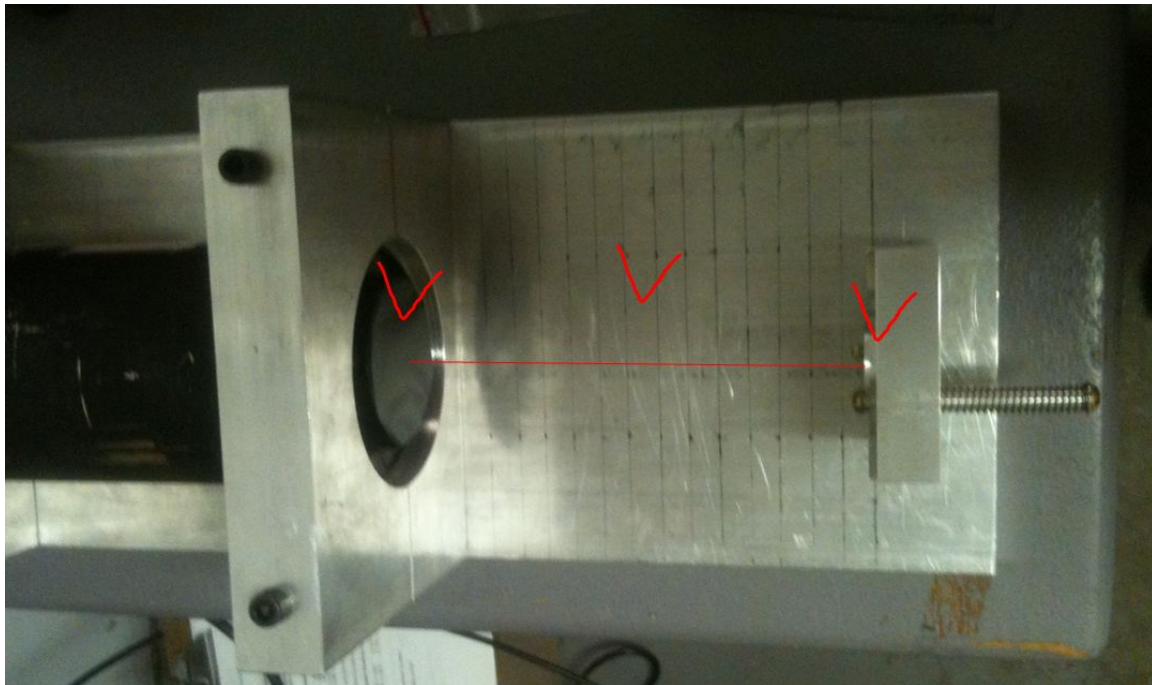


Figure 43. Beta organic scintillation counter at IU (left arrow) for measurement of beta decay products from phosphorus daughter; S pellet was placed in an aluminum holding fixture (right arrow) 14 cm from the detector.

measured using a scintillation detector (displayed in the left portion of Figure 43). Before measuring the irradiated S, a series of four 5-min background measurements was made to determine an average background count, which is tabulated in Table 14. The average 5-min background measurement was $2478 (\pm 50)$ counts.

Table 14. Sulfur pellet background measurement for 5 minute counting intervals; note that Cps = counts per second.

#	Counts	Avg Counts	Counts \pm	Cps	Avg Cps	Avg Cps \pm
b.1	2716	2477.5	49.77	9.05	8.26	0.55
b.2	2381			7.94		
b.3	2457			8.19		
b.4	2356			7.85		

Additionally, a 104 year half-life, standardized ^{32}Si source was used to calibrate detector efficiency. This source was produced by Eckert & Ziegler and is NIST-traceable. The standard source was placed in the apparatus and counted for 5 min.

Total beta counting efficiency was then calculated as,

$$\begin{aligned}\varepsilon_{beta} &= SS \cdot \varepsilon_{det}, \\ &= SS \cdot \left(\frac{C_{std_src} - B}{\xi \cdot A_{source}} \right),\end{aligned}\tag{52}$$

where SS is the self-shielding factor; ε_{det} is the detector efficiency; C_{std_src} and B are the standard source and background counts, respectively; ξ is a geometric correction factor accounting for solid angle of the standard source versus the irradiated S pellet samples; and A_{source} is the activity of the standard source in units of decays/min.

The self-shielding factor corrects for betas emitted from within the S pellet that must travel through the S before being emitted from the pellet. A percentage of the betas are captured by the pellet as they travel, reducing the measured value of radioactivity. By including this self-shielding factor, which is always ≤ 1 , we can correct for this reduction. From literature and by using MCNP, the best value of SS for sulfur is 0.88, which was subsequently used in this dosimetry analysis.

The geometric factor ξ corrects for the difference between the calculation of efficiency in the standard source and the calculation of efficiency in the S pellet source. In the calculation of geometric detector efficiency, the correction factor is $\varepsilon_{det} = \frac{C-B}{A_{source}}$ if the standard source has the same physical dimensions as the S pellet. This is equivalent to saying that $\xi = 1$. In the case of this experiment, this is not true, so the geometric factor ξ must be added in the denominator. To calculate solid angle, Ω , for a detector with radius a at a distance d from a source of radius s , Equation Set 53 was used.

$$\begin{aligned}
\Omega &= 1 - \frac{1}{(1+\beta)^{1/2}} - \frac{3\alpha\beta}{8(1+\beta)^{5/2}} - \alpha^2 f_1 - \alpha^3 f_2 \\
\alpha &= \left(\frac{s}{d}\right)^2 \quad \beta = \left(\frac{a}{d}\right)^2 \\
f_1 &= \frac{5\beta}{16(1+\beta)^{7/2}} - \frac{35\beta^2}{16(1+\beta)^{9/2}} \\
f_2 &= \frac{35\beta}{128(1+\beta)^{9/2}} - \frac{315\beta^2}{256(1+\beta)^{11/2}} - \frac{1155\beta^3}{1024(1+\beta)^{13/2}}
\end{aligned} \tag{53}$$

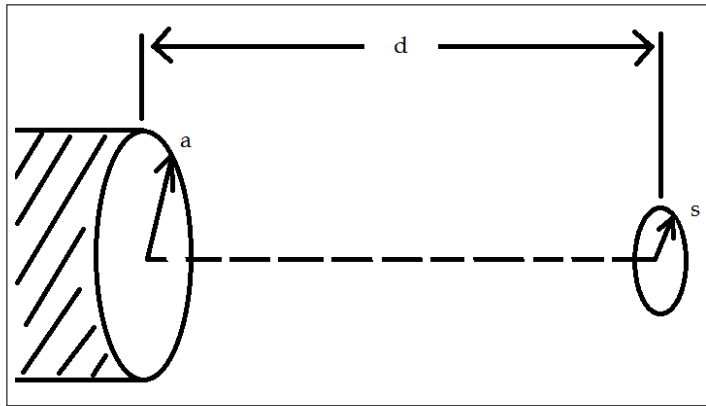


Figure 44. Schematic showing variables involved in calculating solid angle for a source of beta particles with radius, s , a distance, d , away from a detector with radius, a . The geometric factor, ξ , is dependent on the solid angle.

The geometric factor is thus the ratio of solid angle for the standard source Ω_{std_src} to the solid angle for the irradiated S pellet sample Ω_{irr_sample} or $\xi = \frac{\Omega_{std_src}}{\Omega_{irr_sample}}$. The detector face radius is $a = 3$ cm, the distance from the beta source is $d = 14$ cm, the standard source radius is $s_{std_src} = 1.02$ cm, and the S pellet sample radius is $s_{sam} = 0.64$ cm. Therefore, the geometric factor is $\xi = 0.998$. Therefore, since the average background counts are 2478, the calculated detector efficiency is found as

$$\varepsilon_{det} = \left(\frac{1783.5 - 495.5}{0.99773 \cdot 63180} \right) = \frac{1288.0}{63037} = 2.04 \times 10^{-2}. \tag{54}$$

This leads to a total system efficiency of

$$\varepsilon_{beta} = 0.88 \cdot 2.204 \times 10^{-2} = 1.940 \times 10^{-2}. \quad (55)$$

Each irradiated S pellet was measured for four 5-min counting intervals. The activity was corrected to infinite irradiation time using Equation 49. The results are tabulated in Table 15. The effective flux was determined as $\phi_{avg} = A_\infty [N_{isotope} \sigma_{isotope}^{avg}]^{-1}$. The spectrum-averaged cross section for S is $1.23 \times 10^{-25} \text{ cm}^2$ or 0.123 b.

Table 15. Calculation of measured 1-MeV Equivalent (Si) neutron flux using sulfur pellets.

ID#	$\frac{C - B}{\varepsilon_\beta}$	A_∞ [dps]	$N_{isotope}$ $[cm^{-3}]$	$\frac{A_\infty}{N_{isotope}}$	ϕ_{eff} $[cm^{-2}s^{-1}]$
1.1	5.041×10^5	2.625×10^6	1.054×10^{22}	2.490×10^{-16}	2.023×10^9
1.2	4.973×10^5	2.590×10^6	1.054×10^{22}	2.456×10^{-16}	1.996×10^9
1.3	4.976×10^5	2.593×10^6	1.054×10^{22}	2.459×10^{-16}	1.998×10^9
1.4	4.889×10^5	2.548×10^6	1.054×10^{22}	2.416×10^{-16}	1.963×10^9
2.1	6.476×10^5	3.201×10^6	1.068×10^{22}	2.998×10^{-16}	2.436×10^9
2.2	6.419×10^5	3.174×10^6	1.068×10^{22}	2.972×10^{-16}	2.415×10^9
2.3	6.495×10^5	3.213×10^6	1.068×10^{22}	3.008×10^{-16}	2.444×10^9
2.4	6.321×10^5	3.127×10^6	1.068×10^{22}	2.928×10^{-16}	2.379×10^9
3.1	5.836×10^5	3.026×10^6	1.065×10^{22}	2.842×10^{-16}	2.309×10^9
3.2	5.852×10^5	3.035×10^6	1.065×10^{22}	2.851×10^{-16}	2.316×10^9
3.3	5.753×10^5	2.985×10^6	1.065×10^{22}	2.803×10^{-16}	2.277×10^9
3.4	5.908×10^5	3.065×10^6	1.065×10^{22}	2.879×10^{-16}	2.339×10^9
4.1	5.005×10^5	2.577×10^6	1.023×10^{22}	2.518×10^{-16}	2.046×10^9
4.2	5.092×10^5	2.623×10^6	1.023×10^{22}	2.563×10^{-16}	2.082×10^9
4.3	5.044×10^5	2.599×10^6	1.023×10^{22}	2.539×10^{-16}	2.063×10^9
4.4	5.040×10^5	2.597×10^6	1.023×10^{22}	2.538×10^{-16}	2.062×10^9

The results displayed in Tables 13 and 15 show a wide spread of results for the effective flux. However, one must remember that this is not an absolute measure of the neutron flux, but a relative measure of the flux *that the Fe isotope can respond to based on their cross section*.

A more intuitive measure of the dosimetry methodology would be to compare

the measured activity at infinite irradiation as calculated in Equation 49 with the expected activity at infinite irradiation as calculated using the Monte Carlo derived spectrum. This is done using Equation 56 by,

$$A_{\infty} = N_{isotope} \int_{E_{min}}^{E_{max}} \sigma_{isotope}^{rxn}(E) \phi(E) dE. \quad (56)$$

In Equation 56, $N_{isotope}$ is the number density of parent isotopes in the dosimeter in cm^{-3} and $\sigma_{isotope}^{rxn}(E)$ is the energy-dependent cross section for the reaction that creates the radioactive daughter product. Using the spectrum in Figure 31 and cross sections for the three reactions of interest as described in Section 4.1, a comparison can be made and the expected neutron flux can be verified. The three cross sections are plotted in Figure 45. Note that the units of the y-axis in all three plots are mb or 10^{-27} cm^2 , meaning that the cross sections remain very small, even at their peak value.

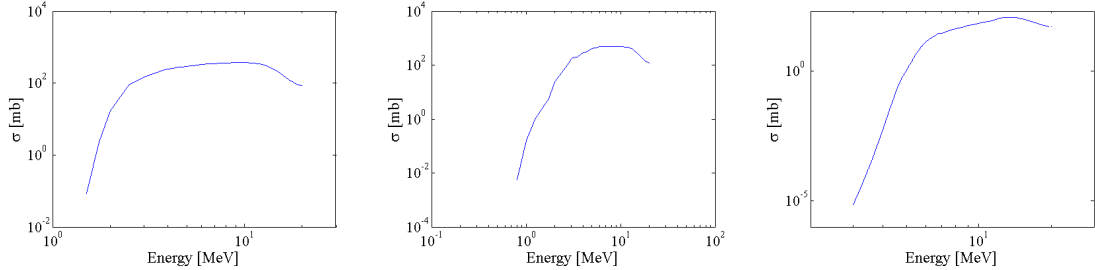


Figure 45. Cross sections for neutron capture by (left) ^{32}S , (middle) ^{54}Fe , and (right) ^{56}Fe . Note that the units of the y-axis are in mb.

In Figure 46, the measured activities at infinite irradiation for all 4 dosimetric irradiations are plotted along with the calculated activity for various levels of 1-MeV equivalent (Si) neutron fluence. The dashed line signifies the expected value for neutron fluence for the IU NREF spectrum, which is $4.96 \times 10^{10} \text{ n/cm}^2/\text{s}$. The Fe foils agree well, within experimental error.

The flux, as determined using S pellets, does not fit the other measurements. Un-

fortunately, the beta detection system used for this measurement included a number of uncertainties for which approximations were made. First, there was no accounting for absorption in the detector window, meaning the result would be skewed to under calculate the true flux. Second, when calculating the geometric factor used to correct for the difference between the standard calibrating source and the unknown S pellet sample, the radius of the calibrating source disk was used. Most likely, however, the beta source itself was a very small radius sample positioned somewhere on the disk. Because of these assumptions, the efficiency was calculated to be larger than it actually was, and therefore the S pellet measurements again under calculated the true flux. Using only the Fe foils, the 1-MeV equivalent (Si) neutron flux is found to be 4.96×10^{10} n/cm²/s for these experiments.

For each of the four 20-min dosimetry-focused irradiations, a TLD crystal was included in the dosimetry package placed next to the BJTs. This TLD was then kept in a light-tight package while it was sent to the Naval Surface Warfare Center (Crane Detachment) for gamma flux determination. The average gamma dose was found to be $(5.3 \pm 1.3) \times 10^3$ rad(Si). From Monte Carlo calculations, the TLD response expected based on the calculated gamma spectrum is 4.75×10^3 rad(Si). One reason the measured TLD response would be higher than the calculated value may be due to neutron-induced electron excitation that is not taken into account in the simulated value, so having a higher average gamma fluence is not unexpected.

Results and Analysis.

For the four dosimetric irradiations of 20 min each, BJT current gain was measured as a function of time using the Keithley SMUs. Using the calculated neutron flux, a plot of the $\Delta(1/\beta)$ is displayed in Figure 47. The 1-MeV equivalent (Si) fluence is calculated using ASTM Standard E722-09e1, *Standard Practice for Characterizing*

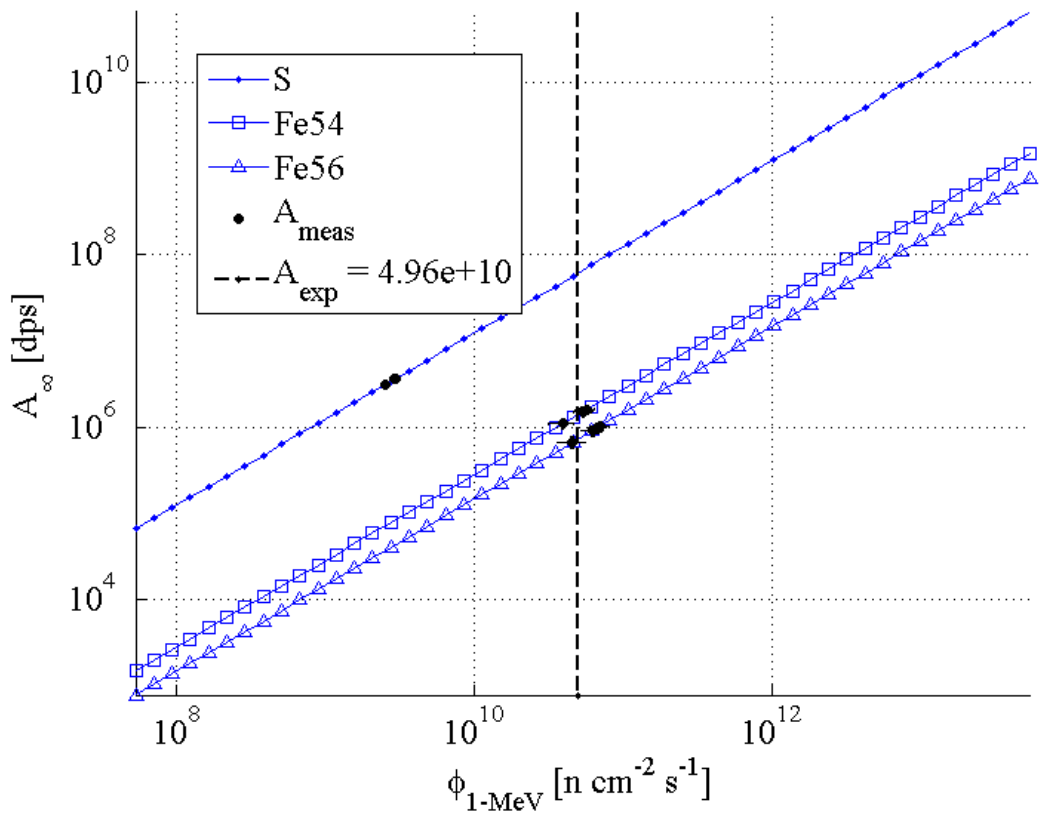


Figure 46. A comparison of the measured and expected activity at infinite irradiation time for the IU NREF neutron spectrum provides good agreement for the Fe foils for $4.96 \times 10^{10} \text{ n/cm}^2/\text{s}$ while the S pellet does not agree.

Neutron Fluence Spectra in Terms of an Equivalent Monoenergetic Neutron Fluence for Radiation-Hardness Testing of Electronics. The Messenger-Spratt equation states that the performance degradation of a semiconductor transistor when subjected to displacement damage such as that from neutrons is governed by a linear response as described by Equation 12.

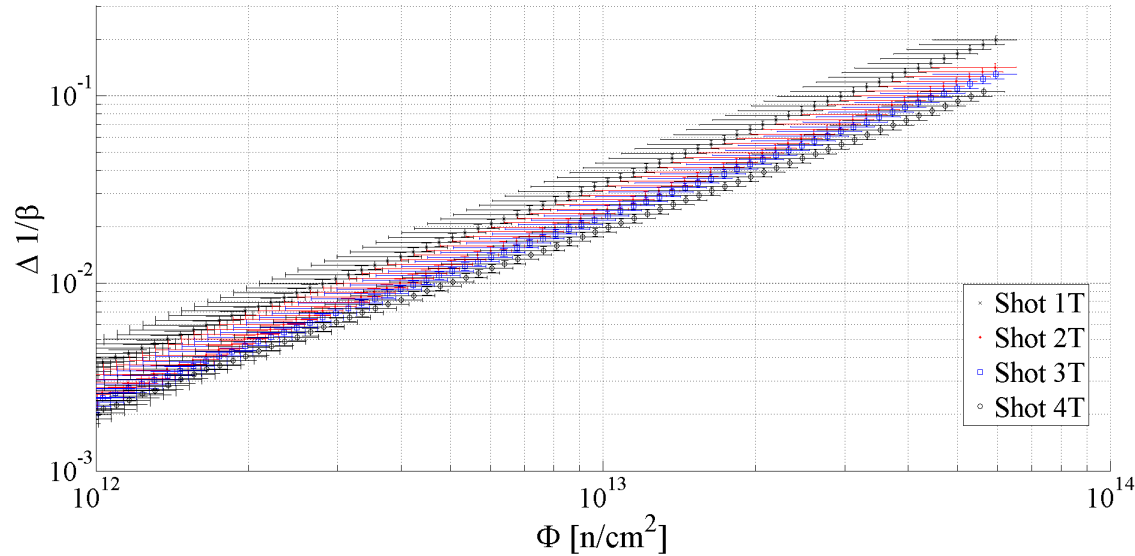


Figure 47. The $\Delta(1/\beta)$ with fluence for the 4 dosimetric shots with error corresponding to beam current uncertainty in the x-direction and equipment error in the y-direction. The average slope was $3.06(\pm 0.55) \times 10^{-15} \text{ cm}^2/\text{n}$.

The response of the BJT under irradiation is linear within experimental error and uncertainty with an average slope of $3.06(\pm 0.55) \times 10^{-15} \text{ cm}^2/\text{n}$. This is greater than the slope in the ASTM Standard E1855 [1], however these devices have not been baked at 80°C for the standard-prescribed 2 hour time interval.

The second set of irradiations in this experimental series investigated effects of time and variations to total neutron fluence. Figure 48 displays the $\Delta(1/\beta)$ with fluence for three of the five variable fluence irradiation intervals, which have an average slope of $3.43 \times 10^{-15} \text{ cm}^2/\text{n}$. Unfortunately, the beam current was not constant from irradiation to irradiation so that the total fluence-to-time varied, causing the slope to fluctuate. Additionally, the beam current varied in the middle of the 5th and

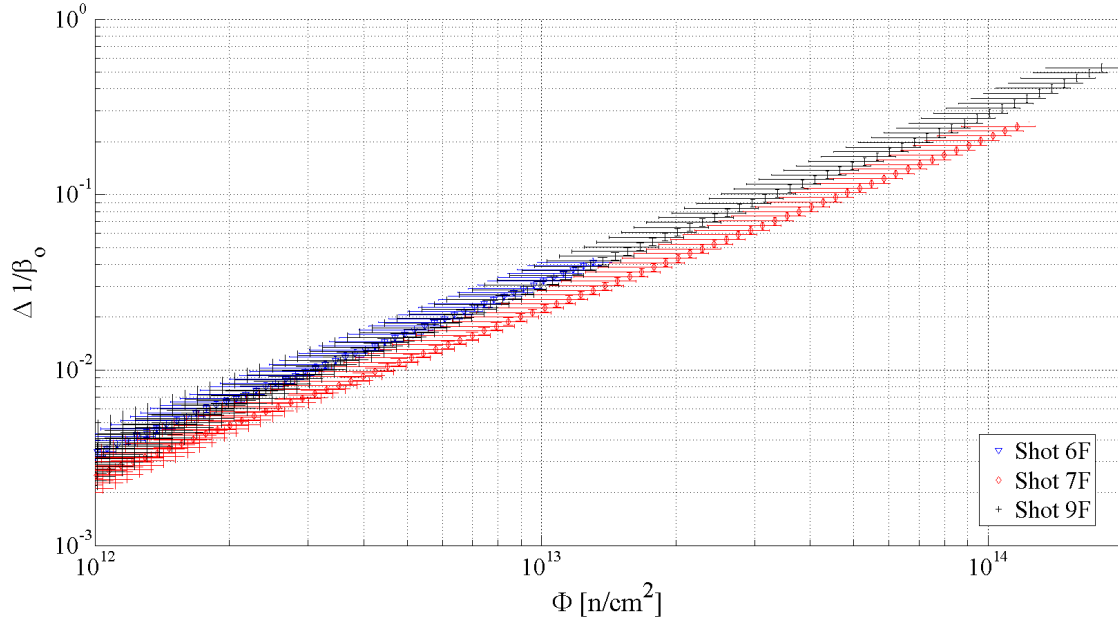


Figure 48. The $\Delta(1/\beta)$ with fluence for three of the five variable fluence shots with error corresponding to beam current uncertainty in the x-direction and equipment error in the y-direction. Shots 5 and 8 were removed because the beam current fluctuated during the shot.

8th irradiations, so they were removed from Figure 48 and presented separately in Figure 50. Irradiation 6F was for four min of total irradiation time, as the proton beam capacitor bank tripped the safety breaker, automatically shutting the beamline down. Irradiations 7F and 9F were for 40 and 60 min, respectively.

To correct for the variation in the beam proton flux from shot-to-shot, a scaling factor was sought using the beam monitor log displayed in Figure 49. The beam current for each irradiation was integrated over the time interval of that irradiation to get a total proton current. Since the y-axis in Figure 49(a) is relative, absolute calculation of the total current is not possible. However, comparison from one irradiation to the next is possible by calculating the ratio. Shot 1T was selected as the normalizing irradiation, and the results of this calculation are also displayed in Figure 49(b). Table 16 displays the time intervals as well as the expected and actual beam current ratios, defined as $R = I_n/I_{1T}$, for each shot. It is these values that are

used to scale the expected flux.

Table 16. Fitting coefficients from gain degradation intervals with extracted flux, ϕ .

Shot	t_{irr} [min]	Exp. Ratio	Act. Ratio	Diff	I/t
1T	20	1	1	—	2.343
2T	20	1	0.98	-2%	2.304
3T	20	1	0.95	-5%	2.301
4T	20	1	1.04	4%	2.38
5F	120	6	6.73	12%	2.664
6F	4	0.2	0.17	-15%	1.883
7F	40	2	2.25	13%	2.451
8F	90	4.5	5.15	14%	2.687
9F	60	3	3.19	6%	2.514

From Figure 49(b), most irradiation intervals have a relatively constant beam current during the entire interval. However, in irradiations 5F and 8F, the proton source jumped between two average current levels during irradiation of the BJTs. These two irradiations are displayed in Figure 50. They are broken down into intervals, three for 5F and four for 8F, corresponding to the periods in which the beam was in a low or high current state. A linear regression was performed on the three intervals in irradiation 5F and the four intervals in irradiation 8F; the overall damage constant was $2.94(\pm 0.35)$ and $2.810(\pm 0.39) \times 10^{-15} \text{ cm}^2/\text{n}$, respectively. In choosing the change in the “average flux”, the ratios determined from Figure 49 and tabulated in Table 16 were used. This analysis assumes that neutron flux is approximately proportional to beam current incident on the beryllium target. A scaling factor, SF , was determined by comparing the average values for each interval against the normalizing average value selected as the first dosimetric irradiation, 1T.

The results for the damage constant calculated using gain data for each irradiation are tabulated in Table 17. Overall, the average value of K is $3.17(\pm 0.40) \times 10^{-15} \text{ cm}^2/\text{n}$. This is higher than the value quoted by the ASTM standard by a factor of approximately 2, however these devices have not been annealed in the 80°C oven.

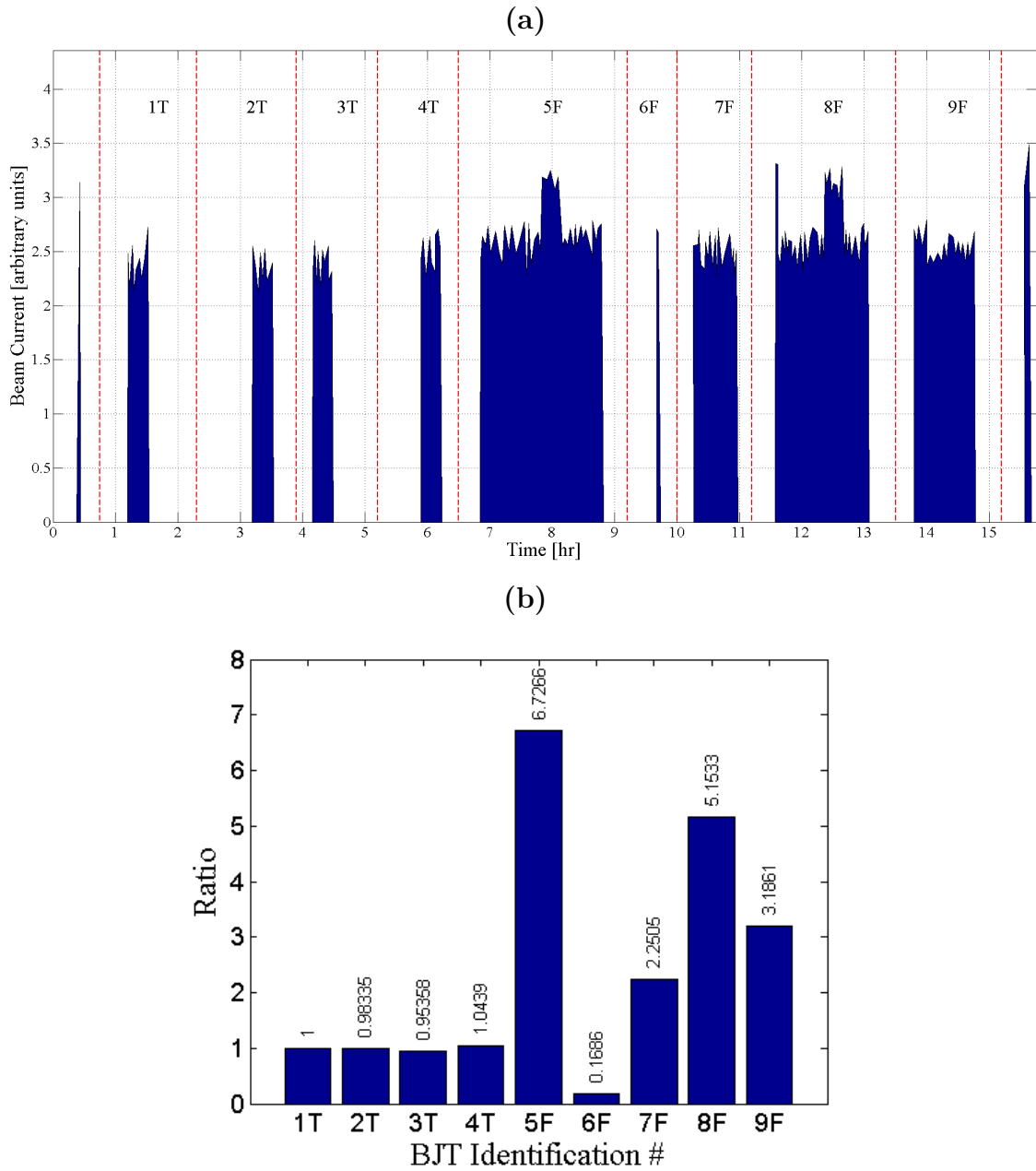


Figure 49. (a) IU NREF beam current as a function of time for the experiment. (b) The proton beam current was not constant throughout the experimental series, and an example of proof of this is that the beam current ratio of 5F, which should be 6.0, is 12% higher.

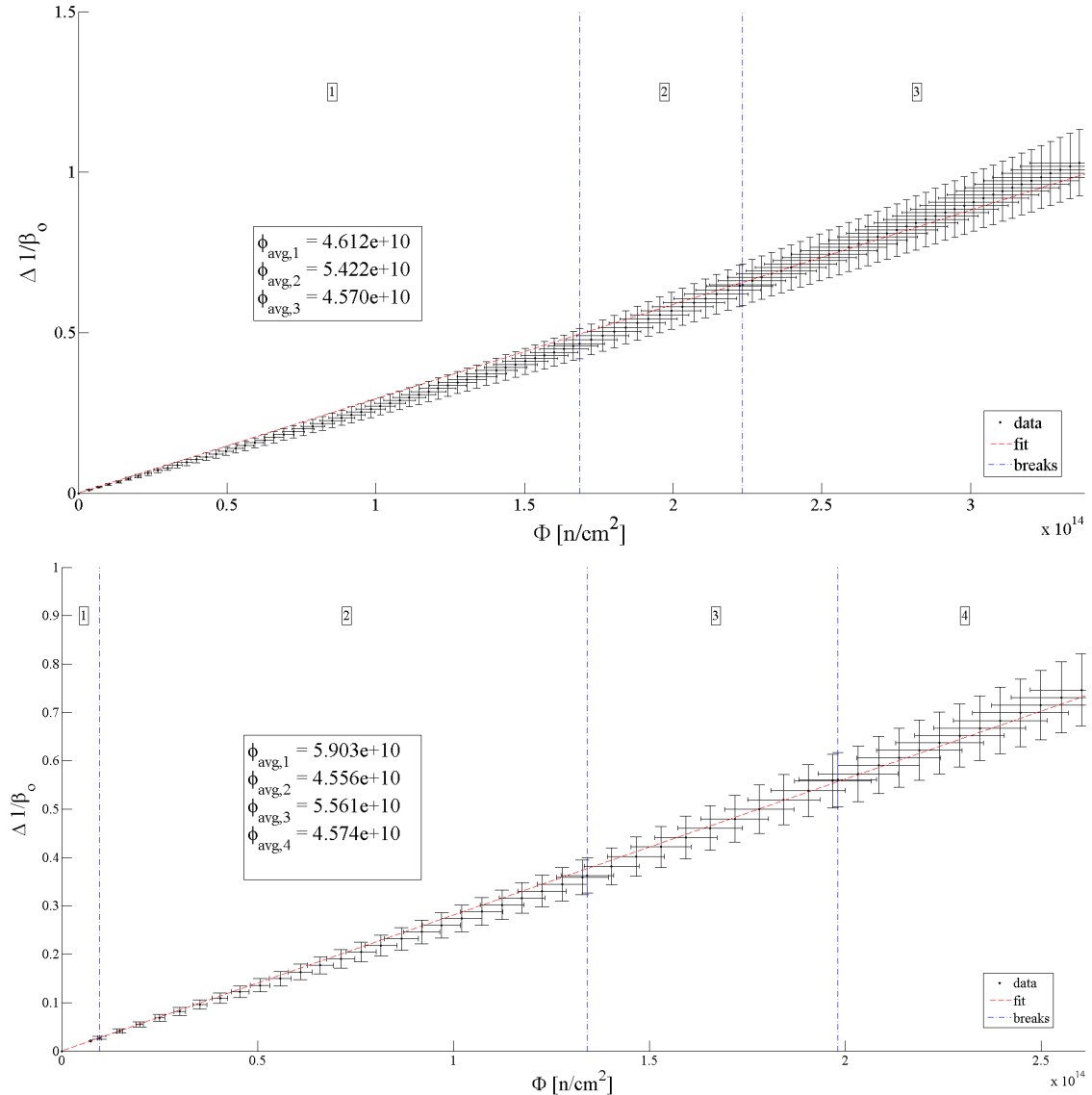


Figure 50. Shots 5F (top) and 8F (bottom) of the $\Delta(1/\beta)$ versus fluence. In these two shots, the proton beam current jumped between low and high values during the irradiation. The blue dotted vertical lines correspond to the time/fluence at which the beam current changed during the irradiation.

Unfortunately, these devices could not be recovered to perform the prescribed bake.

Table 17. The calculated damage constant and linear regression parameter for neutron irradiation at the IU NREF experimental set 2.

Shot	K ($\times 10^{-15}$) [cm 2 /n]
1T	4.186
2T	2.991
3T	2.739
4T	2.329
5F	3.086
6F	3.992
7F	2.640
8F	2.950
9F	3.646
AVG	3.173

Comparison with traditional single-pulse systems.

In Figure 75, a plot of the change in inverse gain as a function of fluence is plotted. However, this time, the results differ from the first experimental set at IU NREF. Most of the data sets lie above the line traced by the legacy data set, and the variation is most noticeable at higher fluences.

4.2 OSURR Experimental Series

After accomplishing the experiments at IU NREF, the research questions were investigated further by utilizing a different neutron source; the Ohio State University Research Reactor facility. Silicon BJTs were irradiated with neutrons and the current gain measured in the same fashion. The gain was then compared with experiments at other facilities.

The OSURR facility was used for this experiment because the model presented in Chapter III predicted a different response to radiation than in the IU NREF. Three

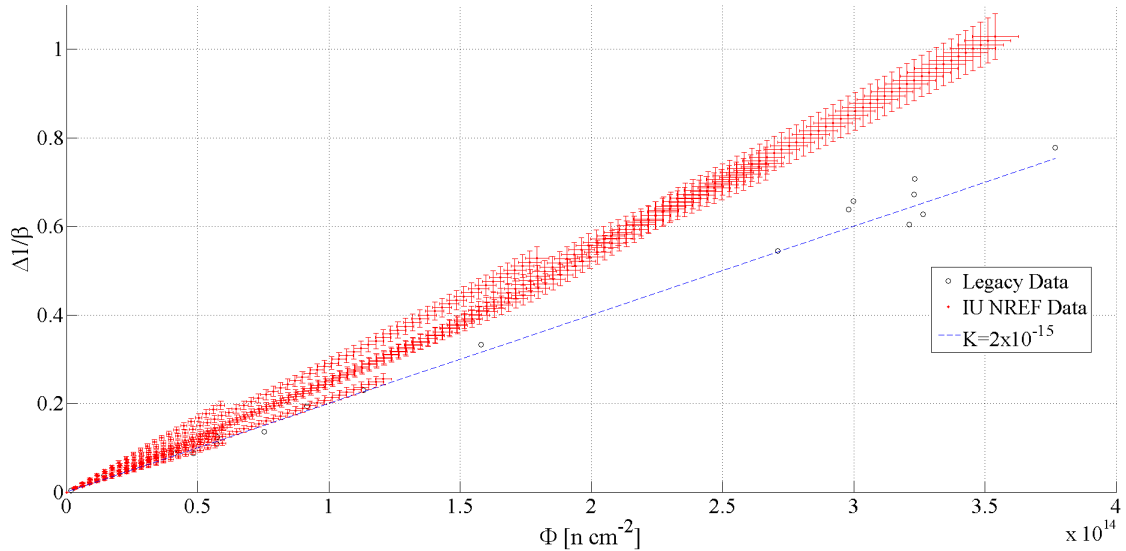


Figure 51. The $\Delta(1/\beta)$ versus fluence for the experimental data collected from the second experimental series at IU NREF as compared to data from various single-pulse, short-duration irradiation facilities such as SPR-III and WSMR FBR.

irradiation conditions were compared via simulation:

1. Typical IU NREF conditions with beam parameters of 20 Hz and $400 \mu\text{s}$
2. The IU NREF operating running with beam frequency “de-tuned” to 15 Hz, yet still having the same time-averaged flux as (1)
3. An OSURR-type neutron spectrum with the same 1-MeV equivalent neutron flux as (1) and (2).

In the third simulation, the reactor simulation included operation at a percentage of the maximum power to ensure the 1-MeV flux was the same as the time-averaged neutron flux at IU NREF. It is expected that using this type of facility would provide a device response with a damage constant lower than that found at the IU NREF.

The most important qualitative feature of the results of these simulations is that the NREF damage constant is different from the OSURR. At lower fluence, this is difficult to differentiate. However, as the simulation reaches higher total neutron

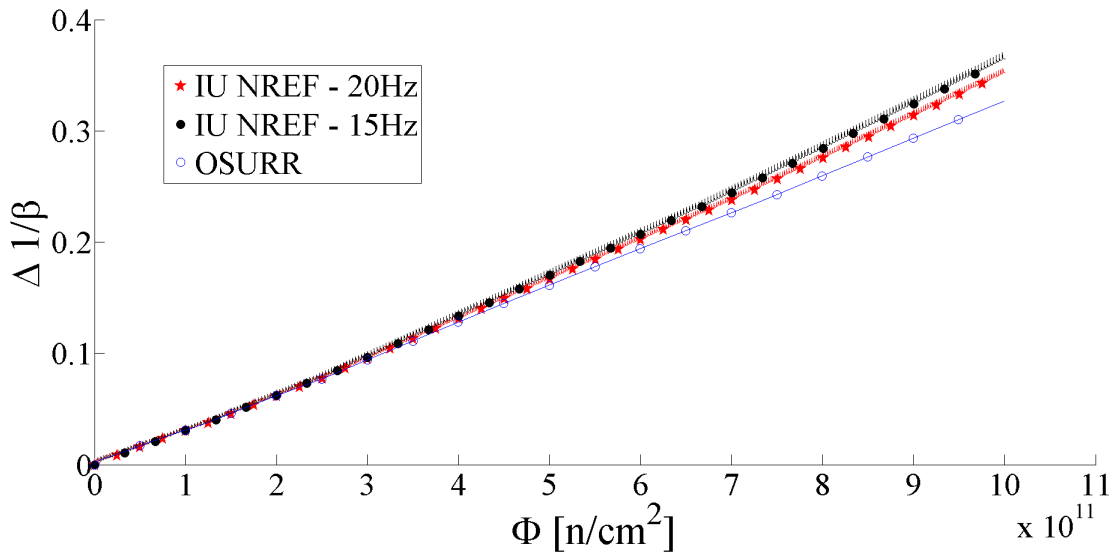


Figure 52. Simulation of three different irradiation conditions at the IU NREF and OSURR.

fluence, the three simulations begin to separate. The “detuned” IU NREF conditions result in the largest damage constant. This is because, to have the same 1-MeV equivalent (Si) neutron flux with a lower beam frequency, the instantaneous neutron flux must be higher. With the higher instantaneous flux, more damage is created with the same amount of total irradiation time. However, higher flux increases the amount of time in which no damage is occurring (*i.e.* time when the beam is off). Similarly, the OSURR has the smallest damage constant. All three simulations still follow the linear response with fluence as predicted by the Messenger-Spratt equation.

Facility Description.

The OSURR consists of a light water, pool-type research reactor. It is licensed to operate up to 500 kW and, at maximum steady-state power, the average thermal neutron flux is approximately 5×10^{12} n/cm²/s.

There are several sub-facilities within the reactor core, displayed in Figure 53, that allow researchers to select different neutron spectrum shapes and flux rates. The

Central Irradiation Facility (CIF) has an inner diameter of 1.3 inches and extends from the top of the pool down to a central grid position within the core. It has a maximum total flux of 2.3×10^{13} n/cm²/s and a maximum 1-MeV equivalent (Si) flux of 4.52×10^{12} n/cm²/s with a hardness of $H = 0.20$. The Auxiliary Irradiation Facility (AIF) is 2.5 inches in diameter, but the maximum fluxes are lower at $\phi_{tot} = 9.4 \times 10^{12}$ n/cm²/s and $\phi_{1-MeV} = 2.44 \times 10^{12}$ n/cm²/s, with a hardness of $H = 0.27$. An advantage of this is that the gamma flux is also lower because the additional water between the core and the tube attenuates the low energy gamma rays. The Peripheral Irradiation Facility (PIF) is also 2.5 inches in diameter and in a different position, with a maximum total flux of 5.3×10^{12} n/cm²/s. Finally, the thermal column has a thermalized neutron field with a maximum total flux of 6.8×10^{11} n/cm²/s. Flux values, except for the calculated 1-MeV equivalent (Si) fluxes, come from the OSURR web site [17].

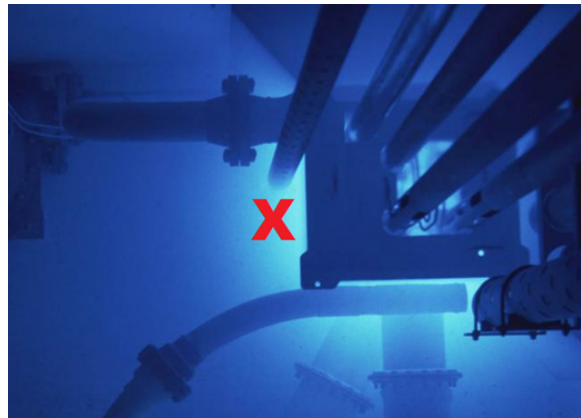


Figure 53. Image looking down in the OSURR reactor pool at the core during operation. This shows the multiple tubes and beam-ports available for use. The 7 inch tube used for irradiations was positioned at the red X. [Photo obtained from OSURR Staff.]

All of these facilities have advantages and disadvantages, however the one that was used was the 7 inch tube. Its position near the core is displayed as the red X in Figure 53. The 7 inch tube can be moved within the reactor pool, but the standard position allows a maximum total flux of 1.5×10^{12} n/cm²/s and a 1-MeV equivalent

(Si) flux of 1.92×10^{11} n/cm²/s with a hardness of 0.13 and a gamma dose of 6.5×10^4 rad(Si)/hr. The maximum flux and hardness are lower than the other tubes because the 7 inch tube is positioned the furthest from the center of the core when compared with the other major tubes.

The greater distance from the center of the core leads to additional neutron thermalization as neutrons travel through the light water coolant. The spectrum has been calculated using Monte Carlo simulations, and the calculations have been verified using foil activation analysis and spectrum unfolding using the Spectrum Analysis by Neutron Detectors (SAND-II) code [18]. The spectrum in the 7 inch tube is displayed in Figure 54.

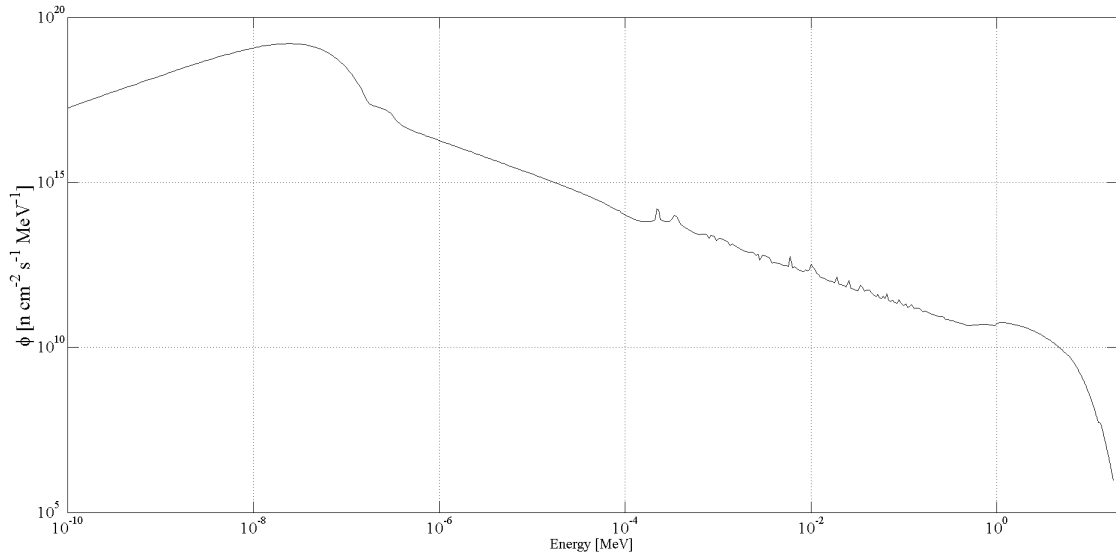


Figure 54. Neutron differential flux spectrum at the OSURR 7 inch tube at full power where the 1-MeV equivalent (Si) flux at this power level is 1.92×10^{11} n/cm²/s and the hardness is 0.13.

OSURR Test Equipment.

During irradiation, the two BJTs being measured were under constant electrical bias. To accomplish this, five Keithley 237 SMUs and one Agilent B2901A SMU were set up at the side of the reactor pool. Each BJT leg was connected to an SMU

via approximately 10 to 15 feet of BNC cabling. The SMUs data was output to a laptop, which was running a custom-built LabView virtual instrument, via General Purpose Interface Bus (GPIB) cables and a National Instruments Ethernet-to-GPIB converter. The setup is displayed in Figure 55.



Figure 55. SMU set up next to the OSURR reactor pool.

At the OSURR, there is an aluminum frame with an eye loop at the top which can be hooked to a lead plug for the top of the 7 inch tube. A simple cardboard frame with BNC cable throughputs was attached to this aluminum frame. A printed circuit board (PCB) was soldered directly to the BNC throughputs, and power sockets were soldered to the PCB. BJTs could be socketed to the PCB and removed easily for repeatability. The dosimetry packets were adhered to the cardboard frame. An image of the test rig set-up is displayed in Figure 56.

In addition to the BJT being tested, a second BJT was connected to the base leg of the device in order to shunt the gamma-induced photocurrent, as displayed in

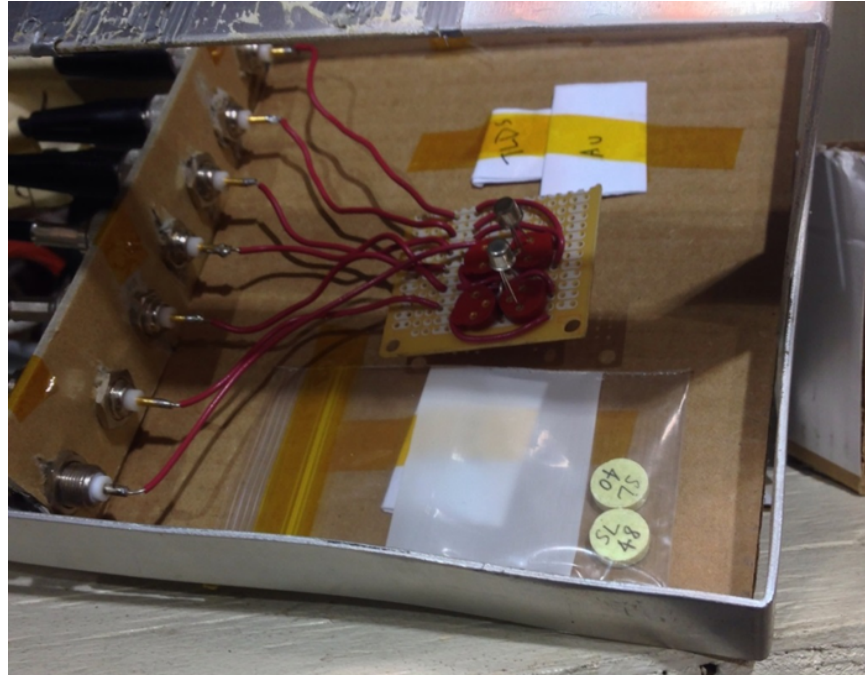


Figure 56. The test rig built for the OSURR experiments was simple and made from materials that would minimally activate so that the experiment could be accomplished as many times as possible while requiring the minimum downtime for radioactive decay between shots.

Figure 34. The gamma flux at the OSURR is significant, and the electrons promoted into the conduction band by gamma ionization in the base can mask current gain degradation during the measurement. Therefore, this shunting procedure must be done in order to properly measure BJT gain degradation.

OSURR Test Procedure.

Three irradiations were accomplished: two at 1% of maximum power, corresponding to 1.92×10^9 n/cm²/s, and one at 23.4% of maximum power, corresponding to 4.96×10^{10} n/cm²/s. For each of the three irradiations, two BJTs were placed in the printed circuit board rig and lowered into the core in the 7 inch tube. There were also dosimetry packets to validate the neutron flux for one of the 1% and for the 23.4% power irradiations. These packets consisted of 2 S pellets, 2 Fe foils, and 2 Au foils. For the 1% power dosimetry packet, there were also 14 TLDs. The dosimetry packet

for the 23.4% irradiation did not contain TLDs because they would have become too radioactive and would present a safety hazard when removed from the test fixture.

Initially, the core was subcritical and data recording commenced. The SMUs were set to source +10 V on the collector, -220 μ A on the emitter, and the base was set to SMU ground. The collector and base SMUs were set to source voltage and measure current, while the emitter SMU was set to source current and measure voltage. This configuration ensured that the collector-base junction was reverse-biased, while the emitter-base junction was forward-biased, causing the BJT to be in forward active mode at all times. It is in this mode that BJTs are designed to provide the greatest current gain; this also means that it is most sensitive to changes in defect species concentration during irradiation.

During reactor start-up, measurement continued. Then, when the reactor was at the desired power level, the twenty min timer began. The SMU output from all three legs was collected and, after 20 min, the reactor was shut down. Output was recorded until the devices were removed from the pool. After a period of time to allow short-lived radioactive isotopes to decay away, the test rig was pulled from the tube and the devices and dosimeters were removed from their positions.

Neutron Dosimetry.

The first step in dosimetry was to measure the masses of the pellets and foils. This data is tabulated in Table 18. The two neutron capture reactions for ^{54}Fe and ^{56}Fe were used for dosimetry purposes. Additionally, the gamma emitter ^{59}Fe was detected with the OSURR data due to neutron capture by ^{58}Fe . However, the ^{58}Fe isotope has an isotopic abundance of 0.2% in natural iron. Therefore, its gamma emission line is well-pronounced.

Equation 49 was used to calculate the saturation activity. For the Fe dosimeters,

Table 18. Mass measurement for the OSU dosimeters.

Mat'l	ID#	Mass (g)	+/-	N $^{32}\text{S}, ^{54}\text{Fe}, ^{197}\text{Au}$	N ^{56}Fe	N ^{58}Fe
S	SL40	0.5923	0.0001	1.056×10^{22}		
	SL48	0.5915	0.0001	1.055×10^{22}		
	SL1	0.6006	0.0001	1.071×10^{22}		
	SL7	0.5954	0.0001	1.062×10^{22}		
Fe	1	0.3075	0.0001	1.938×10^{20}	3.043×10^{21}	9.351×10^{18}
	2	0.3096	0.0001	1.952×10^{20}	3.063×10^{21}	9.415×10^{18}
	3	0.3060	0.0001	1.929×10^{20}	3.028×10^{21}	9.305×10^{18}
	4	0.3043	0.0001	1.918×10^{20}	3.011×10^{21}	9.254×10^{18}
Au	G	0.5993	0.0001	1.533×10^{21}		
	H	0.5194	0.0001	1.537×10^{21}		
	I	0.1227	0.0001	3.751×10^{20}		
	J	0.1208	0.0001	3.693×10^{20}		

the counting time was 86,400 s, or 1 full day. For the S pellets, the counting time was 300 s. The results of the measurement are tabulated in Tables 19, 20, and 21. In these tables, the acronym *NPA* stands for Net Peak Area and is the total number of counts under the curve for a gamma spectrum after background adjustment or the total number of counts for the beta detection system in the time interval.

Utilizing this information, the measured values of A_∞ can be compared against what is expected based on Monte Carlo particle simulation. As before, the activity at infinite irradiation is based on the Monte Carlo calculated spectrum and the isotopic capture cross section using the equation

$$A_\infty = n_x \int_0^{E_{\max}} \sigma_x^{cap}(E) \phi(E) dE, \quad (57)$$

where n_x is the number of isotope x in the sample of interest, σ_x^{cap} is the energy-dependent microscopic neutron capture cross section for the isotope x , and $\phi(E)$ is the energy-dependent differential neutron flux spectrum.

Figures 58 and 59 display plots of the measured dosimetric data as black dots on

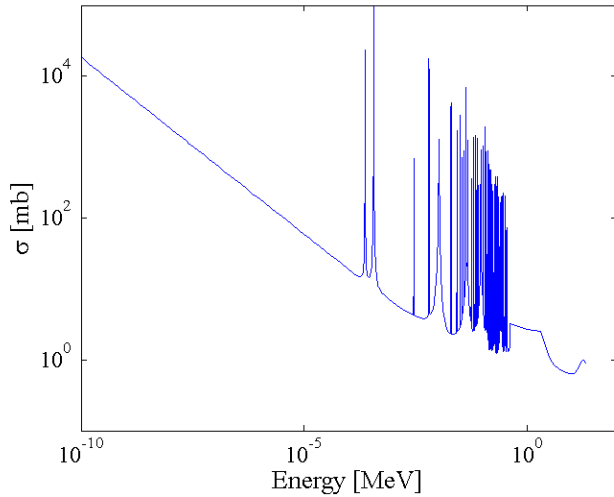


Figure 57. Cross sections for neutron capture by ^{58}Fe ; note that the units of the y-axis are in b this time.

the blue curves of A_∞ as a function of 1-MeV equivalent (Si) flux for the five isotopes of interest in this analysis. The vertical dotted line corresponds to the 1-MeV equivalent (Si) flux for the particular irradiation, $1.92 \times 10^9 \text{ n/cm}^2/\text{s}$ for the 1% irradiation and $4.96 \times 10^{10} \text{ n/cm}^2/\text{s}$ for the 23.4% irradiation.

At 1% power, both dosimetry packets agree well with the expected 1-MeV equivalent (Si) flux of $1.92 \times 10^9 \text{ n/cm}^2/\text{s}$. However, only dosimetry packet #2 has good agreement for the 23.4% power irradiation. Dosimetry packet #1 is consistently below the expected value of 1-MeV equivalent (Si) neutron flux. For the 23.4% irradiation, the dosimetry packets were positioned differently than for the 1% irradiation. While the packets were taped to cardboard next to the BJTs in the 1% irradiation, the packets were taped to the aluminum rig for the 23.4% irradiation. The rig can rotate freely, and this is most likely the cause of the discrepancy. If the rig rotated such that first dosimetry packet were further away from the core, the flux would consequently be lower due to $1/r^2$ streaming. With this understanding and recognizing that the BJTs were positioned between the two dosimetry packets for the 23.4% irradiation, the predicted values were accepted for these two irradiations. The values of 1-MeV

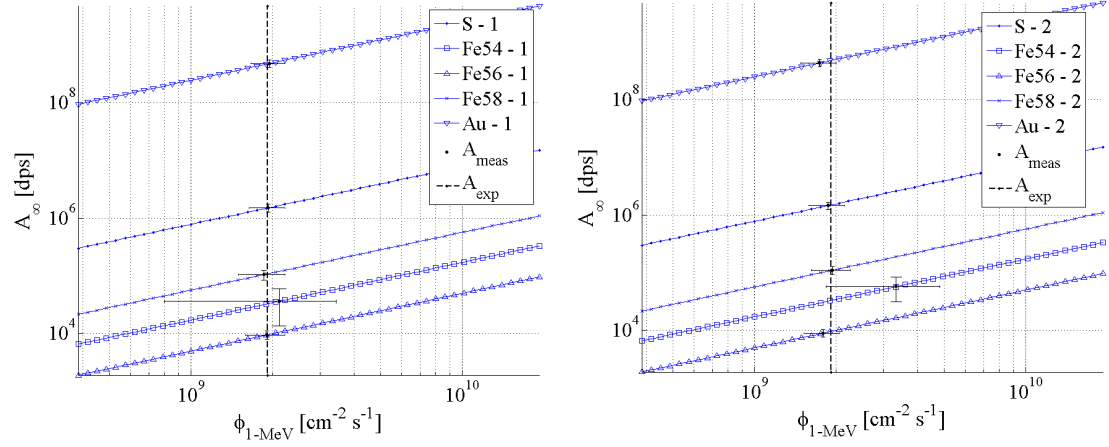


Figure 58. Comparison of measured dosimetric data (black dots) for packet 1 (left) and packet 2 (right) with curves of saturation activity as a function of 1-MeV equivalent flux with the expected value of 1.92×10^9 n/cm 2 /s for 1% power in the 7 inch tube at OSURR shows that the pellet/foil set agrees well with the Monte Carlo simulation results and OSURR reactor estimates, within experimental error.

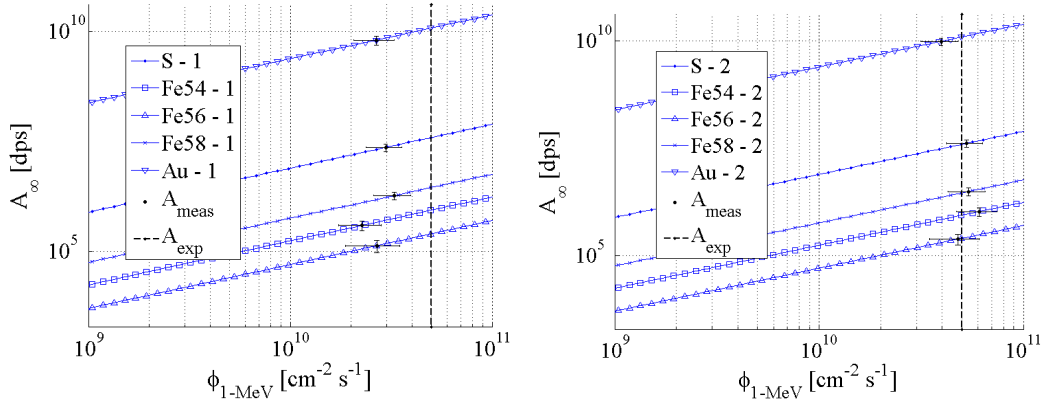


Figure 59. Comparison of measured dosimetric data (black dots) for packet 1 (left) and packet 2 (right) with curves of saturation activity as a function of 1-MeV equivalent flux with the expected value of 4.96×10^{10} n/cm 2 /s for 23.4% power in the 7 inch tube at OSURR shows that the pellet/foil set agrees well with the Monte Carlo simulation results and OSURR reactor estimates, within experimental error.

Table 19. Iron foil dosimetry analysis for the OSU dosimeters.

ID#	Rxn. Prod.	Epeak [keV]	t _{wait}	Det. ε	$\frac{(C-B)}{\varepsilon}$	A _{∞} [dps]	A _{∞} Unc. [%]
1	Mn-54	835	4371	2.00×10^{-3}	3.35×10^4	3.63×10^4	52.32%
	Mn-56	847		2.28×10^{-3}	6.79×10^6	1.05×10^4	5.85%
	Fe-59	1099.251		1.40×10^{-3}	1.38×10^6	1.07×10^5	8.66%
	Fe-59	1291.596		1.25×10^{-3}	1.34×10^6	1.04×10^5	9.62%
	Mn-56	1811		1.00×10^{-3}	7.06×10^6	8.63×10^3	7.37%
2	Mn-54	835	4350	2.00×10^{-3}	5.70×10^4	6.17×10^4	22.13%
	Mn-56	847		2.28×10^{-3}	4.66×10^6	7.19×10^3	6.02%
	Fe-59	1099.251		1.40×10^{-3}	9.00×10^5	6.98×10^4	9.36%
	Fe-59	1291.596		1.25×10^{-3}	1.06×10^6	8.21×10^4	9.78%
	Mn-56	1811		1.00×10^{-3}	4.96×10^6	6.05×10^3	7.82%
3	Mn-54	835	4371	2.00×10^{-3}	3.35×10^4	3.63×10^4	52.32%
	Mn-56	847		2.28×10^{-3}	6.79×10^6	1.05×10^4	5.85%
	Fe-59	1099.251		1.40×10^{-3}	1.38×10^6	1.07×10^5	8.66%
	Fe-59	1291.596		1.25×10^{-3}	1.34×10^6	1.04×10^5	9.62%
	Mn-56	1811		1.00×10^{-3}	7.06×10^6	8.63×10^3	7.37%
4	Mn-54	835	4350	2.00×10^{-3}	5.70×10^4	6.17×10^4	22.13%
	Mn-56	847		2.28×10^{-3}	4.66×10^6	7.19×10^3	6.02%
	Fe-59	1099.251		1.40×10^{-3}	9.00×10^5	6.98×10^4	9.36%
	Fe-59	1291.596		1.25×10^{-3}	1.06×10^6	8.21×10^4	9.78%
	Mn-56	1811		1.00×10^{-3}	4.96×10^6	6.05×10^3	7.82%

equivalent (Si) flux were thus used for the analysis to be completed in the next section.

BJT Gain Degradation Experiment.

For this experiment, there were two methods of BJT current gain data collection. For one of the 1% reactor power irradiations, gain was recorded as was done in the IU NREF experiment set, *i.e.* +10 V of DC voltage on the collector, -220 μ A of DC current on the emitter, the base grounded to SMU ground, and the base and collector currents measured to calculate gain. For the 23.4% irradiation, the emitter and base legs were biased at the same levels. However, the collector voltage was swept from -1 V to 20 V with 40 data points between -1 and +1 and 20 data points between +1 and +20. The reason for dividing up the range in this manner is that the BJT

Table 20. Sulfur pellet dosimetry analysis for the OSU dosimeters.

ID#	t_{wait}	NPA	$\frac{(C-B)}{\varepsilon}$	A_∞ [dps]	A_∞ Unc. [%]
Sl40.1	68087	7.83×10^4	1.03×10^3	1.53×10^6	5.39%
Sl40.2	68405	7.80×10^4	1.02×10^3	1.52×10^6	5.39%
Sl40.3	68720	7.85×10^4	1.03×10^3	1.53×10^6	5.39%
Sl40.4	69660	7.78×10^4	1.02×10^3	1.52×10^6	5.39%
Sl40.5	71185	7.72×10^4	1.01×10^3	1.51×10^6	5.40%
Sl48.1	71605	7.38×10^4	9.70×10^2	1.44×10^6	5.40%
Sl48.2	71920	7.40×10^4	9.72×10^2	1.44×10^6	5.40%
Sl48.3	72952	7.40×10^4	9.73×10^2	1.45×10^6	5.40%
Sl48.4	74105	7.40×10^4	9.74×10^2	1.45×10^6	5.40%
Sl48.5	74417	7.40×10^4	9.75×10^2	1.45×10^6	5.40%
Sl1.1	72040	7.89×10^5	4.48×10^6	2.31×10^7	5.15%
Sl1.2	72370	7.88×10^5	4.48×10^6	2.31×10^7	5.15%
Sl1.3	72775	7.87×10^5	4.47×10^6	2.31×10^7	5.15%
Sl1.4	73105	7.88×10^5	4.48×10^6	2.31×10^7	5.15%
Sl1.5	73435	7.87×10^5	4.47×10^6	2.31×10^7	5.15%
Sl1.6	73705	7.88×10^5	4.48×10^6	2.31×10^7	5.15%
Sl1.7	74110	7.86×10^5	4.46×10^6	2.30×10^7	5.15%
Sl7.1	74460	1.39×10^6	7.92×10^6	4.09×10^7	5.12%
Sl7.2	74800	1.39×10^6	7.92×10^6	4.09×10^7	5.12%
Sl7.3	75300	1.39×10^6	7.92×10^6	4.09×10^7	5.12%
Sl7.4	75640	1.39×10^6	7.91×10^6	4.08×10^7	5.12%
Sl7.5	75979	1.39×10^6	7.91×10^6	4.09×10^7	5.12%
Sl7.6	76330	1.39×10^6	7.93×10^6	4.09×10^7	5.12%
Sl7.7	76670	1.39×10^6	7.90×10^6	4.08×10^7	5.12%

switches operation modes, essentially *turning on*, between -1 and 0 V. Therefore, in order to best measure the transition from negative current to positive current in the collector, the finer grid of points was selected. Then, from +1 to +20 V, there is little change so a coarser grid was selected to minimize the time required for each sweep.

1% Power / DC Measurements.

Using the SMUs, BJT current gain was measured as a function of time for both DuTs before, during, and after the 20 min irradiation at 1% of maximum reactor

Table 21. Gold foil dosimetry analysis for the OSU dosimeters.

ID#	E_{peak}	t_{wait}	NPA	$\frac{(C-B)}{\varepsilon}$	A_∞ [dps]	A_∞ Unc. [%]
AuG	411.802	66650	3.20×10^6	4.18×10^9	4.77×10^9	5.18%
	678.8	66650	1.68×10^4	4.17×10^9	4.75×10^9	7.50%
	1087.4	66650	2.36×10^3	4.12×10^9	4.70×10^9	11.52%
AuH	411.802	67565	3.13×10^6	4.09×10^9	4.68×10^9	5.18%
	678.8	67565	1.68×10^4	4.17×10^9	4.77×10^9	5.29%
	1087.4	67565	1.92×10^3	3.35×10^9	3.84×10^9	12.35%
AuI	411.802	758872	6.96×10^5	1.08×10^9	9.66×10^9	5.12%
	678.8	758872	3.60×10^3	1.08×10^9	9.66×10^9	6.75%
	1087.4	758872	4.42×10^2	1.08×10^9	9.65×10^9	10.01%
AuJ	411.802	758872	5.15×10^5	7.23×10^8	6.48×10^9	5.14%
	678.8	758872	2.73×10^3	7.22×10^8	6.47×10^9	6.98%
	1087.4	758872	3.58×10^2	7.22×10^8	6.46×10^9	10.44%

power. The raw data is displayed in Figure 60. The first 25 min show reactor start up. Following this, the reactor is maintained at the designated power for 20 min, at which time annealing is monitored when the reactor is turned off.

Figure 61 displays the change in inverse gain for the 20 min irradiation as a function of 1-MeV equivalent (Si) fluence as calculated from ASTM Standard E722-09e1 [19]. In this figure, there are two distinct curves: one with and one without gamma displacement damage correction. It is possible that the damage induced in a semiconductor device can be inflated by sufficiently high gamma doses. Therefore, an additional term representing damage due to gamma recoil was included in the Messenger-Spratt equation as $K\Phi(t) = \Delta_{\beta_o} - K_\gamma D_\gamma$ where K_γ is the damage factor and D_γ is the gamma dose in Gy. The value of the damage factor stated in ASTM standard E722 is 1.5×10^{-5} Gy $^{-1}$. This correction factor was not applied for the IU NREF gain degradation analysis because, contrary to thermal nuclear reactors, the gamma flux at the IU NREF is quite low. Therefore, the correction factor was negligible in comparison to experimental error.

In Figure 61, the time-averaged flux was assumed to be the value determined by

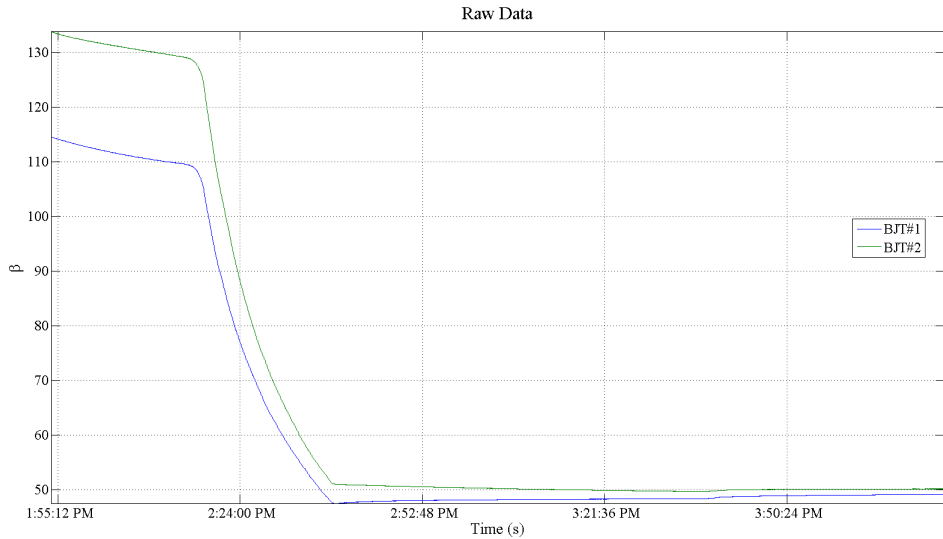


Figure 60. Raw data from irradiation of 2 BJTs at the OSURR at 1% power for 20 minutes.

dosimetry. Therefore, the slope of the line, which corresponds directly to the damage factor K , is calculated to be $3.77 \times 10^{-15} \text{ cm}^2/\text{n}$. It is interesting to note in Figure 61 how little of an effect that gammas have on gain degradation.

23.4% Power / Sweep Measurement.

Again, BJT current gain was measured as a function of time for 2 BJTs before, during, and after the 20 min irradiation at 1% of maximum reactor power. However, this time, the collector voltage was swept from -1 V to +20 V once approximately every 1.5 s.

Figure 62 displays a plot of all the sweeps from the 23.4% power sweep measurement. The important features of this graph are the *turn-on* region around -0.5 V and the instability in the sweep at voltages greater than 5 V. The *turn-on* region is important because several features about it will be used in later analysis. Those features are voltage range from 10 to 90% of operating voltage and voltage at zero current. As more defects are injected into the device, these parameters should get

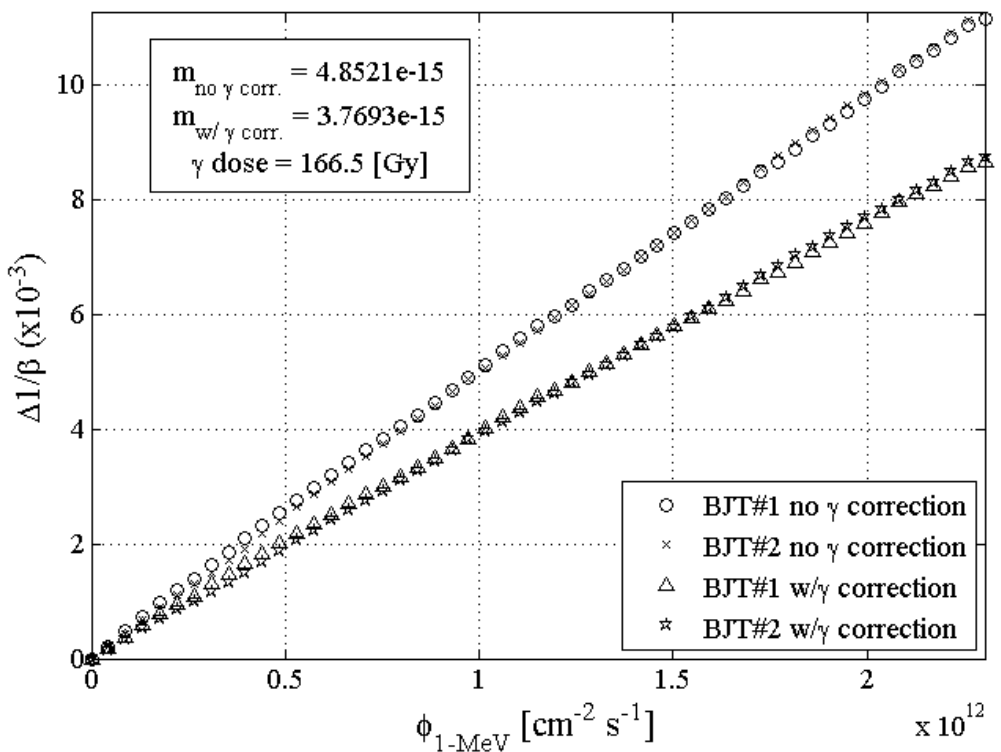


Figure 61. The $\Delta(1/\beta)$ with fluence for the 20 minute irradiation; gain change has been corrected for gamma dose using the ASTM standard value of gamma displacement damage factor.

larger as it will require a greater potential to flip the collector-base region to reverse bias and into an “on” state.

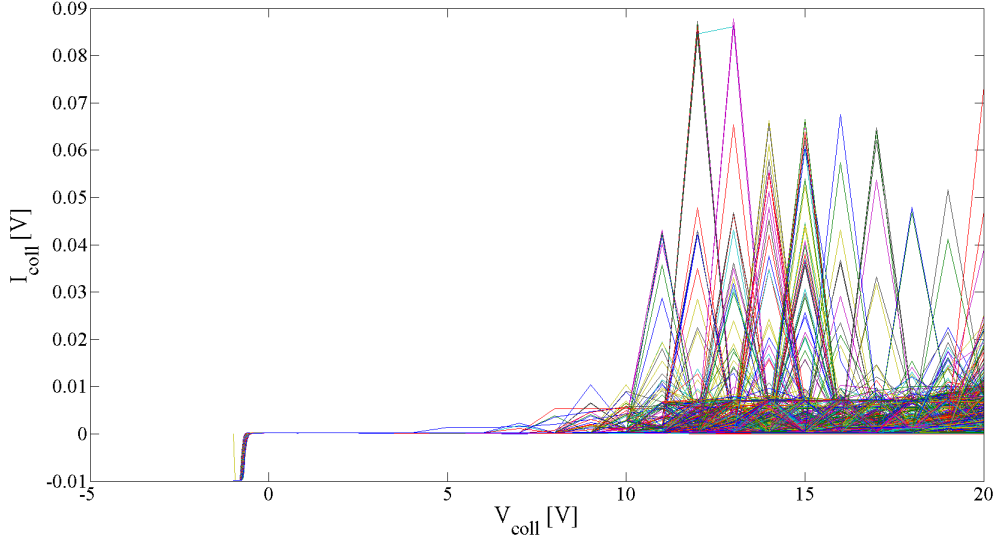


Figure 62. The collector current as a function of collector voltage for the 26% power shot.

From these sweeps, the device gain can be sampled at a voltage of interest. While +10 V was the voltage sourced to the collector in the IU NREF experiments, this voltage could not be used in this analysis. There was an unresolved issue with auto-ranging in the SMU that was not noticed until post-experiment analysis. This caused destabilization of the SMU measurement capability at high voltages and caused the measurement of collector current at voltages greater than +5 V to be unsuitable for analysis. Therefore, +0.9 V was selected for this analysis, as the collector current changes very little before reaching instability at +5 V. Figure 63 is a plot of the Messenger-Spratt response for the higher reactor power irradiation. In this figure, the two irradiated BJTs have differing responses. It is believed that BJT2 shorted to the power socket connections. Additionally, BJT1 responded in a non-linear fashion. However, this is likely due to the reactor operator performing adjustments in order to stabilize the reactor. Therefore, time is not a linear function of fluence, which affects

the $\Delta(1/\beta)$ plot.

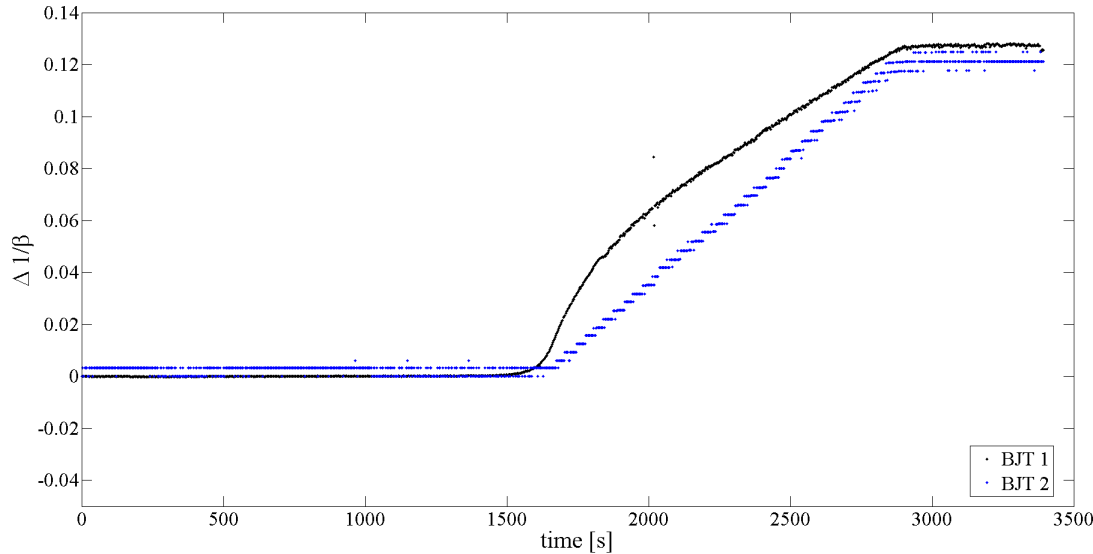


Figure 63. The Messenger-Spratt response during irradiation by $4.96 \times 10^{10} n/cm^2/s$ 1-MeV equivalent (Si) neutrons.

Neutron dosimetry proved that the average 1-MeV equivalent (Si) flux was $4.96 \times 10^{10} n/cm^2/s$ for this irradiation; and if the final value of $\Delta(1/\beta)$ is 0.1254, then the damage constant is $2.11 \times 10^{-15} \text{ cm}^2/n$. However, this value has not been gamma displacement damage corrected. The gamma dose was 217 Gy leading to a correction factor of 3.26×10^{-3} , changing the damage factor to $2.05 \times 10^{-15} \text{ cm}^2/n$. This value of the damage constant is much more consistent with that found in literature, and it is different from that found during the IU NREF experiments.

ASTM Bake.

The devices from OSURR versions 1 and 2 were placed in an oven and heated to 80°C for 2 hours as prescribed by the ASTM E1855 standard. The device gain was measured for three devices after this period of temperature-assisted annealing: (1) OSURR version 1 at low power, (2) OSURR version 2 at low power, and (3) OSURR version 2 at high power. Then, the annealing factor was calculated for these three

devices. The results are displayed in Figure 64. The slope of each line was determined using linear regression, and the average value was $-0.026(\pm 5.97\%)$.

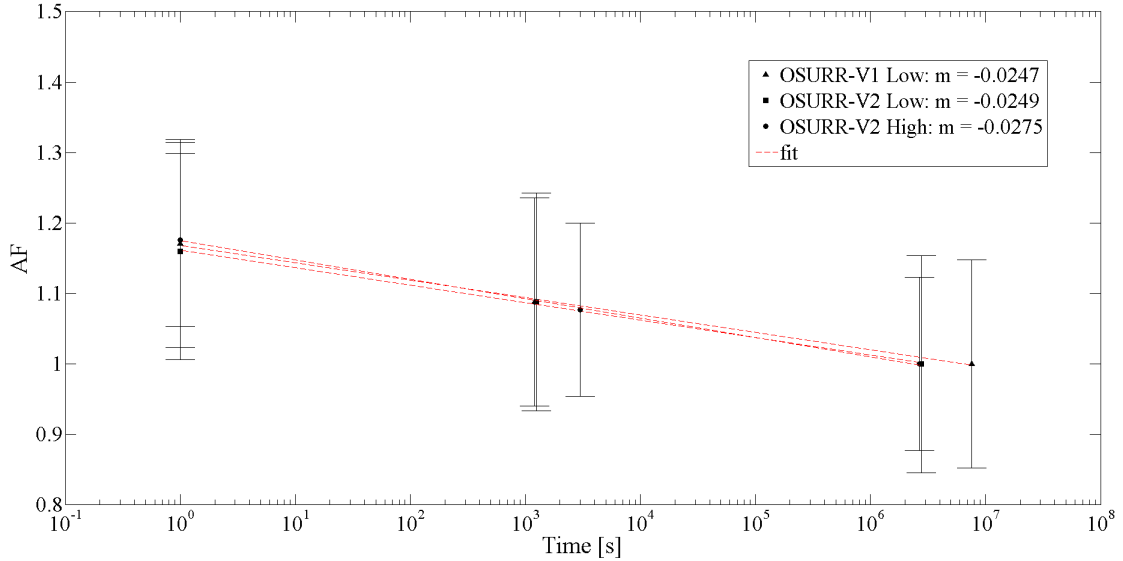


Figure 64. The annealing factor of the BJTs irradiated at the OSURR as a function of time after irradiation is completed.

The $\Delta(1/\beta)$ was calculated after baking and the results are plotted in Figure 65. The damage constant, K , is calculated using the initial gain and final gain in Equation 58.

$$K = (\Delta 1/\beta) \Phi \quad (58)$$

The result of applying Equation 58 is that $K = 2.36 \times 10^{-15} \text{ cm}^2/\text{n}$ for the OSURR Version 1 BJT at low power, $K = 1.72 \times 10^{-15} \text{ cm}^2/\text{n}$ for the OSURR Version 2 BJT at low power, and $K = 1.60 \times 10^{-15} \text{ cm}^2/\text{n}$ for the OSURR Version 2 BJT at high power. It is interesting to note that the two Version 2 BJTs have a lower damage constant than the Version 1 BJT, but this is also manifested in the *in-situ* measurements. As already mentioned, this measurement suffers from not having enough data points.

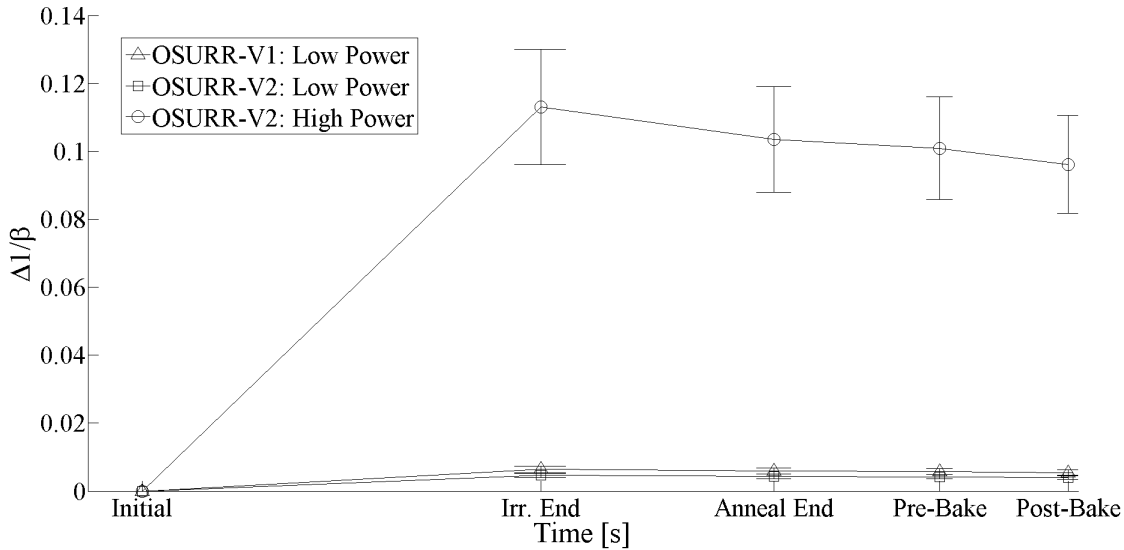


Figure 65. The $\Delta(1/\beta)$ as a function of the point in time where the measurement was taken; note that the x -axis is an arbitrary scale.

Comparison with traditional single-pulse systems.

Now that data has been collected from both the IU NREF in pulsed mode and the OSURR at constant power, a comparison can be made between these two types of facilities and the legacy, single-pulse systems, as shown in Figure 66.

The $1/\beta$ data collected at the OSURR falls below the data from IU NREF at the end of irradiation. Since there is no accounting for real-time reactor flux changes due to operations, it is best to ignore the curvature and focus on the end value, which falls below the IU NREF measurements but consistent with legacy data. However, as happened before with the IU NREF data, this is only one set of BJTs, and only one of the two irradiated BJTs provided an interpretable result. More experimenting is needed to truly verify the damage constant as found in Figure 66.

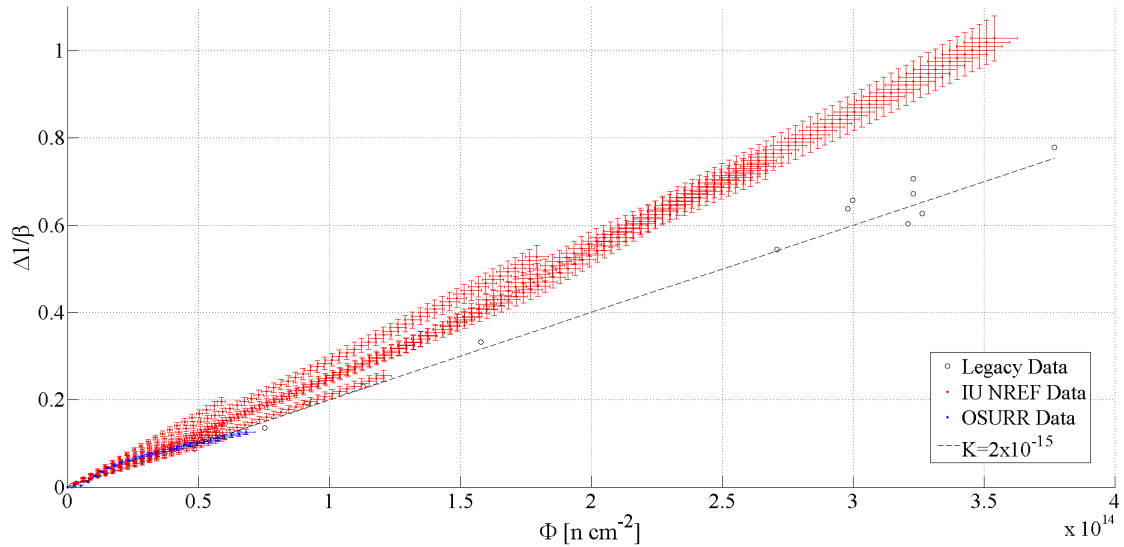


Figure 66. The devices respond differently for different neutron spectra; however, it is yet to be proven whether the ASTM elevated temperature annealing interval will have a significant enough impact to bring all devices back to the literature value for the damage constant.

References

1. ASTM Standard E1855-10, *Standard Test Method for Use of 2N2222A Silicon Bipolar Transistors as Neutron Spectrum Sensors and Displacement Damage Monitors*, ASTM International, West Conshohocken, PA, 2010.
2. M. Halstead, “Characterization of the energy spectrum at the Indiana University NREP neutron source,” Master’s thesis, Air Force Institute of Technology, March 2011.
3. M. Halstead, S. Lee, J. Petrosky, A. Bickley, and P. Sokol, “Neutron energy spectrum characterization on TMR-1 at the Indiana University neutron source,” *Phys. Proc.*, vol. 26, pp. 188–195, 2012.
4. M. Halstead, S. Lee, J. Petrosky, A. Bickley, J. McClory, S. Clark, and P. Sokol, “Neutron flux spectrum characterization of a compact, accelerator-driven neutron source at Indiana University,” *J. Rad. Eff. Res. Eng.*, vol. 31, no. 1, pp. 117–123, 2013.
5. A. Bickley, M. Halstead, J. McClory, S. Lee, P. Sokol, and J. Petrosky, “Evaluation of the neutron energy spectrum produced at the neutron radiation effects beam line utilizing a computational Monte Carlo approach,” *J. Rad. Eff. Res. Eng.*, vol. 31, no. 1, pp. 23–27, 2013.

6. A. Bogdanov, V. Anferov, M. Ball, D. Baxter, V. Derenchuk, A. Klyachko, T. Rinckel, P. Sokol, and K. Solberg, “Upgrade of the LENS proton LINAC: Commissioning and results,” in *Proceedings of PAC07*, 2007.
7. C. Lavelle, “The neutronic design and performance of the Indiana University Cyclotron Facility (IUCF) Low Energy Neutron Source,” Ph.D. dissertation, Indiana University, 2007.
8. B. von Przewoski, T. Rinckel, W. Manwaring, T. Ellis, C. Foster, E. Hall, T. Kinser, and K. Murray, “Beam properties of the new radiation effects research stations at Indiana University Cyclotron Facility,” in *MRS Proceedings*, vol. 851. Cambridge Univ. Press, 2004, pp. NN7–10.
9. B. von Przewoski, D. Baxter, A. Bogdanov, S. Clark, V. Derenchuk, T. Ellis, C. Lavelle, M. Leuschner, N. Remmes, T. Rinckel, P. Sokol, and T. Turflinger, “The Neutron Radiation Effects Program (NREP) at Indiana University Cyclotron Facility,” in *IEEE Rad. Eff. Data Workshop*, 2006, pp. 188–190.
10. M. Leuschner, D. Baxter, V. Derenchuk, H. Kaiser, C. Lavelle, H. Nann, T. Remmes, T. Rinckel, W. Snow, and P. Sokol, “LENS: a new university-based neutron source for science and education,” in *Proceedings of the Nineteenth International Conference on the Application of Accelerators in Research and Industry*, 2007, pp. 956–959.
11. “Personal correspondance with Dr. Sanjin Lee at the IU NREF,” 2011.
12. E. Bielejec, G. Vizkelethy, R. Fleming, W. Wampler, S. Myers, and D. King, “Comparison between experimental and simulation results for ion beam and neutron irradiations in silicon bipolar junction transistors,” *IEEE Trans. Nucl. Sci.*, vol. 55, no. 6, pp. 3055–3059, December 2008.
13. “MCNPX user’s manual, version 2.7.0,” Los Alamos National Laboratory, Albuquerque, NM, Tech. Rep. LA-CP-11-00438, April 2008.
14. 4145a/b semiconductor parameter analyzers [obsolete] — agilent. [Online]. Available: <http://www.home.agilent.com/en/pd-542807-pn-4145B/semiconductor-parameter-analyzers?&cc=US&lc=eng>
15. ASTM Standard E265-07(2013), *Standard Test Method for Measuring Reaction Rates and Fast-Neutron Fluences by Radioactivation of Sulfur-32*, ASTM International, West Conshohocken, PA, 2013.
16. ASTM Standard E263-13, *Standard Test Method for Measuring Fast-Neutron Reaction Rates by Radioactivation of Iron*, ASTM International, West Conshohocken, PA, 2013.

17. (2014, February) Research reactor — nuclear reactor lab. The Ohio State University Research Reactor. [Online]. Available: <http://reactor.osu.edu/facilities/research-reactor>
18. "Personal correspondance with Dr. Susan White at the OSURR," March 2014.
19. ASTM Standard E722-09(e1), *Standard Practice for Characterizing Neutron Energy Fluence Spectra in Terms of an Equivalent Monoenergetic Neutron Fluence for Radiation-Hardness Testing of Electronics*, ASTM International, West Conshohocken, PA, 2009.

V. Comparison of Model to Experiment

The experimental evidence was compared to the mathematical model developed in Chapter III. Initially, a sensitivity analysis and parametric study were accomplished to determine the set of parameters required to fit the experimental results. In this chapter, these two studies are described, the results are analyzed, and the resultant parameter set used for comparison against the experimental data collected from the IU NREF and OSURR.

5.1 Sensitivity Analysis

Since it was determined in Section 3.2 that the values for model parameters have wide variation in literature, a sensitivity analysis was warranted to determine which were most important. This sensitivity study was accomplished when the model contained six equations, so the model used was as shown in Equation Set 30. In Equation 30, the six species are vacancies (V), divacancies (VV), interstitials (I), vacancy-impurity complexes (VX), divacancy-impurity complexes (VVX), and impurities (X).

The system of six coupled differential equations has a total of 17 parameters that were analyzed for sensitivity. These seventeen parameters were selected because of their use in the determination of the rate coefficients related to Equation 30. They are tabulated in Table 22. In this table, there is the expectation, or most common, value of each parameter derived from the literature. Likewise, the upper and lower boundaries of the sensitivity analysis were selected to encompass the range of values found in literature.

If ten values were selected from within each parameter's range, the problem would require 10^{17} permutations of the parameter subsets to be solved, stored, and analyzed. This is not computationally feasible from a resource requirement or an analysis

Table 22. Parameters (P), Expectation values ($\langle P \rangle$), and Ranges (R) for 17 parameters varied in sensitivity study. Units of D are cm^2/s , units of E are eV, units of ν are s^{-1} and units of Radius are Å.

#	P	$\langle P \rangle$	R	#	P	$\langle P \rangle$	R
1	D_v	3×10^{-10}	$3 \times 10^{-13} - 3 \times 10^{-9}$	10	ν_{vvx}	10^{13}	$10^{12} - 10^{14}$
2	D_i	2×10^{-15}	$2 \times 10^{-16} - 2 \times 10^{-14}$	11	$R_{v,i}$	1	$0.1 - 5$
3	D_{vv}	1×10^{-15}	$1 \times 10^{-16} - 1 \times 10^{-14}$	12	$R_{v,v}$	1	$0.1 - 5$
4	E_{vv}	1.6	$1.0 - 2.5$	13	$R_{v,x}$	1	$0.1 - 5$
5	E_{vx}	1.7	$1.0 - 2.5$	14	$R_{v,vx}$	1	$0.1 - 5$
6	E_{v-vx}	2.24	$2.0 - 2.5$	15	$R_{i,vx}$	1	$0.1 - 5$
7	E_{vv-x}	2.98	$2.5 - 3.5$	16	$R_{i,vvx}$	1	$0.1 - 5$
8	ν_{vv}	10^{13}	$10^{12} - 10^{14}$	17	$R_{vv,x}$	1	$0.1 - 5$
9	ν_{vx}	10^{13}	$10^{12} - 10^{14}$				

perspective. Therefore, an alternative method of accomplishing the sensitivity analysis was investigated.

In 1979, M.D. McKay [1] developed a theory, later expanded upon by R.L. Iman and others [2], that used Latin Squares to select input parameters to best cover the tested space. A Latin Square is an $n \times n$ array filled with n symbols, each occurring 1 time in each row and each column. A 3×3 example is shown in Figure 67. A Latin hypercube is the generalization of this concept to N dimensions. McKay's method is often called Latin Hypercube Sampling (LHS).

To determine the simulation space, each variable range is broken up into m equally probable bins. Points are then randomly selected from within those bins and placed in the simulation space to satisfy the Latin hypercube requirement (occurring only 1 time in each row, column, page, sheet, *etc.*).

The mathematical software suite Matlab [3] has a built-in function called *lhsdesign*(n, m) that takes as arguments the number of parameters, n , and the number of bins, m . The output of this function is an $n \times m$ matrix of numbers between 0 and 1 that satisfy the Latin hypercube requirement. By applying this matrix with the

A	B	C
C	A	B
B	C	A

Figure 67. This example of a Latin Square shows the three values – A , B , and C – positioned such that each value is used exactly once in every row and column.

lower and upper bounds of the parameters, the range can be sampled efficiently. The result is a simulation space that covers all ranges without requiring 10^{17} parameter sets to sample the entire range.

For the first sensitivity study, the generation rate of Frenkel Pairs (FP) was constant for $400\mu\text{s}$. The instantaneous IU NREF neutron energy flux was folded into the displacement damage kerma for silicon as found in the ASTM Standard E722 [4] and is plotted in Figure 17. The total damage was integrated over the spectrum (plotted in Figure 68), and the result was divided by the amount of energy needed for the liberation of a silicon atom from the lattice and thus formation of vacancy/interstitial pair. This was used as the generation rate for interstitials and vacancies, $G_i = G_v$, and as an input in the model. The initial concentration conditions ($C_v(t = 0)$, $C_{vv}(t = 0)$, etc.) and other known parameters, such as the temperature and the irradiation time, are input parameters to the model.

The result of this analysis was then plotted, and an example of the results is displayed in Figure 69. In this figure, the vacancy concentration is on the z -axis while the x - and y -axes are time and silicon vacancy diffusivity, D_v . There is a change in the vacancy concentration over the range, which shows that the input affected the

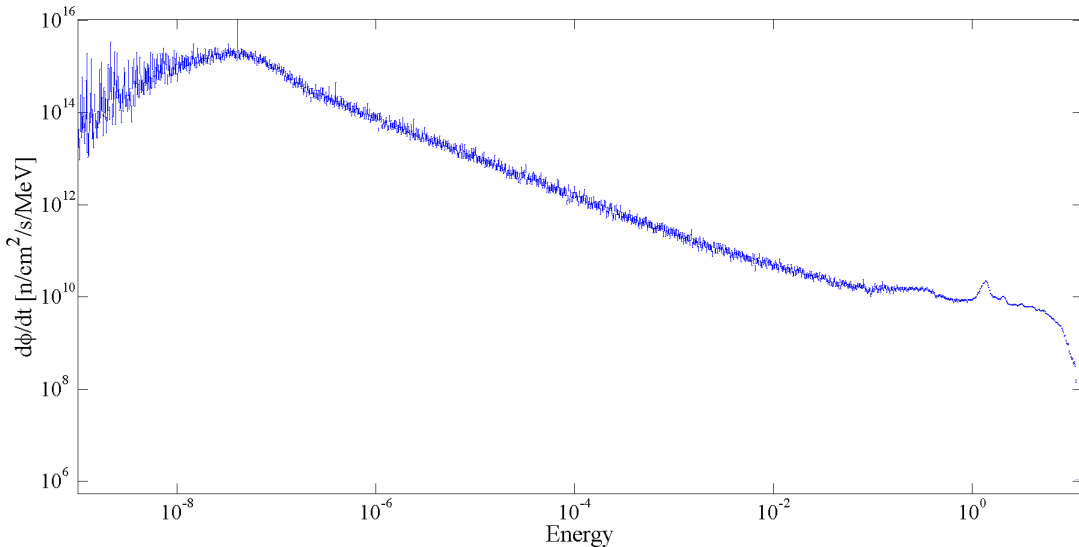


Figure 68. The time-averaged differential neutron flux at the IU NREF that was used for sensitivity analysis.

output. The same analytical techniques were applied to the other parameters. Of the initial 17 parameters selected for sensitivity analysis, the vacancy diffusivity, D_v presented any sensitivity over its range. Therefore, when transitioning into using the newer model with 11 instead of 6 species and subsequently performing the parameter search, only D_v was added to the list of parameters for this search.

5.2 Parameter Search

Following the sensitivity analysis, the model was improved from 6 species to 11 species, to include multiple defect clusters. Additionally, the ability to calculate device gain based on semiconductor material parameters was added. At this point, the model parameters were analyzed again. This time, however, the results predicted by the model were compared against experimental data collected during the first experiment at IU NREF. In this way, the LHS methodology was used as a searching mechanism for the correct parameters rather than an analysis of the sensitivity of those parameters to variation.

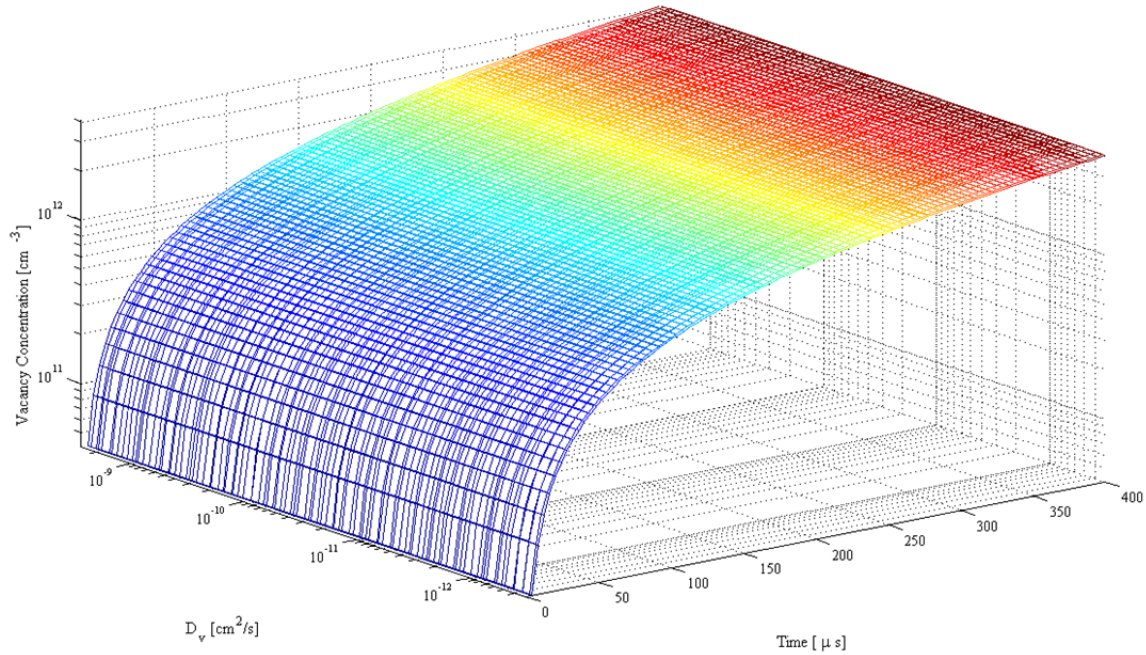


Figure 69. The vacancy concentration over a $400 \mu\text{s}$ interval and for a range of vacancy diffusivity values shows little change across the entire range.

Parameters were selected for this analysis based on their sensitivity, on a lack of values from literature, or because they were added after the sensitivity analysis from Section 5.1 was completed. To this end, Table 23 displays the parameters and initial values selected. In this table, E_{fp} is the energy required to create a Frenkel pair; D_v is the diffusivity of vacancies; C_{vo} and C_{xo} are the initial concentration of vacancies and impurities, respectively; W_b and W_e are the base and emitter widths, respectively; and N_{DE} , N_{DE} , and N_{DE} are the donor concentration in the emitter, acceptor concentration in the base, and donor concentration in the emitter, respectively.

Initially, wide ranges of values were selected for the parameters, which would be refined during each iteration of the LHS. The LHS methodology for this analysis started by creating the simulation space from the 9 parameters and the number of bins for each range, n . Then, each of the n number of sets of 9 parameters was solved for the species' concentrations as a function of time. These concentrations

Table 23. First guess for upper and lower bounds for parameter search using LHS methodology.

Parameters	Limits	
	Lower	Upper
E_{fp}	1.00×10^{-5}	1.00×10^{-3}
D_v	1.00×10^{-15}	1.00×10^{-9}
C_{vo}	1.00×10^5	1.00×10^{16}
C_{xo}	1.00×10^5	1.00×10^{16}
W_b	1.00×10^{-6}	1.00×10^{-3}
W_e	1.00×10^{-6}	1.00×10^{-3}
N_{DE}	1.00×10^{17}	1.00×10^{20}
N_{AB}	1.00×10^{13}	1.00×10^{16}
N_{DB}	1.00×10^{13}	1.00×10^{16}

were converted to device gain for comparison against the experimental data. Finally, a regression analysis of the predictive results from the mathematical model and the experimental results from the first 20-minute dosimetric measurement at IU NREF (see Section 4.1) provided a measure of the *goodness* of those .

Since the range of the initial parameters were quite large, a refinement procedure was required to truncate the range over which the search proceeded for each subsequent analysis space. After the initial simulation space was completed, a histogram was generated for each parameter that collected the number of parameters within the bin that met a threshold value for the regression coefficient, R^2 . Then, from this histogram, the slope of the leftmost 4 and rightmost 4 bins was calculated and the $y = 0$ intercept was calculated for these two lines. These two x values became the new lower and upper bounds, respectively. The results of this procedure applied to the initial LHS analysis are tabulated in Table 24. In this table, the dark delineate when a bound was smaller after refinement, light cells delineate when a bound grew after refinement, and mid cells mean that there was no change. In this way, the parameter ranges grow, shrink, or stay the same through multiple refinements.

Table 24. Change to upper and lower bounds for the parameter search after first cut using LHS methodology; colors are only to guide the eye to the parameter bounds that became smaller (red), larger (green), or stayed the same (yellow).

Parameters	LB	Δ LB	UB	Δ UB
E_{fp}	1.00×10^{-6}	- 9.00×10^{-6}	1.00×10^{-4}	- 9.00×10^{-4}
D_v	1.00×10^{-16}	- 9.00×10^{-16}	1.00×10^{-11}	- 9.90×10^{-10}
C_{vo}	1.00×10^9	1.00×10^9	1.00×10^{12}	- 1.00×10^{16}
C_{xo}	1.00×10^5	0	1.00×10^{18}	9.90×10^{17}
W_b	1.00×10^{-8}	- 9.90×10^{-7}	4.80×10^{-5}	- 9.52×10^{-4}
W_e	1.00×10^{-8}	- 9.90×10^{-7}	1.00×10^{-4}	- 9.00×10^{-4}
N_{DE}	1.00×10^{19}	9.90×10^{18}	1.00×10^{21}	9.00×10^{20}
N_{AB}	1.00×10^{15}	9.90×10^{14}	1.00×10^{17}	9.00×10^{16}
N_{DB}	1.00×10^{14}	9.00×10^{13}	1.00×10^{16}	0

After the second analysis was completed, it was obvious that the initial vacancy concentration (C_{vo}), emitter width (W_e), and donor concentrations in the emitter and base (N_{DE} and N_{DB} , respectively) changed very little over the two refinement steps. Therefore, they were set to a parameter within their range and no longer were a part of the search procedure in order to reduce sampling time. The other five parameters were again shifted by the values tabulated in Table 25.

Table 25. Change to upper and lower bounds for the parameter search after first cut using LHS methodology; colors are only to guide the eye to the parameter bounds that became smaller (red), larger (green), or stayed the same (yellow).

Parameters	LB	Δ LB	UB	Δ UB
E_{fp}	1.00×10^{-7}	- 9.00×10^{-7}	1.00×10^{-5}	- 9.00×10^{-5}
D_v	1.00×10^{-17}	- 9.00×10^{-17}	1.00×10^{-12}	- 9.00×10^{-12}
C_{vo}	1.00×10^5	- 1.00×10^9	1.00×10^{10}	- 9.90×10^{11}
W_b	1.00×10^{-8}	0	1.00×10^{-6}	- 4.70×10^{-5}
N_{AB}	1.00×10^{14}	- 9.00×10^{14}	1.00×10^{16}	- 9.00×10^{16}

Again, the results of the simulation allowed for three more parameters to be set: initial impurity concentration (C_{xo}), base width (W_b), and acceptor concentration in the base (N_{AB}). Therefore, only the Frenkel pair creation energy (E_{fp}) and the

vacancy diffusivity (D_v) remained.

In Figures 70, 71, 72, (E_{fp}) and (D_v) were used and their ranges modified based on the results of the $R^2 > 0.9$ tolerance. Figure 70 plots the value of the regression coefficient for those parameter sets that met the 0.9 threshold value. Figure 71 presents the values in Figure 70 as histograms. The top two charts of Figure 71 shows that significantly more values for E_{fp} meet the cutting criterion in the low end, so the range for both parameters was modified in the second analysis step (shown in the middle two charts). This time, however, the range for D_v was shifted too far. In the final two plots of Figure 71, the two parameter ranges are more stable. While they could be refined further, it was sufficient for analysis of the data.

Finally, Figure 72 displays a three dimensional histogram of the values of E_{fp} and D_v that met the tolerance criterion. The relationship is linear, which is expected since, as E_{fp} increases, fewer Frenkel pairs would be produced. Thus, it is shown that the diffusivity of vacancies, *i.e.* their ability to move around and recombine or annihilate with other species or themselves, must decrease.

In conclusion, the parameter search resulted in the selection of values for the nine parameters selected for analysis. Only two, the vacancy diffusivity D_v and the energy required to create a Frenkel pair E_{fp} were found to be sensitive across the range. This shows that the generation and diffusion of vacancies dominates the prediction of gain in the model.

5.3 Model/Data Comparison

With reasonable values for unknown parameters, a comparison to experimental data was accomplished. Using the parameters as determined from the Latin Hypercube Sampling, $E_{fp} = 72\text{eV}$ and $D_v = 1.05 \times 10^{-10} \text{ cm}^2/\text{s}$, the comparison is plotted in Figure 73. The model underpredicts damage for the first ten minutes of the ex-

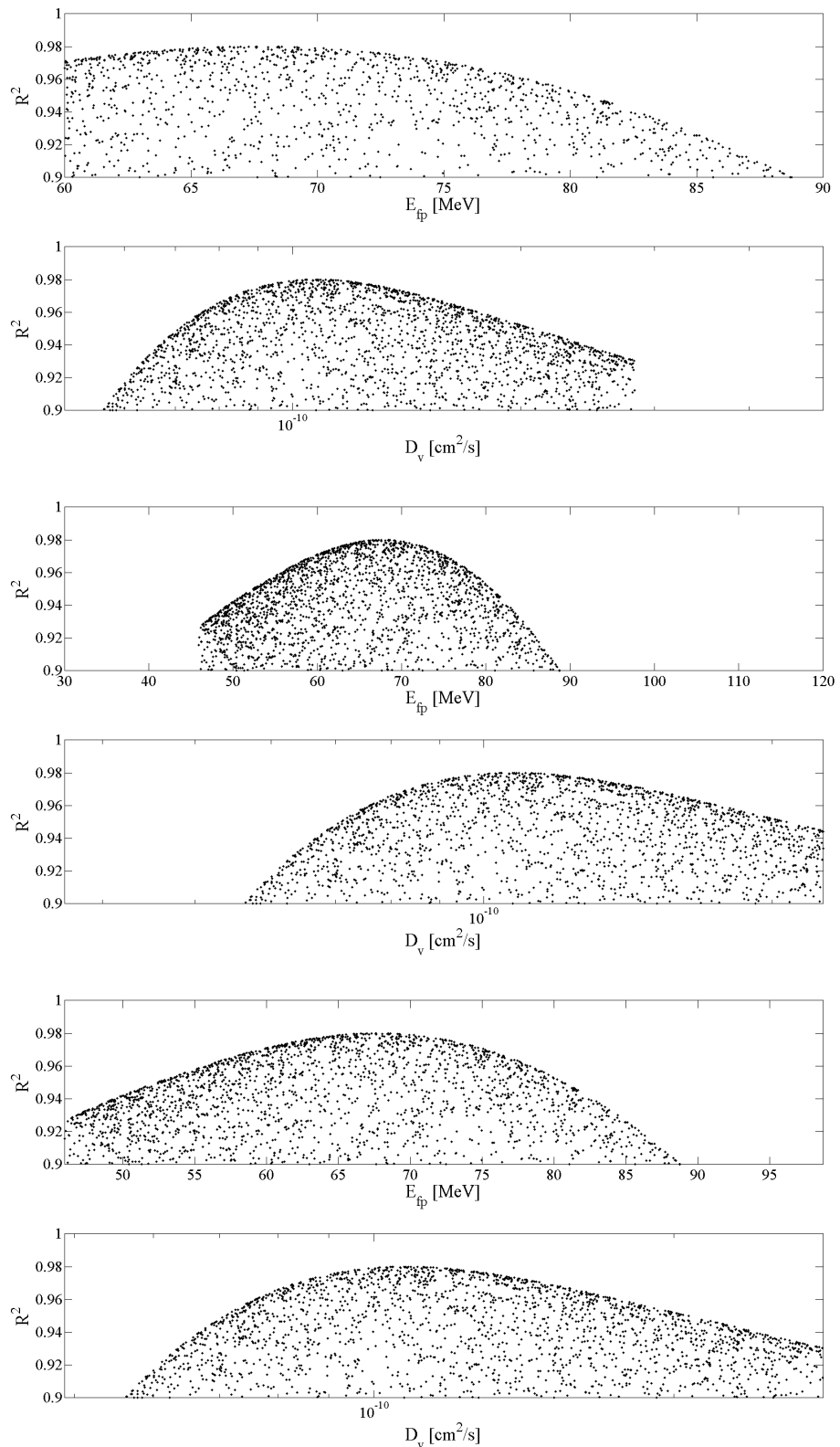


Figure 70. Regression coefficient, R^2 , as calculated for E_{fp} and D_v for the (top two) first, (middle two) second, and (bottom two) final iterations.

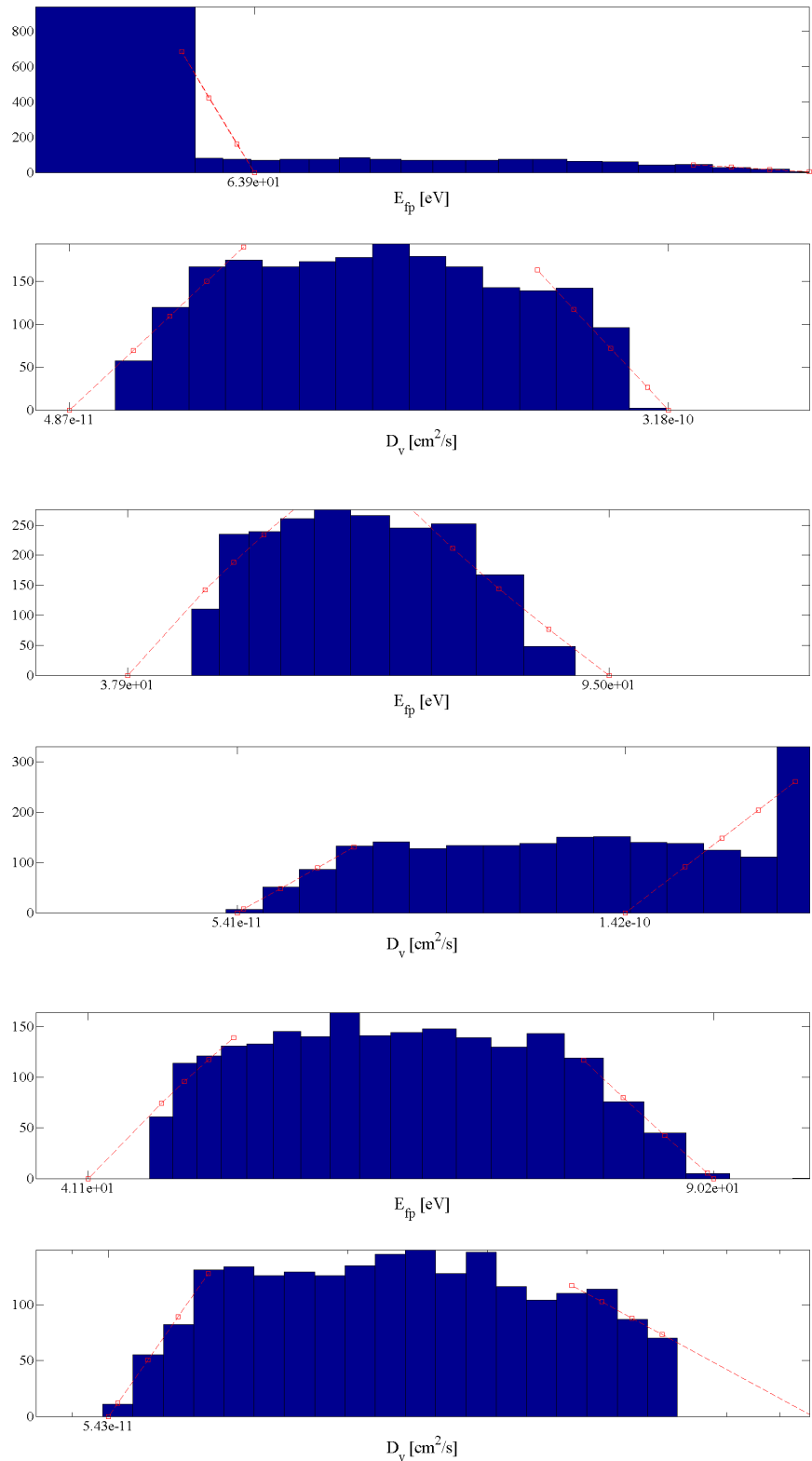


Figure 71. The regression coefficient from Figure 70 is binned in histogram form for the (top two) first try, (middle two) second try, and (bottom two) final try.

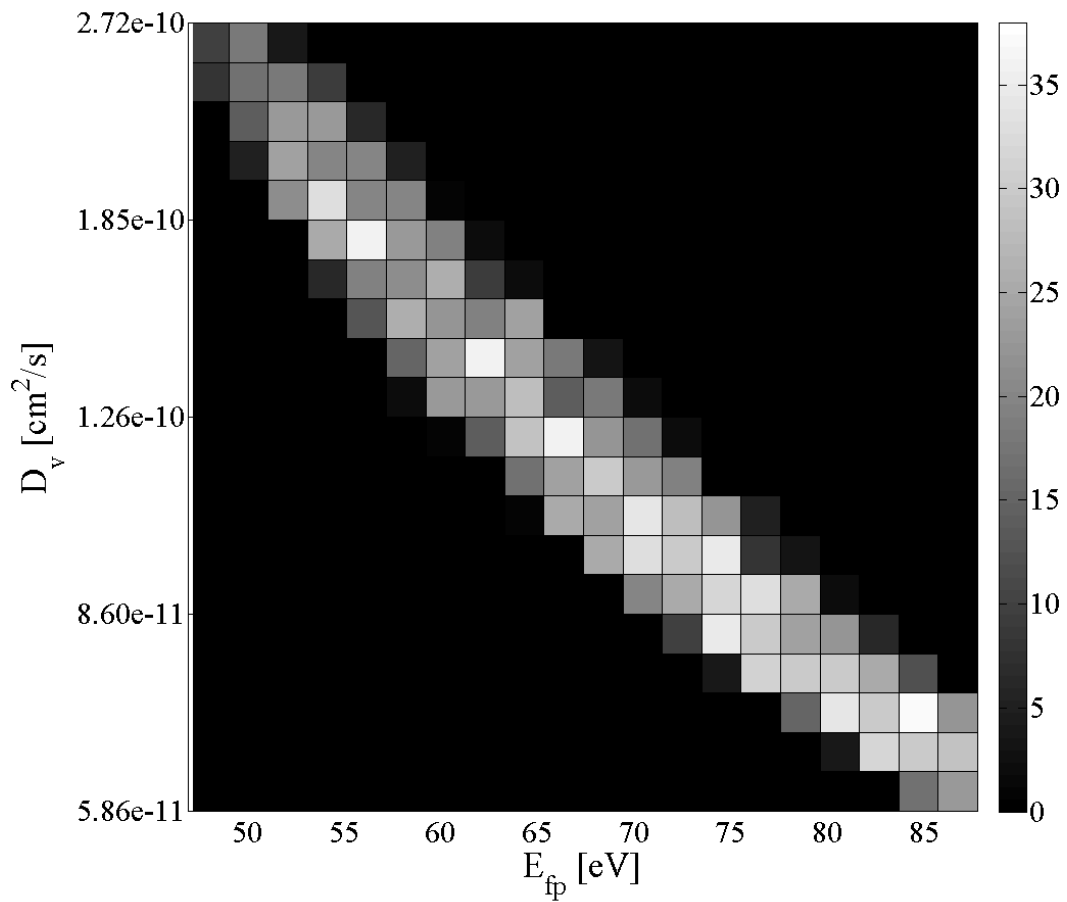


Figure 72. Three dimensional histogram of $R^2 > 0.9$ showing where both D_v and E_{fp} meet the R^2 cut.

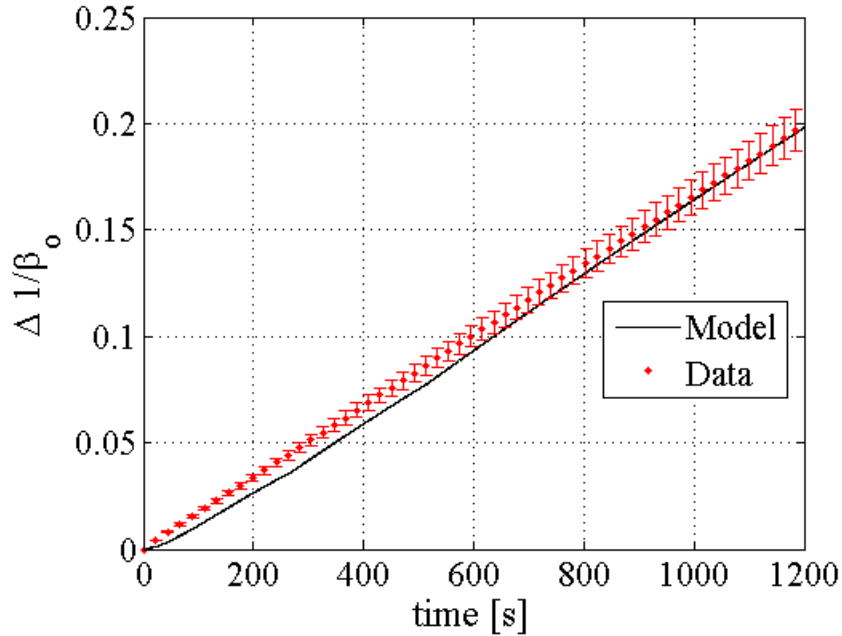


Figure 73. The change in gain as a function of time for the model as compared with experiment for IU NREF Shot 1T (beam frequency of 20 Hz, pulse width of 400 μ s, and 20 mA beam current). There is a small deficit when compared with the data until about 10 min, at which time it follows very well within experimental error.

periment. However, from this point on, the model matches the experimental data within error bounds. The slope changes for the model data between 200 and 400 seconds, which is not in the experimental data. The behavior in the model is explained as the point in which the singular impurity concentration drops below the vacancy concentration, so the gain response begins to be dominated by vacancy concentration changes. It is possible that this behavior is being dominated by another mechanism not currently implemented in the model. Further study and improvements to the model are warranted to correct these differences.

Figure 74 displays the annealing factor calculation for the model as compared with the empirical results from IU NREF Shot 1T. The annealing factor at time, t , is calculated in Equation 59.

$$AF(t) = \frac{\frac{1}{\beta(t)} - \frac{1}{\beta_o}}{\frac{1}{\beta_\infty} - \frac{1}{\beta_o}} \quad (59)$$

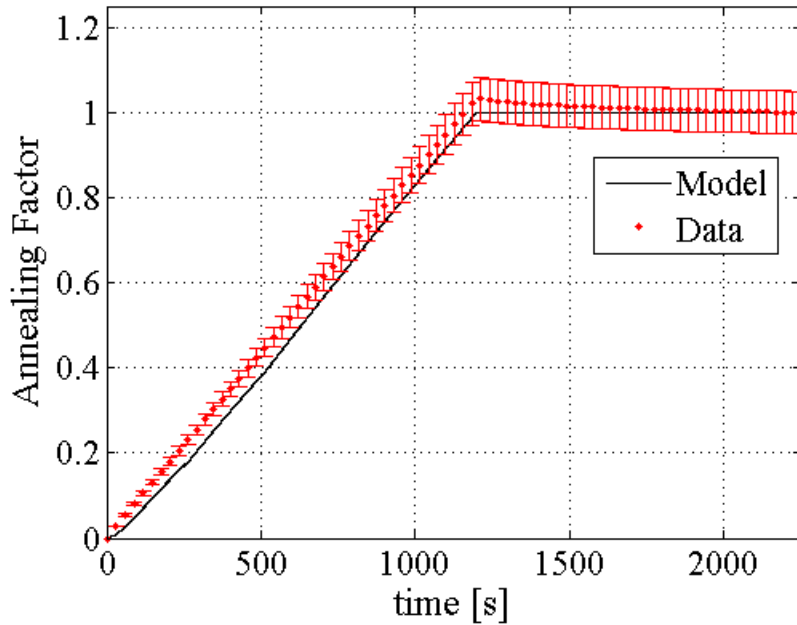


Figure 74. The annealing factor as a function of time shows good agreement for the comparison of the model against experimental data.

In Equation 59, $\beta(t)$ is the gain at time t , β_o is the gain in the device before irradiation, and β_∞ is the gain after a very long annealing time. In Figure 74, the gain at long annealing time has been taken to be the gain at the end of the annealing period. To follow the ASTM Standard more precisely, β_∞ should take the value of device gain after a period of two hours in an 80°C oven. However, since these devices have been misplaced and cannot be baked, an approximation was made.

In Figure 74, the model is being dominated by the two parameters E_{fp} and D_v . The model response, and thus the device's predicted gain, is strongly dependent on the neutron flux. However in the long term, where the flux goes to zero, the response is flux-independent. This shows that the short-lived species, such as vacancies with their relatively large diffusivity, are more sensitive during and immediately after irradiation. However, as the simulation progresses to later times, these species are almost non-existent and do not affect the device gain.

References

1. M. McKay, R. Beckman, and W. Conover, "A comparison of 3 methods for selecting values of input variables in the analysis of output from a computer code," *Technometrics*, vol. 21, no. 2, pp. 239–245, 1979.
2. R. Iman, J. Campbell, and J. Helton, "An approach to sensitivity analysis of computer models. I- Introduction, input, variable selection and preliminary variable assessment," *J. Qual. Tech.*, vol. 13, no. 3, pp. 174–183, 1981.
3. Matlab - the language of technical computing. [Online]. Available: <http://www.mathworks.com/products/matlab/>
4. ASTM Standard E722-09(e1), *Standard Practice for Characterizing Neutron Energy Fluence Spectra in Terms of an Equivalent Monoenergetic Neutron Fluence for Radiation-Hardness Testing of Electronics*, ASTM International, West Conshohocken, PA, 2009.

VI. Summary, Conclusions, and Way Forward

With the model developed, experimental measurements taken, and a comparison made between the two, conclusions can be made regarding the outcome of the research. In this section, a summary of the results of this research are presented, conclusions that can be drawn from the results of this research are presented, and the plans for future work are suggested.

6.1 Summary of Research

In the first part of this research, a mathematical model was developed that describes the interaction of defect species after they are formed in a time- and energy-dependent neutron environment. The mathematical model proceeded through a number of steps in development, starting out with Bateman-like equations of the accumulation of defect species in the same manner that radioactive atoms build up in irradiated materials. An analytical solution was sought; but as the number of defects that must be tracked expanded, the subsequent complexity of the system of differential equations made this impossible.

At this point, a change to a chemical kinetics approach modified the system of equations. Each type of interaction between species was modeled as a rate-dependent chemical interaction of two species coming together to form a third or a single species breaking into two other species. The rate of each interaction, designated α , was defined using parameters such as the diffusivity of the species interacting, the radius of capture of one species by another, and a rate of dissociation of the species. The system of equations was expanded to include 9 different defect species and the two semiconductor charge carriers, electrons and holes. The nine species modeled were vacancies, divacancies, interstitials, vacancy-impurity complexes, divacancy-impurity

complexes, impurities, 2-vacancy clusters, 3-vacancy clusters, and annihilations. The result of the development was a system of equations displayed in Equation Set 46. In each equation, C designated the concentration of a particular species (v for vacancy, x for impurity, etc.).

In Equation Set 46 was developed the idea of the *generation rate* of vacancies/interstitials, G_v and G_i respectively. These generation rates took into account the displacement damage kerma when calculating the amount of energy deposited into the material. Additionally, the gamma generation rate, G_γ , was set as the number of electron/hole pairs created in the material by the gamma dose.

The solution of this system of coupled, non-linear ordinary differential equations is a system of defect species concentrations as a function of time, and thus fluence of neutrons. An example of the resultant solution is plotted in Figure 25.

This system of defect species concentrations was then used to calculate the BJT current gain in the device. The vacancy, 2-vacancy clusters, and 3-vacancy cluster concentrations contributed to the acceptor concentration in a region, since the vacancy lies very close to the valance band within the silicon bandgap structure. The divacancies acted as thermal electron/hole pair generators, as they sit around the mid-point in the silicon bandgap. The Messenger-Spratt behavior was investigated by plotting the change in inverse current gain as a function of neutron fluence. An example is displayed in Figure 26 showing that, for a 10 second irradiation at a 1-MeV Equivalent (Si) neutron flux of $\phi_{1-MeV} = 5 \times 10^{10}$ n/cm²/s, the hypothetical silicon device responds in a linear (thus Messenger-Spratt like) manner.

Following the development of the model, a series of two experiment sets were accomplished at the IU NREF neutron source and the OSURR, which is a thermal neutron reactor-based system.

At IU, two types of experiments were conducted. A Multiple Sequential Interval

(MSI) test looked at the response of the Si BJT to multiple intervals of irradiation and annealing, all in a row. Each interval of irradiation could be mapped to Messenger-Spratt behavior.

In addition, the annealing intervals were fit to a power law function. With no more than 30 s of annealing information for this particular experiment, the power law fit the data extremely well. However, it was noted that a power function is not the best representation as the device gain would go to infinity at infinite time, whereas the actual behavior of BJTs after irradiation is to asymptotically approach a value, less than β_0 , at long time after irradiation. Therefore, it was verified that device response has more than one annealing mode.

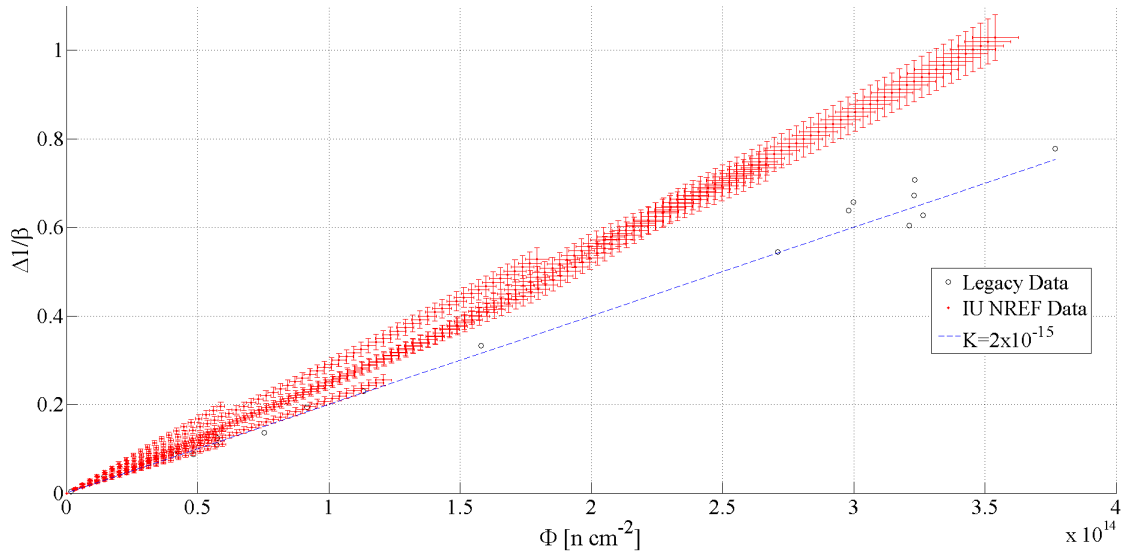


Figure 75. The $\Delta(1/\beta)$ versus fluence for the experimental data collected from the second experimental series at IU NREF as compared to data from various single-pulse, short-duration irradiation facilities such as SPR-III and WSMR FBR.

For the Single Long Interval (SLI) test, the BJT was irradiated in the IU NREF for one interval corresponding to a particular 1-MeV Equivalent (Si) interval, and current gain was measured *in-situ* during and after the irradiation. Dosimetry, via neutron activation analysis, verified the neutron flux to be approximately $5 \times 10^{10} \text{ n/cm}^2/\text{s}$ because of the mechanical jack that positioned the DuT closer to the beryllium target.

Figure 75 showed that the change in inverse current gain ($\Delta 1/\beta$) is linear with fluence for many different intervals of irradiation. Not only that, but the damage constant during irradiation was greater than that found in literature for the same devices. However, it was noted that the literature values were determined after the damaged devices had been baked for two hours in an oven at 80°C.

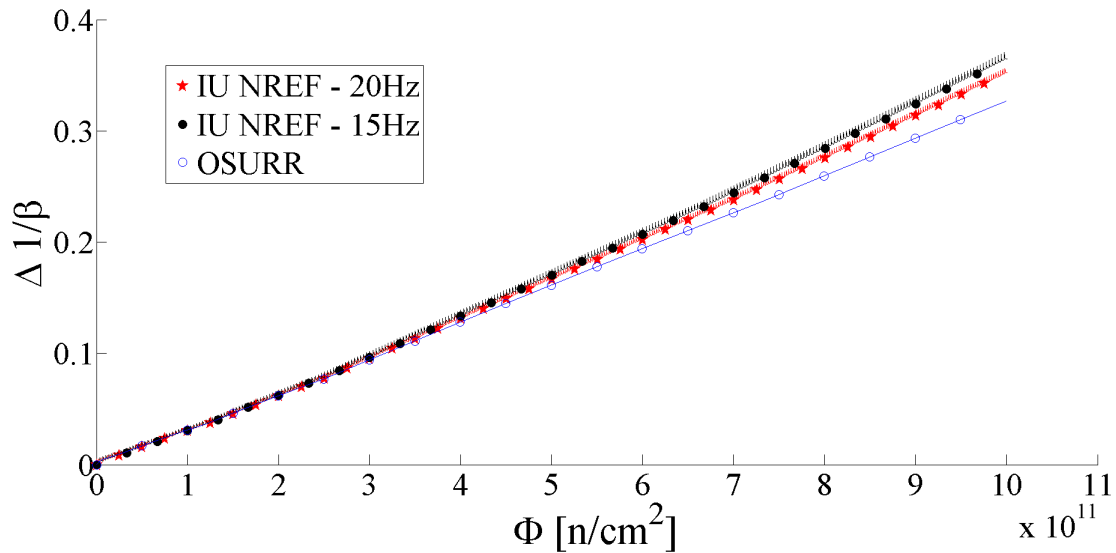


Figure 76. Simulation of three different irradiation conditions at the IU NREF and OSURR.

Next, a comparison was made between the sequentially pulsed source at IU NREF with a steady-state source at the OSURR, undertaken because the model predicted a different gain degradation response. Figure 76 displays this difference. The OSURR provided a steady-state flux of neutrons, in contrast to the multiple pulses at the IU NREF, to reach the desired total neutron fluence. In addition, the neutron energy spectrum for the OSURR is much softer than the spectrum at IU NREF. The semiconductor devices were measured at the OSURR at two power levels, 1% and 23.4% of maximum reactor power, which corresponded to a neutron flux of 2×10^9 and 4.94×10^{10} n/cm²/s in the experimental column. The SLI test was repeated at the OSURR; the BJTs being measured were irradiated for approximately 20 min and the

gain measured *in-situ*, the same as at IU NREF. The result of this analysis showed that $\Delta I/\beta$ remained linear, but with a different damage constant than the one determined during the IU NREF experiment set. At the OSURR, the damage constant measured during irradiation was between 1.60 and $2.36 \times 10^{-15} \text{ cm}^2/\text{n}$, which is much closer to that published in the ASTM standard value of $2 \times 10^{-15} \text{ cm}^2/\text{n}$ than that measured at the IU NREF, which was $> 3 \times 10^{-15} \text{ cm}^2/\text{n}$.

One final comparison was made against legacy systems, and it is plotted again in Figure 77, this time with a logarithmic scale on the x and y axes. This allows one to observe the variations in BJT current gain response at lower fluences that may not be immediately evident when plotting on a linear-linear scale. The curvature in the OSURR data may be a result of changes in neutron flux due to a rise in temperature in the core, causing the flux to be elevated. Once it was noticed by the reactor operator and adjusted, the flux was depressed to compensate.

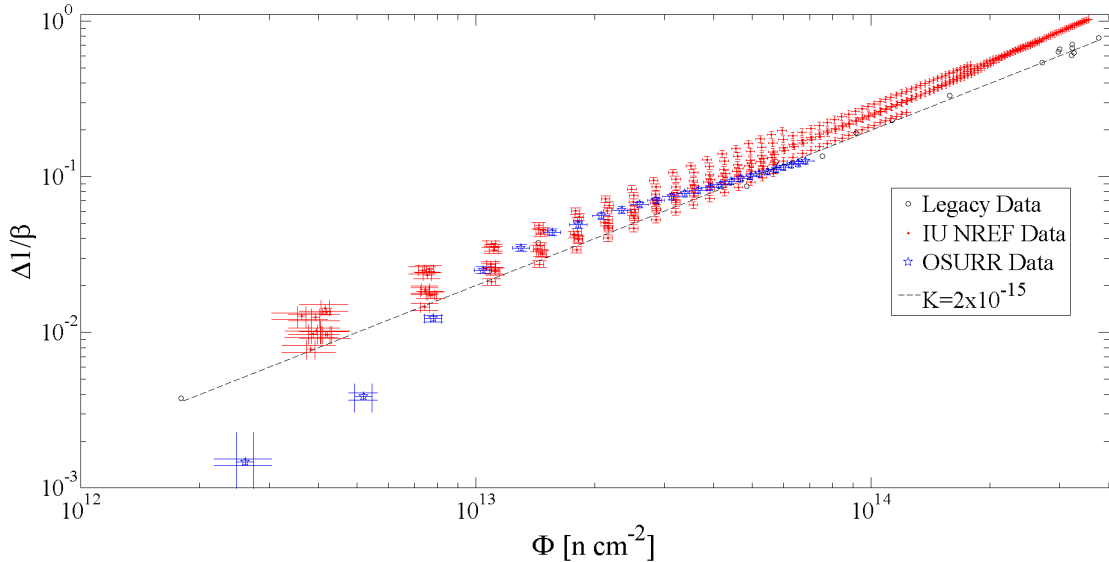


Figure 77. When comparing all datasets together, the devices respond differently for different neutron spectra; however, it is yet to be confirmed whether the ASTM elevated temperature annealing interval will have a significant enough impact to bring all devices back to the literature value for the damage constant.

To complete this research work, a comparison was made between the empirical re-

sults and predictions from the mathematical model. However, the model parameters were found to vary widely throughout literature, so a sensitivity analysis and parameter search were undertaken to determine parameters that best fit the experimental results. A Latin Hypercube Sampling technique was developed to more efficiently search through the entire range of parameters' values. The sensitivity analysis, accomplished when the model only contained six defect species, found that the vacancy generation rate parameter had the greatest affect on results in that current implementation.

However, the model was modified and additional species were added. Therefore, a new comparison was accomplished using an eleven-species model. The parameters with greatest sensitivity were the Frenkel-pair generation energy (E_{fp}), vacancy diffusivity (D_v), vacancy and impurity initial concentrations (C_{vo} and C_{xo} , respectively), base and emitter widths (W_b and W_e , respectively), and dopant concentrations in the base and emitter (N_{DE} , N_{AB} , and N_{DB}).

A series of range reductions were made based on the sensitivity, and it was found that E_{fp} and D_v were the most sensitive of these parameters. After setting all of these parameters to their most likely value based on this sensitivity analysis and parameter search, the model was used to predict the response of a hypothetical BJT subjected to a 20 min irradiation at the IU NREF. The neutron source was configured to mimic typical operating parameters at IU NREF, such that the beam frequency was 20 Hz, the neutron pulse width was 400 μ s, and the proton beam current was 20 mA. The model was shown to underpredict damage in the first 20 min, but the response matches well for the rest of the 20 min irradiation interval. However, the annealing behavior did not match as well. While it stayed within experimental error, the model responded by almost instantly relaxing to its final value of gain. On the other hand, experimental evidence indicated annealing with longer time constants. It

was surmised that this is due to the need for a more complex model to account for the long-time annealing mechanisms.

6.2 Conclusions

The kinetics-based model, in its current implementation, is able to predict device gain degradation with reasonable accuracy. However, the annealing behavior of the device does not match experimental results as well. It is suspected that this is due to the device behavior being dominated during irradiation by generation, which is directly driven by the parameter E_{fp} . The kinetic interaction of species has little effect during irradiation, and this is observed in the empirical results, as the temporal profile has little effect on the linearity of device response. However, during annealing, defect generation ceases and only species' interactions drive the behavior. Therefore, there must be some aspect of these interactions that is missing in the model. This may be a missing defect species or the interpretation of how these species are used in calculating gain may be incorrect.

This work is the first measurement into the advantages and disadvantages of using an extended irradiation period to simulate total displacement damage in silicon semiconductor devices. It was revealed that the devices continue to follow the Messenger-Spratt linear behavior in the change in inverse gain as a function of fluence for both a sequentially pulsed source such as IU NREF, as well as a steady-state source such as OSURR. Non-linearity was observed in device response for the 26% power irradiation at the OSURR, however deviations in the reactor flux leave some of the results in question. Therefore, the hypothesis that the temporal profile of the neutron source will cause a deviation from linear behavior has proven false.

It continues to be extremely important to fully understand the time-averaged neutron energy spectrum for the facility using computational particle physics techniques

combined with experimental verification, especially if the device is being measured *in-situ*. This is due to the effect that the neutron spectrum has on the types and quantities of defect species as they are created and interact in the semiconductor material during irradiation. This research has shown that, during irradiation, the harder spectrum at IU NREF causes damage at a faster rate than the softer spectrum at the OSURR at the same fluences. Unfortunately, the devices irradiated at IU NREF were misplaced and cannot be baked. However, the difference in damage constant is small enough that an 80°C bake would most likely anneal enough damage to bring the damage constant back to the expected value from literature, which was the case with the devices at the OSURR. For this reason, the hypothesis that neutron energy spectrum has a profound effect on the damage constant is not supported in this work. It is true in the sense that the spectrum has an effect *in-situ*; however, the ASTM standard bake requirement accounts for this. Therefore, the hypothesis is false in regards to long-term effects in the devices.

This research has provided better insight into why and how facilities such as IU NREF and OSURR can be used for displacement damage studies of semiconductor devices.

6.3 Ideas for Future Research

The first goal for any future research would be to refine the model. As noted in Section 6.2, the annealing behavior of devices does not match well with empirical results. The procedure for generation of defect species could be modified to better reflect the current understanding of defect species formation. To do this, the list of defect species that are tracked currently would need to be modified. In the current implementation, 2- and 3- vacancy clusters are possible, but only by the interaction of vacancies. These 2- and 3-vacancy clusters could be removed from the system of

equations and could be replaced by a species called a *cluster*. Now, the generation of Frenkel-pairs, which is driven by low energy neutrons, could be supplemented by the generation of clusters, which is driven by higher energy neutrons. This would involve a much more complicated routine for determination of the generation rates than is currently implemented in the model. However, this would more accurately describe how defect species are created in devices under neutron irradiation. Figure 78 is an example of how the spectrum at IU NREF might be broken up into three regions: one that creates Frenkel-pairs, one that creates clusters, and one that has the probability to create either.

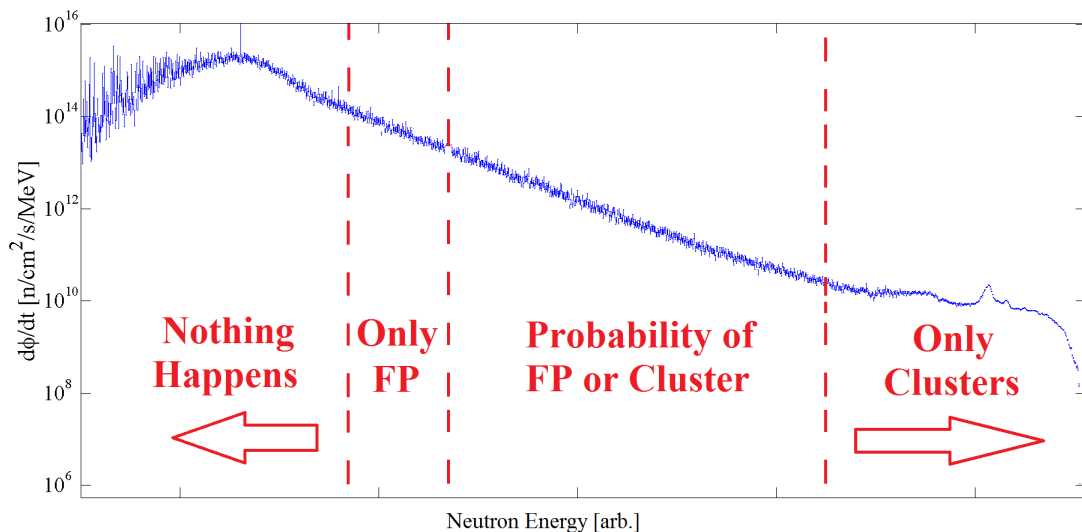


Figure 78. The differential neutron energy spectrum at IU NREF with an example of the way the spectrum may be broken up into the region that creates Frenkel-pairs (left), the region that creates clusters (right), and the region that has some probability of creating either (middle).

Another idea for future research is to expand the SLI fluence dataset. Many of the datasets contain points that consist of one measurement at a particular fluence, mainly because of time and financial restrictions. Getting better statistics by measuring multiple devices at that fluence will lead to decreasing error and refining the understanding of the device response. Additionally, the maximum fluence reached

during this research was $< 4 \times 10^{14}$ n/cm². It would be useful to irradiate a device to higher fluences to see if there is a catastrophic threshold, *i.e.* a fluence where the defects become so tightly packed that the neutrons begin to have less effect on device gain. The mathematical model in its current iteration predicts this will occur but not until much higher fluences are achieved.

Finally, once silicon devices have been investigated fully, it would be important to apply these concepts to novel semiconductor materials such as III-V devices (GaAs, etc.), carbon nanotubes, and others. Obviously, it would be necessary to modify the input parameters for the model, however that may be the only required change. Unfortunately, as was noted with silicon, many of these parameters are not well-known or are still being determined via current research. Therefore, it may be necessary to do calculations or experiments to better quantify the unknown parameters or determine them through a LHS technique.

REPORT DOCUMENTATION PAGE

Form Approved
OMB No. 0704-0188

The public reporting burden for this collection of information is estimated to average 1 hour per response, including the time for reviewing instructions, searching existing data sources, gathering and maintaining the data needed, and completing and reviewing the collection of information. Send comments regarding this burden estimate or any other aspect of this collection of information, including suggestions for reducing the burden, to Department of Defense, Washington Headquarters Services, Directorate for Information Operations and Reports (0704-0188), 1215 Jefferson Davis Highway, Suite 1204, Arlington, VA 22202-4302. Respondents should be aware that notwithstanding any other provision of law, no person shall be subject to any penalty for failing to comply with a collection of information if it does not display a currently valid OMB control number.

PLEASE DO NOT RETURN YOUR FORM TO THE ABOVE ADDRESS.

1. REPORT DATE (DD-MM-YYYY) 18-09-2014	2. REPORT TYPE Ph.D. Dissertation	3. DATES COVERED (From - To) March 2011 - September 2014		
4. TITLE AND SUBTITLE Investigating Time and Spectral Dependence in Neutron Radiation Environments for Semiconductor Damage Studies		5a. CONTRACT NUMBER		
		5b. GRANT NUMBER		
		5c. PROGRAM ELEMENT NUMBER		
6. AUTHOR(S) Halstead, Matthew R, Mr.		5d. PROJECT NUMBER		
		5e. TASK NUMBER		
		5f. WORK UNIT NUMBER		
7. PERFORMING ORGANIZATION NAME(S) AND ADDRESS(ES) Air Force Institute of Technology Graduate School of Engineering and Management (AFIT/EN) 2950 Hobson Way Wright-Patterson AFB OH 45433-7765		8. PERFORMING ORGANIZATION REPORT NUMBER AFIT-ENP-DS-14-S-04		
9. SPONSORING/MONITORING AGENCY NAME(S) AND ADDRESS(ES) Naval Surface Warfare Center, Crane Mr. Steven Clark, Chief Engineer, Radiation Sciences BLDG 3334 GXM, 300 Highway 361 Crane, IN 47522 Steven.Clark@navy.mil		10. SPONSOR/MONITOR'S ACRONYM(S) NSWC		
		11. SPONSOR/MONITOR'S REPORT NUMBER(S)		
12. DISTRIBUTION/AVAILABILITY STATEMENT Distribution Statement A. Approved for Public Release; Distribution Unlimited.				
13. SUPPLEMENTARY NOTES This work is declared a work of the U.S. Government and is not subject to copyright protection in the United States.				
14. ABSTRACT In this dissertation, a system of coupled, non-linear ordinary differential equations has been developed to track defect species in silicon. This model has been used to predict current gain degradation in silicon BJTs for various neutron fluences. These predictions have been compared against empirical data collected at two neutron irradiation facilities with different time and spectral profiles. The damage constant during irradiation has been determined, and it is different for both facilities. However, the time profile is found to have no effect in the region tested in this work. Now that this analysis has been done, these types of facility can be used in the future for neutron damage studies.				
15. SUBJECT TERMS displacement damage, neutron irradiation, bipolar junction transistor, silicon, semiconductor defects				
16. SECURITY CLASSIFICATION OF: a. REPORT U b. ABSTRACT U c. THIS PAGE U		17. LIMITATION OF ABSTRACT UU	18. NUMBER OF PAGES 184	19a. NAME OF RESPONSIBLE PERSON Dr. James C. Petrosky, AFIT/ENP 19b. TELEPHONE NUMBER (Include area code) (937) 255-3636 x4562 james.petrosky@afit.edu